J-PARC Experimental Proposal

Measurement of $\Gamma(K^+ \to e^+\nu)/\Gamma(K^+ \to \mu^+\nu)$ and Search for heavy sterile neutrinos using the TREK detector system

J-PARC TREK Collaboration *

C. Rangacharyulu and R. Pywell

Department of Physics, University of Saskatchewan, Saskatoon, Canada

M. Hasinoff

Department of Physics and Astronomy, University of British Columbia, Vancouver, BC, Canada

P. Depommier

Laboratoire de Physique Nucléaire, Universite de Montréal, Canada

J. Doornbos, D. Gill, and R. Henderson

TRIUMF, Vancouver, Canada

M. Gericke

Department of Physics, University of Manitoba, Winnipeg, Canada

A. Accardi, J. Diefenbach, C. Keppel, M. Kohl, P. Monaghan, L. Tang, L. Yuan, and L. Zhu

Department of Physics, Hampton University, Hampton, VA, USA

C. Djalali and S. Strauch

Department of Physics and Astronomy, University of South Carolina, Columbia, SC, USA

E.W. Anderson

College of Liberal Arts & Sciences, Iowa State University, Ames, Iowa, USA

D. Hasell, R. Milner, and B. Surrow
MIT Laboratory for Nuclear Science and Bates Linear Accelerator Center,
MIT, Cambridge, Massachusetts, USA

A. Ivashkin, A. Kurepin, and V. Marin
Institute for Nuclear Research of RAS, Moscow, Russia

D.P. Nguyen and C.V. Tao
National Science University, HCNC, Vietnam

K. Horie and S. Shimizu[†]
Department of Physics, Osaka University, Osaka, Japan

H. Yamazaki
Department of Physics, Tohoku University, Sendai, Japan

M. Uchida
Department of Physics, Tokyo Institute of Technology, Tokyo, Japan

K. Ozawa
Department of Physics, Faculty of Science, University of Tokyo, Tokyo, Japan

Y. Igarashi, J. Imazato, and A. Toyoda
High Energy Accelerator Research Organization (KEK), Tsukuba, Japan

June 12, 2010

[*]The listed collaboration members are only staffs. Students are not included in the list.
[†]Contact person, E-mail: suguru@phys.sci.osaka-u.ac.jp

Abstract

We propose a precise measurement ratio of the decay width $R_K = \Gamma(K^+ \to e^+\nu)/\Gamma(K^+ \to \mu^+\nu)$ to test lepton universality using a sub-system of the TREK experiment during low-intensity period. The Standard Model (SM) prediction for the R_K value is highly precise ($\Delta R_K/R_K = 0.5\times10^{-3}$) and a deviation from this value would very clearly indicate the existence of New Physics beyond the SM. Recently, a minimal supersymmetric (SUSY) extension of the SM (MSSM) has been considered as a candidate for the new physics to be tested by R_K. A possible mechanism to detect the SUSY Lepton Flavor Violation effect through a deviation from the lepton universality has been discussed. The non-vanishing e-τ lepton mixing can change the R_K value from the SM prediction at the percent level. In this proposed experiment, we aim at achieving an uncertainty for R_K of better than $\Delta R_K/R_K = 2 \times 10^{-3}$, which is about half of the current world record.

We also propose a new experiment to search for heavy sterile neutrinos (N) in the $K^+ \to \mu^+N$ decay using a stopped K^+ beam by adding the μ^+ polarimeter to the above experimental setup. The neutrino minimal Standard Model predicts this branching ratio to be up to 10^{-6} which is accessible by using the TREK experimental apparatus. This decay has some important features such as (1) a narrow peak structure would be formed in the momentum spectrum; (2) the μ^+ polarization would be 100% and opposite from the normal decay $K^+ \to \mu^+\nu$. By measuring both the μ^+ momentum and the μ^+ polarization, we will improve the sensitivity of the branching ratio to better than 10^{-8}, which is about 100 times more sensitive than the previous experiment.

Since these two experiments will be performed simultaneously using a common experimental setup, we regard both proposed measurements as a unified one experiment. The intensity of the primary proton beam is not very important to carry out the experiment and it is possible to collect sufficient events with low-intensity beam such as during the 30 kW operation with a total runtime of 2700 kW·day. The detector components have to be upgraded or newly made item-by-item to realize the TREK experiment (E06), and the proposed experiments can be done on our way to the final TREK configuration.

Contents

1 Physics Motivation of the $\Gamma(K^+ \to e^+\nu)/\Gamma(K^+ \to \mu^+\nu)$ measurement **10**

1.1 $K^+ \to l^+\nu_l$ decay and lepton universality 10
1.2 Contribution from MSSM 11
1.3 Contribution from other models 12

2 Experimental status of the lepton universality test **14**

2.1 $R_K = \Gamma(K^+ \to e^+\nu)/\Gamma(K^+ \to \mu^+\nu)$ measurements 14
2.1.1 NA48/2 and NA62 at CERN 14
2.1.2 KLOE at DAϕNE 16
2.2 $R_\pi = \Gamma(\pi^+ \to e^+\nu)/\Gamma(\pi^+ \to \mu^+\nu)$ measurements 16
2.2.1 PEN at PSI 17
2.2.2 PIENU at TRIUMF 18
2.3 Measurement of $\Gamma(K^+ \to \pi^0\mu^+\nu)/\Gamma(K^+ \to \pi^0 e^+\nu)$ ratio by the E246 collaboration 18
2.4 Summary of the experimental situation 19

3 Proposed experiment for the R_K measurement at J-PARC **21**

3.1 R_K measurement using stopped kaons at J-PARC 21
3.2 Overview of the proposed experiment 22
3.3 Details of the experiment 24
3.3.1 K1.1BR beam line 24
3.3.2 Kaon trigger and stopping target 26
3.3.3 Spectrometer and tracking 27
3.3.4 Particle identification 29
3.3.5 Photon detector 31
3.3.6 Gap photon counter 32
3.3.7 Electronics and data acquisition 33
3.3.8 R_K measurement at J-PARC 34

4 Analysis **36**

4.1 K^+ analysis 37
4.2 e^+ and μ^+ momentum analysis 38
4.3 γ analysis 38
4.4 Particle identification 39
4.5 K_{e2} and $K_{\mu 2}$ data sample 39

5 Monte Carlo simulation **41**

5.1 Theoretical form of the $K^+ \to l^+\nu\gamma$ decay 43
5.2 K_{l2} and $K_{l2\gamma}$ spectra in the D0 sample 44
5.3 K_{l2} and $K_{l2\gamma}$ spectra in D1 sample 46

6 Determination of the $\Gamma(K^+ \to e^+\nu)/\Gamma(K^+ \to \mu^+\nu)$ ratio **51**
6.1 Backgrounds from SD component of $K_{e2\gamma}$ decay 51
6.2 Determination of the R_K value using the D0 sample 52
6.3 Internal consistency check for radiative correction 54
6.4 Measurement of external bremsstrahlung photons 55
6.5 Byproduct physics 55
6.5.1 The $K^+ \to e^+\nu\gamma$ decay 55
6.5.2 The $K^+ \to \mu^+\nu\gamma$ decay 56

7 Estimation of experimental sensitivity for the R_K determination **56**
7.1 Statistical error 56
7.2 Systematic error 57
7.2.1 Reduction mechanism of systematic error 57
7.2.2 Background contamination 58
7.2.3 Inefficiency of tracking elements 58
7.2.4 Performance check of particle identification 59
7.2.5 Radiative correction 60
7.2.6 K_{e2} acceptance loss due to high energy bremsstrahlung emission 60
7.2.7 Summary of systematic errors 60
7.3 Constraint to SUSY model 61

8 Physics motivation of heavy neutrino search **64**
8.1 Description of νMSM 64
8.2 Constraint on the model parameters 65
8.3 Contribution to kaon decays 65

9 Experimental situation of heavy neutrino search **66**
9.1 KEK-PS E99 experiment 66
9.2 CERN PS191 experiment 67

10 Proposed experiment for heavy neutrino search at J-PARC **69**
10.1 Overview of the experiment 69
10.2 Muon polarimeter 71
10.3 π^0 veto system 71
10.4 μ^+ momentum resolution 74
10.5 Experiment at J-PARC 76
10.6 Byproduct physics 76
10.6.1 Search for heavy neutrino in $K^+ \to e^+N$ 76
10.6.2 The $K^+ \to \mu^+\nu\gamma$ decay 77
10.6.3 The $K^+ \to \pi^0\mu^+\nu$ decay 77

11 Experimental sensitivity of heavy neutrino search **77**

12 Beam time request **81**

13 Schedule **82**
13.1 Transfer of the SC toroidal spectrometer 82
13.2 Beam commissioning of K1.1BR 82
13.3 Detector preparation 82
13.4 Further effort toward TREK 83

14 Cost estimation and funding **84**

A Appendix: Measurement of bremsstrahlung photons in the E470 experiment **90**
A.1 KEK E470 experiment 90
A.2 K_{e3} selection 90
A.3 Conclusion 90

B Appendix: Theoretical form of muon polarization from the $K^+ \to \mu^+\nu\gamma$ decay **94**

Introduction

The electroweak Standard Model (SM) based on the Cabbibo-Kobayashi-Maskawa mixing matrix (CKM matrix) successfully explains the various results of particle and nuclear physics experiments and has been considered to describe the nature of the particles and their interactions precisely [1, 2]. The SM consists of quarks and leptons with three generations for the origin of matter, gauge bosons for the interaction between matter, and Higgs particles for the vacuum description. So far, all the SM-predicted particles already have been observed except for the Higgs particle, but it is expected to be probably discovered in the mass region of $110 < M_H < 200$ GeV by the LHC experiment at CERN. Also, CP violation, discovered in the neutral kaon system in 1964 [3], has been observed in the asymmetric decay timing of the B^0,$\bar{B^0} \to J/\Psi\ K_S^0$ decays [4, 5]. The experimental results are consistent with the SM predictions which are induced by quark mixing in the CKM matrix. Therefore, the SM has been increasingly well established over the past forty years, and its present-day position has become quite firm.

However, it is said the SM is just an effective low-energy description and that new physics lies at the energy scale of the $\sim$ TeV region, because we know the following problems:

- (1) The energy scale of the electroweak interaction is 10^{12-13} times different from that of the Grand Unified Theory (GUT) physics scale (hierarchy problem).
- (2) The dark matter and dark energy making up 20% and 70% of the Universe, respectively, cannot be explained.
- (3) The baryon asymmetry in the Universe (Baryogenesis) can not be derived from the SM.
- (4) Why do the neutrinos have non-zero masses?
- (5) There are about 20 unknown parameters which cannot be determined in the framework of the SM.

These problems cannot be explained by the SM at all. This is the reason that we consider the inevitable existence of new physics beyond the SM. In order to explain the above problems, two theoretical approaches (a) supersymmetry (SUSY) for (1)(2) and (b) the existence of right-handed singlet neutrinos for (2)(3)(4) have been paid attention to.

The Minimal Supersymmetric Standard Model (MSSM) is the minimal extension to the SM that realizes supersymmetry [6]. Supersymmetry pairs bosons with fermions; therefore every SM particle has a partner that has yet to be discovered. The MSSM was originally proposed to stabilize the weak scale, solving the hierarchy problem by the cancellation mechanism of virtual boson and fermion loops. There are five classes of particles that superpartners of the SM fall into: squarks, gluinos, charginos, neutralinos, and sleptons. These superparticles have their interactions and

subsequent decay described by the MSSM and each has a characteristic signature. It turns out that a minimum of two complex Higgs doublets are required, yielding eight components in all and five physical Higgs particles. The mass and coupling of the SUSY particles are described in terms of four parameters: three masses and one mixing angle tanβ.

The discovery of non-zero neutrino masses suggests the likely existence of gauge singlet fermions that participate in the neutrino mass generation via the seesaw mechanism [7]. To accommodate these neutrino masses, one can add several electroweak singlets to the SM Lagrangian, involving active neutrinos with lighter mass states and sterile neutrinos with heavier mass states. One can consider three electroweak singlets and thus three sterile neutrinos, all of which have masses below the electroweak scale: one has a mass of order of a few keV, while the two remaining sterile neutrinos masses are at about 0.1−10 GeV (νMSM). This νMSM is singled out for the minimal particle content consistent with baryogenesis via leptogenesis and having a dark-matter candidate.

Effects from new physics beyond the SM have been investigated experimentally by LHC [8], Belle [4], BaBar [5], T2K [9], etc. around the world. We are strongly expecting to get keys to answer the above unsolved questions existing in particle physics. In these experiments, researchers try to find phenomena induced from new physics and may achieve some unexpected results. In the kaon community, rare kaon decays such as $K_L \to \pi^0\nu\bar{\nu}$ and $K^+ \to \pi^+\nu\bar{\nu}$ have been studied to look for new physics [10]. Also, we have been searching for a new CP phase by measuring the transverse muon polarization (P_T) in $K^+ \to \pi^0\mu^+\nu$ (KEK-E246 experiment) using a stopped K^+ method. P_T is described as a T-odd correlation which is a clear signature of T-violation. Since the contribution from the SM is nearly zero, a non-zero value of P_T directly indicates the existence of new physics (of exotic scalar interaction in this case, such as charged Higgs exchange). The final result of the E246 experiment was consistent with no T-violation, and the world's best limit was obtained to be $P_T = -0.0017 \pm 0.0023(stat.) \pm 0.0011(syst.)$. Now we are preparing further P_T search with a sensitivity of $\Delta P_T \sim 10^{-4}$ (the TREK experiment) at J-PARC, where a higher accelerator beam intensity will be available in the near future [11].

However, it has become clear that the low-intensity of the hadron beam at the early stage of J-PARC is a major limiting factor to begin the TREK experiment. It will still be a few years before we will reach the intensity required for the TREK experiment. We have re-examined the experimental and physics plan by considering any possible K^+ decay channels toward the realization of the experiment, while J-PARC is ramping up the beam intensity. At this time, we would like to propose two new experiments using a partial configuration of the TREK experimental apparatus during the low-intensity period before starting the TREK data collection:

- Measurement of the $R_K = \Gamma(K^+ \to e^+\nu)/\Gamma(K^+ \to \mu^+\nu)$ ratio, and
- Search for heavy sterile neutrinos (N) in the $K^+ \to \mu^+ N$ decay.

The intensity of the primary proton beam is not very important to carry out these

experiments and it is possible to accumulate the data with sufficient statistics using relatively low-intensity beam such as the 30 kW operation. We also do not need to fully complete the TREK experimental system for the proposed experiments. The detector components have to be upgraded item-by-item in order to realize our final goal in the TREK data collection, and these experiments can be done on our way to the final TREK configuration. If the J-PARC intensities reach their design values sooner, we will reconsider this strategy and begin the TREK experiment at the earliest possible date. Note a ten-fold increase in the beam intensity will also make these initial experiments much faster, and therefore they can still be addressed.

The SM prediction of the R_K branching ratio value is highly precise ($\Delta R_K/R_K \sim 0.4 \times 10^{-3}$) and a deviation from this value clearly indicates the existence of new physics beyond the SM [12]. Recently, a possible mechanism to detect the Lepton-Flavor-Violating effect in MSSM has been discussed for the R_K measurement [13, 14]. The non-vanishing e-τ lepton mixing can change the R_K value from the SM prediction at the percent level. Likewise, the νMSM predicts the $K^+ \to \mu^+ N$ branching ratio to be up to 10^{-6} [15, 16]. This decay has some important features such as (i) a narrow peak structure would be formed in the momentum spectrum and (ii) the μ^+ polarization is 100% and opposite from that of the normal $K^+ \to \mu^+\nu$ decay. By measuring both the μ^+ momentum and the μ^+ polarization, we will improve the sensitivity of the branching ratio to better than 10^{-8}. It should be emphasized that the great variety of our experiences cultivated in the E246 experiment such as the understanding of the detector properties, elaborate codes for the Monte Carlo simulation, sophisticated analysis procedures, etc. will enable us to successfully perform the proposed experiments.

In this proposal, the former and latter experiment are described in Sections $1-7$ and $8-11$, respectively. Since these two experimental data will be taken using the common experimental setup at the same time, we would like to consider that they are not independent experiments. For the R_K measurement, the magnetic field of the spectrometer $B = 1.4$ T will be optimized for the $K^+ \to e^+\nu$ and $K^+ \to \mu^+\nu$ decays, and neutrinos corresponding to high μ^+ momentum region can be simultaneously searched for. The magnetic field will be changed to $B = 0.65$ T to cover wide μ^+ momentum region for heavier neutrinos, and $K^+ \to \pi^0 e^+\nu$ and $K^+ \to \pi^0\mu^+\nu$ events will be accepted for checking the correctness of the acceptance calculations. Therefore, the two measurements have certain common features and a series of the data collection with two magnetic fields should be considered as the unified experiment.

Measurement of the $\Gamma(K^+ \to e^+\nu)/\Gamma(K^+ \to \mu^+\nu)$ ratio

1 Physics Motivation of the $\Gamma(K^+ \to e^+\nu)/\Gamma(K^+ \to \mu^+\nu)$ measurement

1.1 $K^+ \to l^+\nu_l$ decay and lepton universality

High precision electroweak tests represent a powerful tool to prove the Standard Model (SM) and to obtain indirect hints of new physics. The $K^+ \to l^+\nu_l$ decay (K_{l2}), which is the simplest semileptonic decay among the K^+ decay channels, is one of the best channels to perform such tests. Lepton universality, which is expressed as the identical coupling constant of the three lepton generations —the electron, muon, and tau— is a basic assumption in the SM. Violation of lepton universality clearly indicates the existence of other physics beyond the SM.

The matrix element of K_{l2} decays can be described to be

$$M = g_l \frac{G}{\sqrt{2}} q^\lambda f(q^2)[u_l \gamma_\lambda (1-\gamma_5) u_\nu] \quad (1)$$

$$= g_l \frac{G}{\sqrt{2}} f_K m_l u_l (1-\gamma_5) u_\nu, \quad (2)$$

where g_l is the coupling constant for the lepton current and g_e/g_μ should be unity under the assumption of lepton universality. $f(q^2)$ is the hadronic form factor as a function of momentum transfer squared (q^2) which is the only Lorentz scalar that can be formed from q. However, in the present case, $q^2 = m_K^2$ and $f(m_K^2) = f_K$ is a constant. The K_{l2} decay diagrams are shown in Fig. 1. Then, the K_{l2} decay width can be calculated as

$$\Gamma(K_{l2}) = g_l^2 \frac{G^2}{8\pi} f_K^2 m_K m_l^2 \left(1 - \frac{m_l^2}{m_K^2}\right)^2. \quad (3)$$

This K_{l2} hadronic form factor can be canceled out by forming the ratio of the electric (K_{e2}) and muonic ($K_{\mu 2}$) decay modes as,

$$R_K^{SM} = \frac{\Gamma(K^+ \to e^+\nu)}{\Gamma(K^+ \to \mu^+\nu)} = \frac{m_e^2}{m_\mu^2} \left(\frac{m_K^2 - m_e^2}{m_K^2 - m_\mu^2}\right)^2 (1+\delta_r) \quad (4)$$

$$= (2.472 \pm 0.001) \times 10^{-5}, \quad (5)$$

under the assumption of μ-e universality. Conversely, this ratio can provide a test of μ-e universality as,

$$g_\mu/g_e = (R_K^{exp}/R_K^{SM})^{1/2}. \quad (6)$$

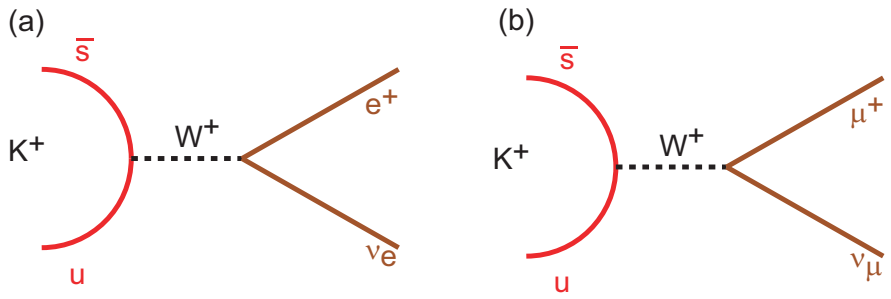

Figure 1: Feynman diagrams of (a) K_{e2} and (b) $K_{\mu 2}$. The hadronic form factor f_K is canceled out by forming the ratio of the decay widths. The SM prediction of R_K is known with excellent accuracy.

Here, the numerical value comes from inserting the particle masses into Eq. (4). δ_r is a correction due to the internal bremsstrahlung process (IB) which is, unlike the structure dependent process (SD), by definition included in R_K. The factor $(m_e/m_\mu)^2$ accounts for the helicity suppression of K_{e2} decay due to the $V-A$ structure of the charged weak current, and, in other words, enhances the sensitivity to effects beyond the SM. As a result, the SM prediction of R_K^{SM} is known with excellent accuracy ($\Delta R_K/R_K \sim 0.4 \times 10^{-3}$) and this makes it possible to search for new physics effects by a precise measurement of R_K.

1.2 Contribution from MSSM

Over the past forty years, the SM has been very successful in explaining various physics phenomena. However, it is said that the SM is only an effective low-energy description and new physics lies at the energy scale of ∼TeV. There is a good chance that the LHC will discover new elementary particles such as various supersymmetric (SUSY) particles soon.

Recently, in the kaon physics field, a minimal SUSY extension of the SM (MSSM) with R parity has also been considered as a candidate for new physics to be tested by R_K [12]. It is well known that models containing at least two Higgs doublets generally allow flavor violating couplings of the Higgs bosons with the fermions. In the MSSM, such Lepton Flavor Violation (LFV) couplings are absent at tree level. However, once non holomorphic terms are generated by loops and given a source of LFV among the sleptons, Higgs-mediated Hll LFV couplings are unavoidable. These effects have been widely discussed in the recent literature through the study of several processes, namely $\tau \to l_j l_k l_k$ [17], $\tau \to \mu\eta$ [18], μ-e conversion in nuclei [19], $B \to l_j \tau$ [20], $H \to l_j l_k$ [21], and $l_i \to l_j \gamma$ [22].

In the case of K_{l2}, in addition to the normal $W^\pm$ exchange shown in Fig. 1, a possible mechanism to detect the LFV SUSY effect through a deviation from the μ-e universality has been discussed. A charged Higgs-mediated SUSY LFV contribution,

as shown in Fig. 2, can be strongly enhanced by emitting a τ neutrino. This non-vanishing e-τ lepton mixing effect can be described as,

$$R_K^{LFV} = R_K^{SM}\left(1 + \frac{m_K^4}{M_{H^+}^4}\cdot\frac{m_\tau^2}{m_e^2}\Delta_{13}^2\tan^6\beta\right), \tag{7}$$

where M_H is the mass of the charged Higgs. Δ_{13} is the term induced by the exchange of a Bino and a slepton, which represents the contribution of LFV effect generated from the off-diagonal flavor changing entries of the slepton mass matrix. A large enhancement factor m_τ^2/m_e^2 can produce a sizable effect in R_K through change of the K_{e2} width (the contribution to $K_{\mu 2}$ is a factor of $\sim m_e^2/m_\mu^2$ smaller). Taking $\Delta_{13} = 5\times10^{-4}$, $\tan\beta = 40$, and $M_H = 500$ GeV, we can obtain $R_K^{LFV} = 1.013\times R_K^{SM}$. Thus, it is possible to reach a contribution at the percent level thanks to the possible LFV enhancements arising in SUSY models. Here it should be noted that the second term in Eq. (7) is proportional to m_K^4, indicating that the μ-e universality test in the pion channel, the measurement of $R_\pi = \Gamma(\pi^+\to e^+\nu)/\Gamma(\pi^+\to\mu^+\nu)$, is not sensitive to this model because of the suppression factor of m_π^4/m_K^4, unless the achievable experimental sensitivity of R_π is much higher than that of R_K.

Therefore, the advantage of the R_K measurement can be summarized as,

- The branching ratio of K_{e2} is very small due to the helicity suppression in the $V-A$ structure. However this makes the K_{e2} decay sensitive to the physics beyond the SM.
- By forming the ratio of the K_{e2} to $K_{\mu 2}$ width, the hadronic form factor is cancelled out and the R_K prediction in the SM becomes highly precise. Also the measurement becomes more precise by the cancellation of the form factor.
- The charged Higgs-mediated LFV effect arising in SUSY models can contribute to the K_{e2} width at the percent level. Since this effect is proportional to m_K^4, the lepton universality test in the kaon channel is much superior to that in the pion channel.
- We can observe the LFV effect as a deviation from μ-e universality by measuring the R_K value with high precision.

1.3 Contribution from other models

A precise measurement of the R_K value can set constraints in certain other non-standard model scenarios. Scalar couplings arising from physics beyond the SM will also induce pseudoscalar interactions through loop corrections [23], and in most cases the measurement provide substantially stronger limits than ones derived from super-allowed beta decay measurements and CKM unitarity. In the case of R-parity violating SUSY, the exchange of various generations of squarks may lead to a non-universal contribution that results in a comparable deviation, and the measurement

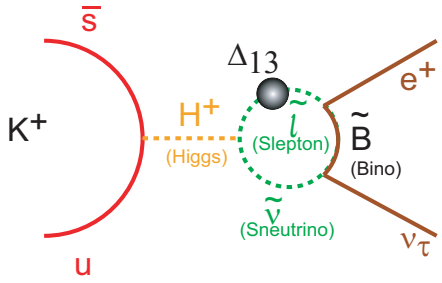

Figure 2: Contribution from charged Higgs-mediated LFV effect arising in SUSY model. Effect from non-vanishing e-τ mixing can be strongly enhanced by emitting a τ neutrino.

places substantial constraints on the possible size of R-parity violating effects [24]. In other approaches the results constrains theories involving sterile neutrinos (see for example [25]), and Majorons [26]. Several interesting new ideas (e.g. a hypothesis involving neutrino mass generated from the QCD quark condensate [27]) have been presented.

In particular, if the $K^+ \to l^+\nu$ decays are dominated by a pseudoscalar coupling, the helicity suppression of the K_{e2} would vanish (helicity unsuppressed) and the R_K value becomes of order $\sim$1. The difference between the experimental results and the SM description of the process provide an estimate of residual pseudoscalar coupling such as charged Higgs exchange, pseudoleptoquark exchange, and so on. Since the pseudoscalar contribution arises as an interference term with the dominant axial-vector term, the contribution is proportional to $1/M_P^2$, where M_P is the mass of the hypothetical particle. Ignoring the small contribution to $K_{\mu 2}$, with a presence of pseudoscalar interactions, the deviation of the new branching ratio from the SM prediction can be described as,

$$R_K^P \sim R_K^{SM}\left[1 \pm \frac{\sqrt{2}\pi}{G}\frac{1}{\Lambda_{eP}^2}\frac{m_K^2}{m_e(m_d+m_u)}\right] \tag{8}$$

$$\frac{R_K^P}{R_K^{SM}} \sim 1 + \left(\frac{1\mathrm{TeV}}{\Lambda_{eP}}\right)^2 \times 10^3, \tag{9}$$

where Λ_{eP}^2 is the mass scale of the new pseudoscalar interaction in K_{e2} decay. This makes a measurement of R_K with a 0.1% uncertainty sensitive to mass scales of $\sim$1000 TeV for pseudoscalar interaction.

2 Experimental status of the lepton universality test

2.1 $R_K = \Gamma(K^+ \to e^+\nu)/\Gamma(K^+ \to \mu^+\nu)$ measurements

The current world average of R_K is composed of three 1970s measurements. Recently, the NA48 and KLOE groups performed measurements, and in the KAON09 conference which was held in Tsukuba, Japan, they reported the latest results of the R_K values, as follows [14, 29]. The results of these measurements are shown in Table 1 and Fig. 5.

2.1.1 NA48/2 and NA62 at CERN

The NA62 experiment at CERN collected a large sample of $K^+ \to e^+\nu$ decays during a dedicated run in 2007-08, which allowed a precise test of lepton universality. Their final goal was a R_K measurement with 0.4% accuracy.

The NA48/2 beam line and the experimental setup were used. The running conditions were optimized for the K_{e2} measurement in 2007 using the experience of earlier studies based on the NA48/2 data. The beam line was capable of simultaneously delivering K^+ and K^- beams with a narrow momentum band and a central momentum of 74 GeV/c was adopted in 2007. The momentum of the incoming kaon was not measured directly in every event, but the averaged beam momentum was monitored by using $K_{\pi 3}$ decays to reconstruct K_{l2} kinematics from the missing mass (M_{miss}). The narrow momentum spectrum ($\delta p_K^{RMS}/p_K \simeq 2\%$) had the advantage to minimize the contribution to the M_{miss} resolution.

The K_{l2} decay signature consisted of a single reconstructed track. Since the incoming K^+ was not tracked, backgrounds induced by the beam halo had to be carefully considered. The performance of the muon sweeping magnet system resulted in lower background in the K_{e2}^+ sample ($\simeq 1\%$) than in the K_{e2}^- sample ($\simeq 20\%$). The halo background was directly measurable using the samples of reconstructed K_{l2} candidates. Among the subdetectors located downstream of a vacuum decay volume, a magnetic spectrometer, a plastic scintillator hodoscope, and a liquid krypton electromagnetic calorimeter were principal for this measurement. The spectrometer, which was used to detect charged products from kaon decays, was composed of four drift chambers and a dipole magnet. A beam pipe traversing the center of the detectors allowed undecayed beam particles and muons from decays of beam pions to continue their movement in vacuum.

The number of K_{l2} candidates is $N(K_{e2}) = 51{,}089$ and $N(K_{\mu 2}) = 15.56\times10^6$. The preliminary NA62 result was

$$R_K = [2.500 \pm 0.012(stat.) \pm 0.011(syst.)] \times 10^{-5} \quad (10)$$

$$= (2.500 \pm 0.016) \times 10^{-5}, \quad (11)$$

which is consistent with the SM expectation. The entire 2007-08 data sample should allow pushing the uncertainty of R_K down to $\Delta R_K/R_K$=0.4%.

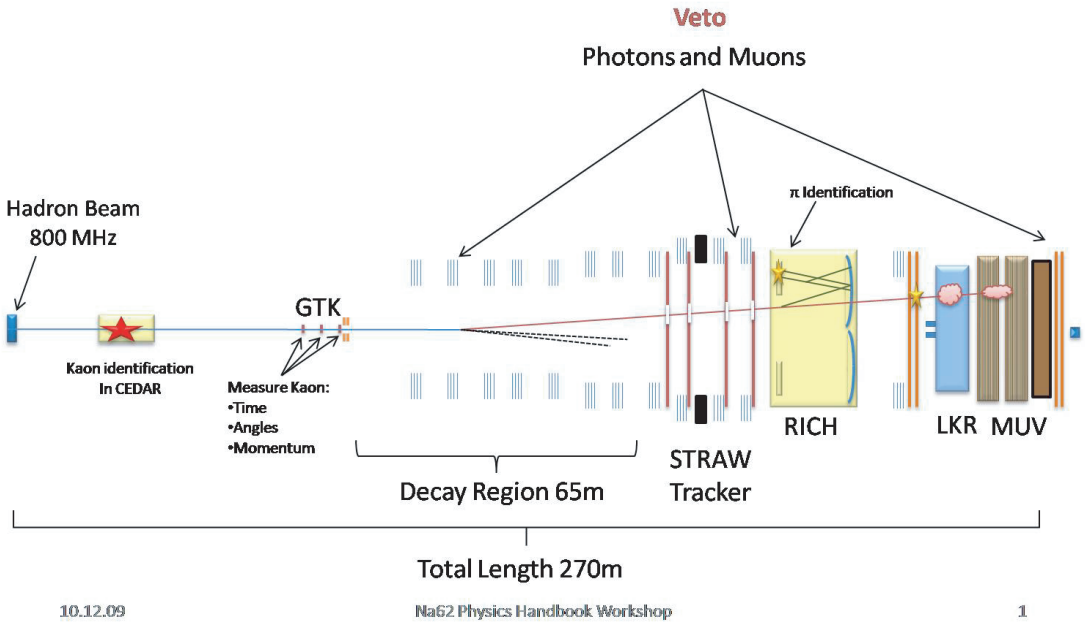

Figure 3: Cross sectional side view of the NA62 experiment. The beam line is capable of simultaneously delivering K^+ and K^- beams with a narrow momentum band. Among the subdetectors located downstream of the vacuum decay volume, a magnetic spectrometer, a plastic scintillator hodoscope, and a liquid krypton electromagnetic calorimeter are principal for the measurement.

2.1.2 KLOE at DAϕNE

The KLOE detector operated at DAϕNE which was the Frascati e^+ e^- collider system working at a center of mass energy $W \sim m_\phi \sim 1.02$ GeV. ϕ mesons were produced with a cross section of $\sim 3.1\mu$b and a transverse momentum of ~ 12.5 MeV/c directed toward the center of the collider rings. The coordinates of the beam's interaction point and the ϕ momentum were determined, run by run, with high precision from Bhabha scattering events.

The KLOE detector consisted of a large drift chamber (DC) surrounded by an electromagnetic calorimeter (EMC). A superconducting coil provides an axial magnetic field of 0.52 T. The DC, a cylinder of 4 m diameter and 3.3 m in length, provided a good measurement of the $K^\pm$ decays. The momentum resolution for tracks at large polar angle was $\sigma_p/p \sim 0.4\%$. The EMC was a lead-scintillating fiber sampling calorimeter consisting of a barrel and two endcaps covering 98% of the solid angle. The photon energy and timing resolutions were $\sigma_E/E \sim 5.7\%/\sqrt{E/\mathrm{GeV}}$ and $\sigma_t = 54$ ps$/\sqrt{E/\mathrm{GeV}} \oplus 50$ ps.

The R_K analysis was performed using the data collected for an integrated luminosity of 2.2 fb^{-1}. The number of collected events for $K^+ \to e^+\nu(\gamma)$ and $K^- \to e^-\nu(\gamma)$ were 7064±102 and 6750±101, respectively, 89.8% of which had $E_\gamma < 10$ MeV. The signal-to-background correlation was 20% and the χ^2/ndf was 113/112(140/112) for $K^+(K^-)$. The number of $K_{\mu 2}$ events was obtained from a fit to the missing mass (m_l^2) distribution to be 2.878×10^8 for $K^+_{\mu 2}$ and 2.742×10^8 for $K^-_{\mu 2}$. The fraction of background events under the muon peak is estimated from MC to be less than 1×10^{-3}. The difference between the K^+ and K^- counts was mainly due to K^- nuclear interactions in the material traversed.

They performed a comprehensive study of the $K_{e2\gamma}$ process. The ratio of the $K_{e2\gamma}$ and $K_{\mu 2}$ widths for photon energies smaller than 10 MeV was carefully checked to remove any systematic bias from the $K^{SD}_{e2\gamma}$ component. The R_K value was obtained to be

$$R_K = [2.493 \pm 0.025(stat.) \pm 0.019(syst.)] \times 10^{-5}, \tag{12}$$

which is also in agreement with the SM prediction. The experimental sensitivity was $\Delta R_K/R_K = 1.3\%$.

2.2 $R_\pi = \Gamma(\pi^+ \to e^+\nu)/\Gamma(\pi^+ \to \mu^+\nu)$ measurements

According to the PDG, the current world average of R_π is $(1.230 \pm 0.004) \times 10^{-4}$. Recently, the PEN [30] and PIENU [31] groups performed new experiments, and the analyses are currently under way. In general, the π^+ beam intensity is much higher than the K^+ intensity and the achievable experimental uncertainty is expected to be better for the R_π measurements compared to the R_K measurements.

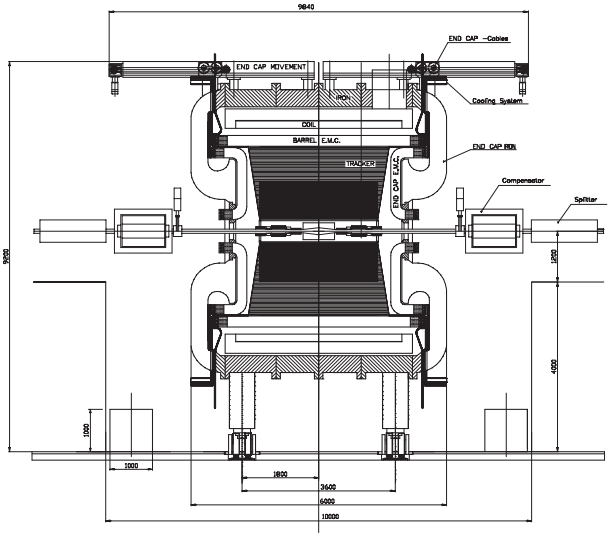

Figure 4: Cross sectional side view of the KLOE experiment. The KLOE detector consists of a large drift chamber (DC) surround by an electromagnetic calorimeter (EMC). The R_K analysis was performed by using the data collected for an integrated luminosity of 2.2 fb^{-1}.

2.2.1 PEN at PSI

A new measurement of $BR(\pi_{e2})$, the $\pi^+ \to e^+\nu(\gamma)$ decay branching ratio, is currently under way at the Paul Scherrer Institute. The present experimental result on $BR(\pi_{e2})$ constitutes the most accurate test of lepton universality available. The experimental accuracy, however, still lags behind the theoretical precision by over an order of magnitude.

The PEN experiment uses an upgraded version of the PIBETA detector system, described in detail in Ref. [32]. The PIBETA collaboration performed a series of rare pion and muon decay measurements [33, 34, 35]. The PEN apparatus consisted of a large acceptance ($\sim 3\pi$ sr) electromagnetic shower calorimeter (pure CsI, 12 radiation lengths thick) with non-magnetic tracking in concentric cylindrical multi-wire proportional chambers and a plastic scintillator hodoscope, surrounding a plastic scintillator active target. Beam pions passed through an upstream detector, had their energy reduced in the wedged active degrader (wAD), and stopped in the target. Combining the signals from the four wedges (a horizontal pair and a vertical pair) of the wAD provided information on the x-y position of the beam pion as it reached the active target.

Two engineering runs were completed in 2007 and 2008. All detector systems were performing to specifications, and $\sim 5 \times 10^6$ π_{e2} events were collected. The experiment continued with a major run in 2009, which was intended to double the existing data sample. Prior to the run, the wedged degrader was replaced by a single thin degrader, and a mini time projection chamber (mini-TPC). The position resolution, ∼1-2 mm,

achieved using the wAD, was limited by pion multiple scattering in the wedges. The new system improved the beam position resolution by about an order of magnitude, with the mini-TPC adding excellent directional resolution, as well. Both were needed to achieve improved systematics and provided better control of decays in flight.

2.2.2 PIENU at TRIUMF

The PIENU experiment at TRIUMF aims to reach an accuracy of five times better than the current world average value, in order to confront the theoretical calculation at the level of 0.1%. At this level, new physics at potentially very high mass scales could be revealed, or sensitive constraints on hypotheses could be obtained for new pseudoscalar, axial vector, or scalar interactions.

A 75-MeV/c π^+ beam from the TRIUMF M13 channel with an intensity of 50-100 kHz was identified by two beam counters and stopped in an active scintillator target. Beam tracking was provided by two wire chambers, and two silicon-strip counters located immediately upstream of the target. Positrons from the decays $\pi^+ \to e^+\nu$ and $\pi^+ \to \mu^+\nu$ and followed by $\mu^+ \to e^+\nu\nu$ decay ($\pi^+ \to \mu^+ \to e^+$ decay) were measured in the positron telescope. This consisted of a silicon-strip counter, two thin plastic counters, a third acceptance-defining wire chamber covering the front of a 48-cm-diameter, 48-cm-long single NaI(Tl) crystal (BINA), which provided the primary energy measurement. The solid angle of the telescope counters was 20%. Two layers of 8.5-cm-thick, 2×25-cm-long pure CsI counters surrounded the NaI to capture shower leakage. Analog signals from the plastic scintillators (Si strip, NaI and CsI detectors) were recorded by 500 MHz Copper ADCs (60 MHz VF48 ADCs).

The beamline and major detectors were tested and satisfied the requirements to achieve the goal of measuring the pion decay's branching ratio, to an accuracy five times better than the current world average value. The physics data taking was started in 2009.

2.3 Measurement of $\Gamma(K^+ \to \pi^0\mu^+\nu)/\Gamma(K^+ \to \pi^0 e^+\nu)$ ratio by the E246 collaboration

Our collaboration had considerable experience in determining the $\Gamma(K^+ \to \pi^0\mu^+\nu)/\Gamma(K^+ \to \pi^0 e^+\nu)$ ratio using the KEK-PS E246 data [36]. The physics motivation of this study is also a search for lepton universality violation, but the cancellation of the hadronic form factor does not work perfectly in these channels. Since the experimental and analysis procedures are very similar with this proposed experiment, we can perform the new experiment in which we can put our experience to good use. In fact, from this experiment, we learned many technical resources to reduce the systematic errors for the proposed experiment. In the following paragraphs, the measurement of $\Gamma(K^+ \to \pi^0\mu^+\nu)/\Gamma(K^+ \to \pi^0 e^+\nu)$ ratio is briefly described.

The experiment was performed at the KEK 12-GeV proton synchrotron. The details of the E246 detector system are well documented in [37]. We detected both a charged particle and a π^0 which enabled us to reconstruct the complete kinematics of a

K_{l3} event. This feature increased the reliability of the event selection. The spectrum distortion due to the detector acceptance was reduced, because of the rotational symmetry of the spectrometer and the large directional acceptance of the CsI(Tl) calorimeter. Moreover, the similarity of the $K_{\mu 3}$ and K_{e3} kinematics reduced the systematic error due to the imperfect reproducibility of the experimental conditions in the simulation. The measurement was carried out for two values of the central magnetic field strength, B= 0.65 and 0.90 T, which yielded a consistency check with regard to the spectrometer acceptance and energy loss estimation in the target. The $\Gamma(K_{\mu 3})/\Gamma(K_{e3})$ ratio could be deduced by the form

$$\Gamma(K_{\mu 3})/\Gamma(K_{e3}) = N(K_{\mu 3})/N(K_{e3}) \cdot \Omega(K_{e3})/\Omega(K_{\mu 3}), \tag{13}$$

where N is the number of accepted events after subtracting backgrounds and Ω is the detector acceptance obtained by a Monte Carlo simulation.

$K_{\mu 3}$ (K_{e3}) events were identified by analyzing the μ^+ (e^+) momentum with the spectrometer and detecting the two photons in the calorimeter. Charged particles from the target were tracked and momentum-analyzed using three multi-wire proportional chambers, as well as by an array of ring counters surrounding the target. $K_{\mu 3}$ and K_{e3} discrimination was carried out by time-of-flight measurement. The π^0 invariant mass and momentum vector were obtained from the photon information. In order to obtain the detector acceptance and to estimate the background fraction, Monte Carlo simulations were carried out for both the charged particle measurement by the spectrometer and the π^0 measurement by the calorimeter. Reproducibility of the experimental conditions by the simulation was carefully checked by mono-energetic π^+ and π^0 from the $K^+ \to \pi^+\pi^0(K_{\pi 2})$ decay.

The $\Gamma(K_{\mu 3})/\Gamma(K_{e3})$ value was obtained by calculating the weighted average of the results for B= 0.65 and 0.90 T data as,

$$R_{\rm exp} = \Gamma(K_{\mu 3})/\Gamma(K_{e3}) = 0.671 \pm 0.007(\text{stat.}) \pm 0.006(\text{syst.}). \tag{14}$$

The dominant sources of the systematic uncertainties was due to the ambiguity of the $K_{\pi 2}$ background fraction in the $K_{\mu 3}$ sample. By removing the μ-e universality assumption, the experimental determination of the $\Gamma(K_{\mu 3})/\Gamma(K_{e3})$ ratio ($R_{\rm exp}$) thus provided a numerical test of the μ-e universality of the form

$$g_\mu/g_e = (R_{\rm exp}/R_{\rm SM})^{1/2}, \tag{15}$$

where g_μ/g_e is the ratio of the weak coupling constants of the μ and e currents. Since μ-e universality leads to an identical weak coupling constant for $K_{\mu 3}$ and K_{e3}, any discrepancy from unity indicates a breakdown of the μ-e universality assumption. g_μ/g_e was obtained to be 0.978±0.014. Thus clear evidence for the μ-e universality violation was not observed.

2.4 Summary of the experimental situation

The lepton universality violation has not been discovered in both kaon and pion channels yet, as shown in Table 1 and Fig. 5. In the NA62 measurement, an in-

Table 1: Summary of the R_K and R_π measurements. The NA62, the KLOE, and proposed experiments are compared. Characteristics of the three experiments and the R_π experiments are summarized in the table.

Measurement	Kaon Beam	PID	R_K ($\times 10^{-5}$)	$\Delta R_K/R_K$
PDG08 [1]			2.45±0.11	5%
KLOE [13]	In-flight ($\phi \to K^\pm$)	E/p and TOF	2.493±0.025±0.019	1.3%
NA62 [14]	In-flight (p($K^\pm$) = 74 GeV/c)	E/p	2.500±0.016	0.4%
TREK	Stopped K^+	TOF and $\hat{C}$		0.2%
SM [38]			2.472±0.001	0.04%

Measurement	Pion Beam	PID	$R_\pi(\times 10^{-4})$	$\Delta R_\pi/R_\pi$
PDG08 [1]			1.230±0.004	0.3%
PIBETA [39]	stopped π^+	E/p	1.2346±0.0035±0.0036	0.4%
Britton et al. [40]	stopped π^+	$\pi \to \mu \to e$	1.2265±0.0034±0.0044	0.4%
PEN [30]	stopped π^+	E/p		$< 0.05\%$
PIENU [31]	stopped π^+	$\pi \to \mu \to e$		$< 0.1\%$
SM [1]			1.2353±0.0004	0.03%

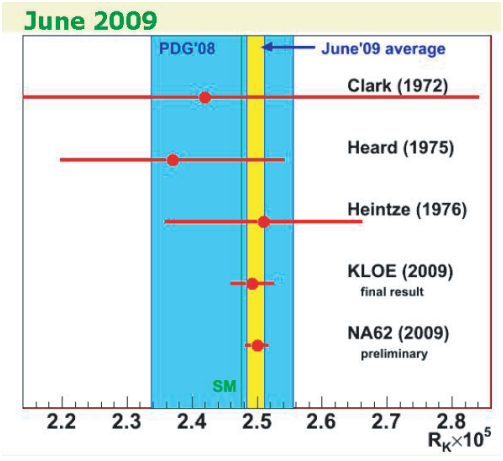

Figure 5: Results of the R_K measurements [14]. The current world average composed of three 1970s measurements. In the KAON09 conference, the NA62 and KLOE groups reported the latest results of the R_K values.

flight kaon beam with particle momentum from 15 to 65 GeV/c, was adopted, and kinematical separation of K_{e2} and $K_{\mu 2}$ at high momentum region (>40 GeV/c) was not achievable. Therefore, $K_{\mu 2}$ decay was the main background source in the K_{e2} sample. The probability of muon misidentification as electron was estimated to be $P(\mu \to e) \sim 3 \times 10^{-6}$, indicating non-negligible contribution compared with $R_K = 2.477 \times 10^{-5}$. Also, due to the experimental setup with a long distance in the beam direction, $K_{\mu 2}$ events with in-flight μ^+ decay contributed to the K_{e2} background. Therefore, the treatment of these backgrounds was one of the most difficult points to determine the R_K value in the NA62 experiment. Since low energy kaons from $\phi \to K^+K^-$ were used in the KLOE experiment, the kinematical resolution of K_{l2} decays were much better than that in NA62. However, the experimental result was dominated by the statistical error because of low-intensity of the kaon beam.

The NA62 and KLOE results are consistent with the SM within the errors, there is still room for improvement as the current data is only at the one percent level. On the other hand, the error weighted average of the two results is 2.499±0.014 which is deviating from the SM prediction at $\sim 1.9\sigma$ level. Possibly this result may be an indication of a new physics effect. Therefore, the current situation of the R_K measurement is very interesting and important, and strong motivation to improve the R_K experimental sensitivity naturally comes to our mind. We would like to propose a new R_K measurement using a stopped K^+ beam (see below).

3 Proposed experiment for the R_K measurement at J-PARC

3.1 R_K measurement using stopped kaons at J-PARC

At J-PARC, the TREK experiment [11] is aiming at measuring the transverse muon polarization in $K^+ \to \pi^0\mu^+\nu$ using a stopped K^+ beam with a sensitivity of $\Delta P_T \sim 10^{-4}$. The experiment will be performed by the upgraded E246 detector based on the 12-sector iron-core toroidal spectrometer and the CsI(Tl) calorimeter.

Here, we will discuss the significance to perform the R_K measurement using a sub-detector system of the TREK apparatus during the low-intensity period of the accelerator. It is possible to carry out the experiment with sufficient statistics using relatively low-intensity beam such as the 30 kW operation. Since the NA62 and KLOE groups adopted an in-flight-kaon decay method, the detection mechanism is different from the proposed J-PARC experiment and it is worth checking the R_K value using a different kinematical approach. In the case of a stopped-kaon beam experiment, the kaon beam history does not contribute to the systematics, which makes our result a valuable supplement to the literature data. Such independent measurements are complementary and comprehensive studies are very important to increase the experimental reliability. Taking into account these points, we would like to propose a new experiment to improve the sensitivity to $\Delta R_K/R_K \sim 2 \times 10^{-3}$ at

J-PARC, as shown in Table 1.

3.2 Overview of the proposed experiment

This experiment will be performed at J-PARC employing a stopped K^+ beam in conjunction with a 12-sector iron-core superconducting toroidal spectrometer. The K_{e2} ($P_{e^+} = 247$ MeV/c) and $K_{\mu 2}$ ($P_{\mu^+} = 236$ MeV/c) events will be accepted by analyzing charged particle momenta using the spectrometer. In order to compare the experimental R_K value with the SM prediction, the internal bremsstrahlung process in radiative $K^+ \to e^+\nu\gamma$ ($K^{IB}_{e2\gamma}$) and $K^+ \to \mu^+\nu\gamma$ ($K^{IB}_{\mu 2\gamma}$) decays has to be included into the K_{e2} and $K_{\mu 2}$ samples, respectively. Schematic cross sectional side and end views of the detector system are shown in Fig. 6. The R_K value is derived from the numbers of the accepted K_{e2} and $K_{\mu 2}$ events by correcting for the detector acceptance.

A separated 800-MeV/c K^+ beam is extracted using the J-PARC K1.1BR beam line. The beam is slowed down by a degrader and stopped in a position-sensitive fiber target. Charged particles from the target are tracked and momentum-analyzed using one GEM detector (C1) and three multi-wire proportional chambers (C2, C3, C4) in each toroidal sector. The K_{e2}, $K_{\mu 2}$, and their radiative decays are collected for central magnetic field of the spectrometer, $B = 1.4$ T. The C1 element is placed at the outer surface of the muon hole of the CsI(Tl) calorimeter. The C2 and C3-C4 chamber are set at the entrance and exit of the magnet gaps, respectively. In order to remove K_{e3} and $K_{\mu 3}$ backgrounds, K_{e2} and $K_{\mu 2}$ events are identified by requiring the e^+ and μ^+ momentum to be higher than the K_{e3} and $K_{\mu 3}$ endpoints ($P_e^{\rm Max} = 228$ MeV/c, $P_\mu^{\rm Max} = 215$ MeV/c), as shown in schematically Fig. 7. Particle discrimination between e^+ and μ^+ is carried out using an aerogel Cherenkov counters and by measuring the time-of-flight (TOF) between the TOF1 and TOF2 scintillation counters. The TOF1 scintillator surrounds the fiber target and TOF2 is located behind C4. The γ detector, an assembly of 768 CsI(Tl) crystals, covers 75% of the total solid angle. Since photons produce electro-magnetic showers, their energy is shared among several crystals. The photon energy and hit position are obtained by summing the energy deposits and by determing the energy-weighted centroid, respectively. The 0γ and 1γ events are accepted as K_{l2} or $K_{l2\gamma}$ samples. A Pb-plastic sandwich detector as the gap photon counter (GP counter) is set at the outer radius of the magnet pole to monitor photons passing through the photon detector holes.

The number of accepted events, $\tilde{K}_{e2} = K_{e2} + K^{IB}_{e2\gamma}$ and $\tilde{K}_{\mu 2} = K_{\mu 2} + K^{IB}_{\mu 2}$, after background subtraction can be described as,

$$N(\tilde{K}_{e2}) = N_K \times \Omega(\tilde{K}_{e2}) \times BR(\tilde{K}_{e2}) \quad (16a)$$

$$N(\tilde{K}_{\mu 2}) = N_K \times \Omega(\tilde{K}_{\mu 2}) \times BR(\tilde{K_{\mu 2}}). \quad (16b)$$

Here N_K is the number of stopped kaon in the target, BR is the branching ratio, and Ω is the acceptance. Therefore, the $R_K \equiv \Gamma(\tilde{K}_{e2})/\Gamma(\tilde{K}_{\mu 2})$ ratio can be obtained by making the ratio of the accepted $\tilde{K}_{e2}$ to $\tilde{K}_{\mu 2}$ event numbers corrected for the detector

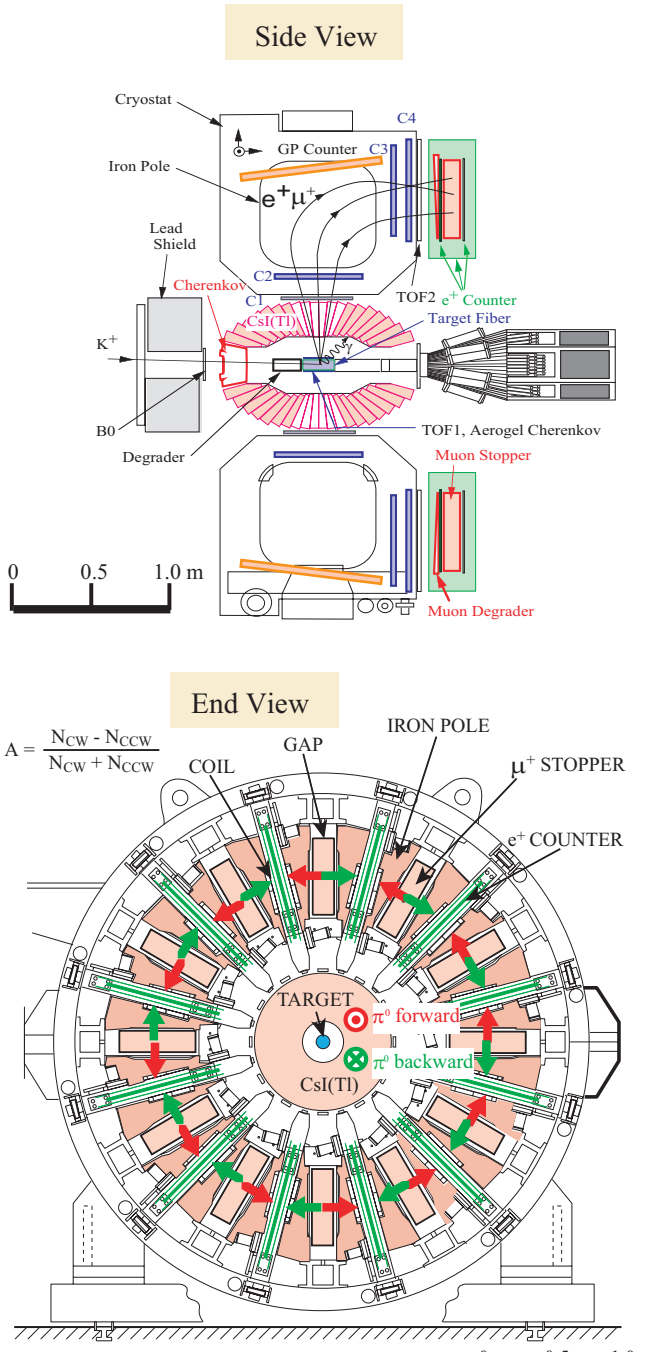

Figure 6: Cross sectional end and side views of the setup for the R_K experiment and the heavy neutrino search. The momentum vectors of charged particles and photons are determined by the toroidal spectrometer and the CsI(Tl) calorimeter, respectively. The assembly around the target system is shown in Fig. 12. The red and green arrows shown in the end view are the directions of P_T by tagging forward and backward going π^0s, respectively, for the T-violation experiment (TREK).

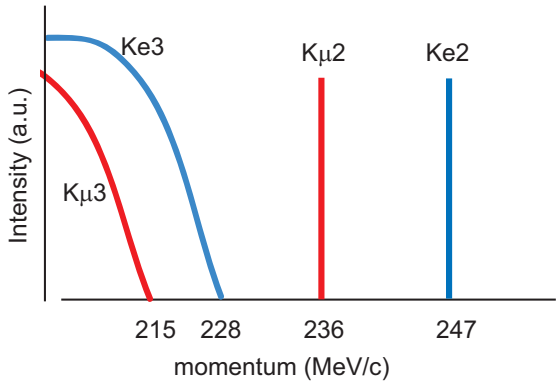

Figure 7: Schematic momentum spectra of K_{l2} and K_{l3}. The accessible region in this experiment is above the K_{l3} endpoints. The K_{l2} and radiative $K_{l2\gamma}$ momenta are imposed to be higher than the endpoints of K_{l3}.

acceptance as,

$$\Gamma(\tilde{K}_{e2})/\Gamma(\tilde{K}_{\mu 2}) = BR(\tilde{K}_{e2})/BR(\tilde{K}_{\mu 2}), \quad (17)$$

$$= N(\tilde{K}_{e2})/N(\tilde{K}_{\mu 2}) \cdot \Omega(\tilde{K}_{\mu 2})/\Omega(\tilde{K}_{e2}). \quad (18)$$

The detector acceptance is calculated by Monte Carlo simulation. It is to be noted that the analysis procedure is exactly identical between $\tilde{K}_{e2}$ and $\tilde{K}_{\mu 2}$ except for the particle identification by TOF in order to reduce the systematic error due to the analysis. Details of the R_K determination will be described in Section 6.2.

3.3 Details of the experiment

Details of the E246 detector system are well documented in Ref. [37] and the necessary upgrades from the E246 system have already been discussed in considerable detail in the TREK proposal and FIFC report [11]. Again we should emphasize that the proposed experiment will be performed using a subset of the TREK apparatus and we do not need to complete the entire TREK system. Here we would like to briefly summarize each detector element as follows [1].

3.3.1 K1.1BR beam line

A separated K^+ beam with low momentum (0.8 GeV/c) from the K1.1BR will be used, where also the TREK experiment will be performed. The layout of the beamline is shown in Fig. 8. Details of this beam are described in the report submitted to the FIFC in 2007 [11]. The beam optics were designed by J. Doornbos of the TREK

[1] The μ^+ polarimeter for the heavy neutrino search will be installed in the R_K measurement. The experimental data of heavy neutrinos in the high momentum region will be simultaneously taken and analyzed. Details are described in Section 10.

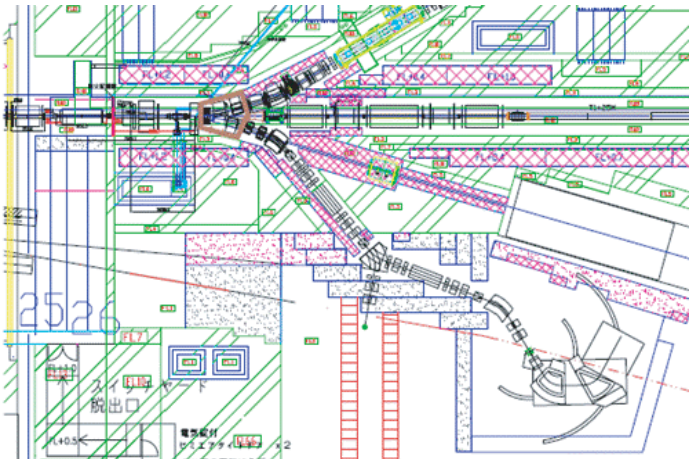

Figure 8: Layout of the K1.1BR beamline. Although there will be only a single electro-static separator (ESS), the existence of a vertical focus (IFY) before the ESS will play an important role to increase the K/π ratio. Details of this beam is described in the report submitted to FIFC in 2007 [11].

collaboration by keeping the upstream layout design of K1.1, as its short branch with a total length of 20.3 m. Although there will be only a single electro-static separator (ESS), the existence of a vertical focus (IFY) before the ESS will play an important role to increase the K/π ratio. The horizontal focus after the sector type magnet B3 is also essential to suppress background pions. The K^+ beam intensity can be evaluated from the beamline acceptance of 4.5 msr%$[\Delta p/p]$, and the comparison with LESB3 at BNL-AGS, to be 2×10^5/s at 30 kW of accelerator beam power. We will be able to obtain a round beam spot at the final focus (FF) with a full width at half maximum of 1.0 cm horizontally and vertically. The momentum bite is $\pm 3\%$. The spot is free from dispersion (R_{16}), but with finite R_{26}, [2] on which the design of the new target is based. The parameters of the K1.1BR beamline are summarized in Table 2.

The beamline will be completed this summer and commissioned in October 2010. The TREK collaboration is responsible for the beam tuning. This initial version of the beamline is modified from the original optics design in a few points mainly due to tight budgetary constraints. For the ESS the old K5 separator (with 2.0 m length) is recycled in place of the final 2.5 m one. The last sector bending magnet B3 is a 45 degree bender instead of 50 degrees. The necessity of 2.5 m thick iron shielding makes the final focus point far from the last element Q8. After K1.1BR beamline commissioning, these three modifications should be reverted back to the original design for this proposed experiment and for TREK, so as to attain the desired K^+ intensity and K/π ratio.

[2] R_{16} and R_{26} are the elements of the 1st-order transport matrix. R_{16} is the measure of horizontal dispersion, and R_{26} is the measure of focusing point depth in the experimental target.

Table 2: Main parameters of K1.1BR. A separated K^+ beam with low momentum (0.8 GeV/c) from the K1.1BR beamline will be used in the proposed experiment, where the TREK experiment is also performed. Details of this beam are described in the report submitted to FIFC in 2007 [11].

Operation beam momentum p	800 MeV/c
Length of the beam line	20.3 m
K^+ intensity at p	2×10^5/s
K^+/π^+ ratio at p	$\sim$2
Beam spot size at final focus	1 cm [H], 1 cm[V] (FWHM)
R_{16}, R_{26}	R_{16} <0.1 cm/%, R_{26}=17.6 mr/%
Acceptance	4.5 msr% ($\delta p/p$)
Momentum bite	$\pm$3%

3.3.2 Kaon trigger and stopping target

In order to trigger only on kaons in the beam, we have prepared a Fitch-type differential Cherenkov counter, whose structure is as shown in Fig. 9 and whose parameters are given in Table 3. Kaons and pions injected into a 40 mm-thick acrylic radiator emit Cherenkov light with characteristic polar angle according to each velocity. The refraction index of the radiator is optimized so that Cherenkov light from pions is totally reflected at the rear surface while that from kaons in the chosen momentum range is emitted from the rear surface. The Cherenkov light from pions is reflected by a mirror around the radiator and detected by an inner photomultiplier (PMT) ring (π-ring). The light from kaons is reflected by a backward parabolic mirror and detected by an outer PMT ring (K-ring). Each ring is composed of 14 PMTs with a Winston cone at the entrance.

This counter is very similar to the counter developed for the KEK E246 experiment, but the momentum range is different. The designed momentum range is 740$-$800 MeV/c, whereas the original momentum range was 620$-$700 MeV/c. We modified the focal length of the K-ring parabolic mirror to compensate for the Cherenkov emission angle shift due to this momentum difference. The PMT hit multiplicity in each ring is used for an online trigger. The trigger condition is evaluated by a computer simulation as shown in Fig. 10. Using the threshold level of a multiplicity N $\geq$ 7, it is expected that we can achieve more than 99% trigger efficiency for K^+s, while the π^+ misidentification as K^+ is negligible.

In order to localize the K^+ stopping point (decay vertex) and also to help tracking of decay particles, the K^+ stopping target is an active bundle of scintillating fibers. Its design is now more advanced from that in the original proposal and in the FIFC report [11]. The bundle is made of about 500 pieces of 3 mm rectangular scintillating fibers with a length of 20 cm forming a 7 cm diameter rod. In each fiber a thin wavelength shifter (WLS) fiber is embedded in a groove and the light through the

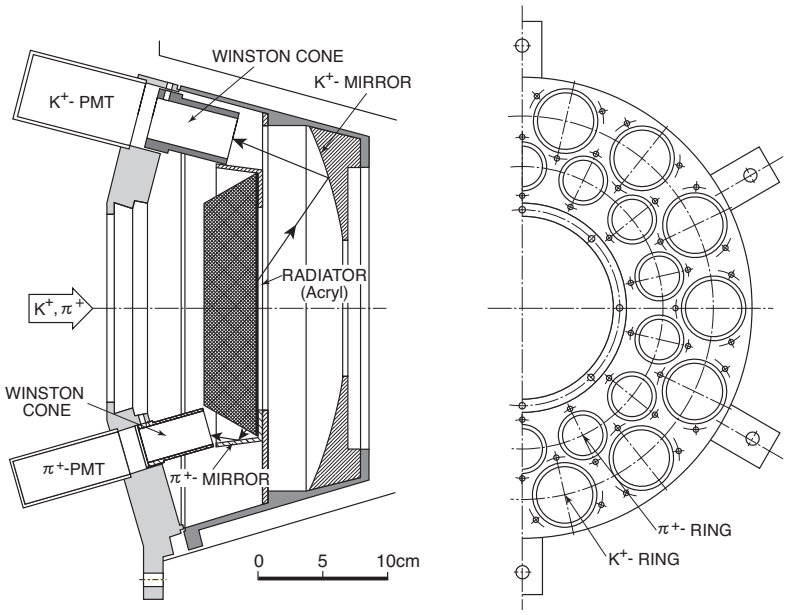

Figure 9: Side view and end view of the beam Cherenkov counter. The beam with 740−800 MeV/c momentum emits the Cherenkov light with an angle of 38° for K^+ and 47° for π^+. The critical angle of the radiator for the total reflection is 42.2°.

about 1 m WLS fiber is read by a multi pixel proportional counter (MPPC) i.e. a Geiger mode APD from Hamamatsu. According to a test and also a simulation calculation, an input of a sufficient number of photons into the MPPC is expected. The fine segmentation is also necessary to suppress backgrounds in reconstructed trajectories. The construction of the target system has been funded in Canada and the mechanical design has already been started at TRIUMF.

3.3.3 Spectrometer and tracking

The heart of the muon spectrometer is a superconducting toroidal magnet with 12 iron sectors separated by 12 gaps [41]. Each iron sector is magnetized by a superconducting coil, and a field up to 1.8 T can be excited across the 20-cm uniform gaps. In the proposed experiment a central field strength of 1.4 T is employed. The field geometry is nearly dipole with some toroidal component superposition. Charged particles from the target located in the center of the magnet are bent by ∼90 degrees and tracked by the GEM and MWPCs at the entrance and exit of the gap. The field map necessary for tracking was calculated using a 3-dimensional code TOSCA [42]. The validity of the map was checked using the measured monochromatic momentum spectra of muons from $K_{\mu 2}$ and pions from $K_{\pi 2}$. Charged particles from the target are tracked and momentum-analyzed using one GEM chamber and three MWPCs, as shown in Fig. 11 and Table 4. Helium bags in the magnet are installed to reduce multiple scattering effects.

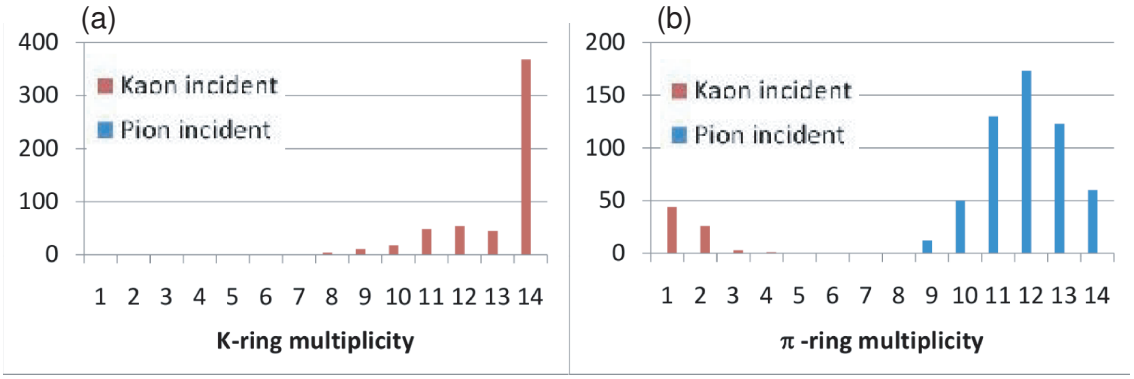

Figure 10: Distribution of PMT-hit multiplicity. The left figure is for the K-ring multiplicity and the right one is for the π-ring multiplicity. By setting a threshold for the PMT multiplicity to 7, the K^+ efficiency is expected to be higher than 99%. The π^+ misidentification probability as K^+ is less than 1%.

Table 3: Main parameters of the beam Cherenkov counter. The K^+ momentum is expected to be 740−800 MeV/c. The K^+ efficiency is obtained to be higher than 99% by setting the threshold level of a PMT multiplicity.

Parameter	Value
Accepted K^+ momentum	740−800 MeV/c
Radiator material	acrylic ($n_D = 1.49$)
Effective aperture	12-cm diameter
Number of PMTs	14 for kaon and 14 for pion
K^+ efficiency	>99%
π^+ misidentification as K^+	<1%

Table 4: Summary of the tracking elements for the track reconstruction of charged particles. Charged particles from the target are momentum-analyzed using one GEM and three MWPCs. For the efficiency measurement of each element, a redundant condition for the track reconstruction is required.

Trackers	Type	Effective area (mm^2)	Comment
C1	planar GEM	450×150	newly-made chamber
C2	planar MWPC	560×160	E246 reuse
C3	planar MWPC	640×200	E246 reuse
C4	planar MWPC	720×200	E246 reuse

We will add newly-constructed planar tracking elements (C1) at the outer surface of the muon hole of the CsI(Tl) calorimeter which will be based on GEM technology [3]. A GEM detector for charged particle tracking represent a new generation of position-sensitive counters, which is reasonably cheap, radiation-hard, and well suited to be operated in high-rate environments.

For the C2, C3, and C4 chambers, we will reuse the existing MWPC chambers which were used in the previous E246 experiment. They are placed at the entrance (C2) and exit (C3, C4) of each magnet gap, as shown in Fig. 11. Since the C2, C3, and C4 chambers have to be operated under the strong field of the spectrometer, a planar MWPC with cathode readout was chosen. The anodes are 20-μm gold-plated tungsten wires strung with 2 mm pitch along the momentum-sensitive directions. The width of the strip is 9 mm in width and the spacing between strips is 1 mm. Typical position resolutions are $\sim$200 μm. Parameters of the MWPC chambers are summarized in Table 4.

Any efficiency difference of GEM and MWPCs between e^+ and μ^+ would introduce a systematic uncertainty into the R_K measurement. In this proposed experiment, the redundancy in the number of chambers allows to directly determine the chamber efficiencies. In principle, it is possible to reconstruct the particle trajectory using three tracking elements. Since four tracking elements are used for the track reconstruction, the efficiency can be determined by comparing signals from a particular element with the tracks reconstructed by others. For example, C1 signals are checked by reconstructing particle tracks from C2, C3, and C4. Details are discussed in Section 7.2.3.

3.3.4 Particle identification

Because of the huge difference of the K_{e2} and $K_{\mu 2}$ branching ratios ($BR(K_{e2})/BR(K_{\mu 2}) \sim 10^{-5}$), reliable discrimination of K_{e2} is very important to remove the $K_{\mu 2}$ contamination. Also, the detection efficiency for the e^+ and μ^+

[3]It is to be noted that a new cylindrical chamber (C0) around the K^+ target has been proposed for the TREK experiment. However, C0 is not used in the proposed experiment here, and a new aerogel Cherenkov counter will be installed at this position (see below).

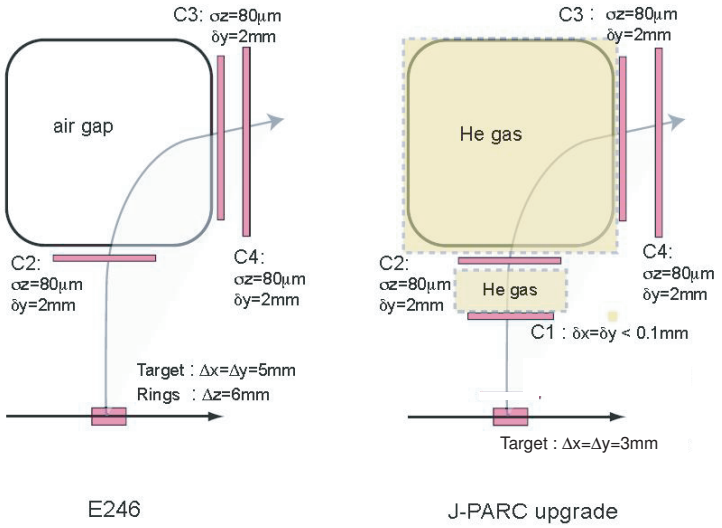

Figure 11: Experimental configuration of the charged particle tracking for the previous E246 experiment and the proposed experiment. Charged particles from the target are tracked and momentum analyzed using one GEM and three MWPCs.

measurement should be controlled with an accuracy better than 10^{-3}. In order to satisfy these conditions, both a threshold type aerogel Cherenkov counter and a TOF measurement between TOF1 and TOF2 will be adopted.

TOF measurement Particle discrimination between the e^+ and μ^+ mainly for the low energy region is carried out by a time-of-flight measurement between TOF1 and TOF2. TOF1 is located surrounding the K^+ target system and TOF2 is located at the exit of the spectrometer (behind C4), as shown in Fig. 6. The main parameters of the counters for the TOF measurement are summarized in Table 5. The time difference between the e^+ and μ^+ from the K_{e2} and $K_{\mu 2}$ decays is approximately 0.5 ns for a typical trajectory. The uncertainty of the light propagation time from the particle hit position to the photo multiplier is suppressed by reading signals from both ends of the TOF counters. Since the TOF resolution in the E246 experiment was only ∼260 ps due to one-end PMT readout for the low momentum e^+, μ^+, and π^+ separation, the existing system is not suited for the proposed experiment. For optimal separation of K_{e2} and $K_{\mu 2}$, a timing resolution of $\sigma_t = 100$ ps for the TOF measurement is needed. It is not impossible to achieve this resolution using the current TOF technology, but it is not very easy. We will construct the new TOF system with a timing resolution of $\sigma = 100$ ps and install the aerogel Cherenkov counter for e^+ discrimination. Note, the TOF2 counters are used for the $K_{\mu 2}$ trigger and TOF1 counters are used as the detector to define the fiducial region of the K^+ stopping target in the beam direction.

Table 5: Main parameters of TOF1 and TOF2. The TOF resolution is expected to be $\sqrt{60\ \mathrm{ps}^2 + 80\ \mathrm{ps}^2} \sim 100$ ps.

	size (mm^2)	thickness (mm)	scintillator	PMT	resolution (ps)
TOF1	200×30	10	BC404	H3171-03	60
TOF2	800×200	20	BC404	H1161	80

e^+ Cherenkov counter A threshold type aerogel Cherenkov counter is used for the e^+ identification, which is installed surrounding the TOF1 counter, as shown in Fig. 12. This type of a Cherenkov counter is widely used for particle identification by many experiments such as BELLE [4]. The β value of μ^+ from $K_{\mu 2}$ is 0.913, therefore a Cherenkov radiation material with refractive index (n) from 1.01 to 1.095 is necessary to discriminate e^+ and μ^+. Normally, the refractive index of aerogel ranges from 1.01 to 1.05, and an increase of Cherenkov photons with increasing refractive index is expected, so that we choose an aerogel material with n of 1.05. The typical number of Cherenkov photons per e^+ passing through this counter is estimated to be about 500, and a wavelength region of photons measured by this counter ranges from 350 nm to 700 nm. An opening angle of Cherenkov radiation with respect to the e^+ trajectory is as small as 35.5°. The number of reflections at the inner surface of the aerogel wrapping material can become large, corresponding to a long path length of Cherenkov photons. Thus the minimization of the path length for the Cherenkov photon transport to the photon detector is a key issue to maximize number of photons emitted from the aerogel. We will optimize material and structure of surfaces of the aerogel wrapping by computer simulations. Photons emitted from the aerogel are focused onto a window of a photo sensor by the Winstone cone. For the moment an avalanche photodiode type sensor is planned to be used as a photo sensor to work well in a magnetic field.

The performance of this Cherenkov counter is the most critical factor for the proposed experiment; it is essential to achieve reliable e^+ triggers with nearly 100% efficiency and negligible misidentification for any possible crossing track of e^+. A prototype is proposed to be made as soon as possible and tested at an e^+ beam facility.

3.3.5 Photon detector

The E246 CsI(Tl) calorimeter with 768 crystals will be used. The readout system in terms of PIN photo-diodes is, however, too slow and should be replaced with a new faster system, as was described in the E06 (TREK) proposal. The PIN system is also crucial to apply for the 30 kW beam power. In the TREK proposal we discussed the adoption of an avalanche photo-diode (APD) with an internal gain of about 100. The APD signal is to be amplified with a conventional current amplifier with a moderate gain. A test of one-module using a 5×5 mm^2 APD has already been performed using

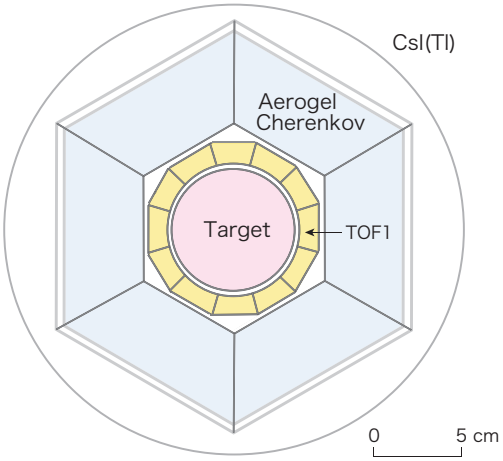

Figure 12: The experimental configuration of the aerogel Cherenkov counter. The counters are placed surrounding the TOF1 counter system.

a positron beam, and high-rate performance and the separability of pileup signals were demonstrated and reported to one of the previous PAC meetings [11].

Recently, however, the development of a micro-pixel APD (MAPD) in Geiger mode operation is significant, and a product of the same size (5×5 mm^2) with rather high internal gain became commercially available from Zacotek Co. If we can apply this MAPD to our CsI(Tl) detector, we will be able to lower the photon detection energy threshold significantly, which has an essential meaning for the measurement of radiative processes. However, because each micro pixel has a long dead time of a few μs, the high rate performance is a concern. Very recently in June 2010, we carried out a beam-test experiment at the Electron-photon Experimental Facility of Tohoku University using a positron beam for a 3×3 matrix of CsI(Tl) modules in order to compare their readout performances, in particular at high event rate. Each module was equipped with one APD and one MAPD, and the amplifiers developed and mass-produced at INR (Moscow) were employed for both elements. The accumulated data are now being analyzed, and basic results will be presented in the coming PAC meeting.

3.3.6 Gap photon counter

The gap photon (GP) counter is a Pb-plastic sandwich detector which is already installed at the outer radius of the magnet pole to monitor photons passing through the photon detector holes for charged particles, as shown in Fig. 6. The GP counter has a thickness of 2.6 radiation lengths and about 40% of the photons escaping through the hole can be monitored by the GP counters. The remaining photons hit the magnet pole, supporting device, etc. The GP counter can be used as a photon veto counter.

Table 6: Detectors and readout devices

Detector	Number of channels	Readout device	Readout system
TOF	48	HR-TDC	TKO
Counters/PMT	120	ADC/TDC	TKO, COPPER
Target/MPPC	489	SCA/FADC	PC
MWPC	500	ADC	TKO
Aerogel Cerenkov/APD	12	100 MHz FADC	VME
GEM	1700	APV25	VME
CsI(Tl) photon detector	768	FADC	VME

3.3.7 Electronics and data acquisition

The data acquisition (DAQ) subsystems of the detectors are not unified by the effective readout of its detectors. The PMT signals are read by the traditional TKO system and KEK-VME/COPPER system at the early stage of the experiment. The TKO system will be replaced by high-speed readout devices. The MPPC and semiconductor signals are read out by a 100 MHz sample flash-ADC based readout system. The target has a switched capacitor array (SCA) based readout system which was developed for the T2K TPC readout [9]. The GEMs have a special readout system based on the APV25 frontend chip and FPGA technology. The APV25 is a 128-channel readout chip originally developed for CMS. The readout devices are summarized in Table 6.

DAQ system integration using Network We will use the common network to integrate many different DAQ subsystems. The DAQ system has controllers which can connect to the network. The performance of the network interfaces and network switches are sufficient to transfer all detector data. The estimated data rate is around 20 MB/s. Current network technology can handle over 100 MB/s of data flow. The common high-speed storage devices such as the RAID hard disk drive, can record data faster than 100 MB/s. Therefore, we design a network based distributed DAQ system to integrate various readout systems. An overview of the network based distributed DAQ system is shown in Fig. 13.

Event synchronization The asynchronous distributed data acquisition requires a tagging mechanism of the event fragments to synchronize each event. We use a unique number for the event fragments of the readout subsystem in each trigger. We use a trigger distribution system for this purpose. The system consists of a master trigger module (MTM) and some trigger receiver modules (RM) and a signal repeater unit. The MTM processes a unique event number and the trigger signals, and distributes it to each RM using a pair of CAT-7 standard STP network cables. Each DAQ subsystem reads the event number and adds it to the event fragments. The repeater

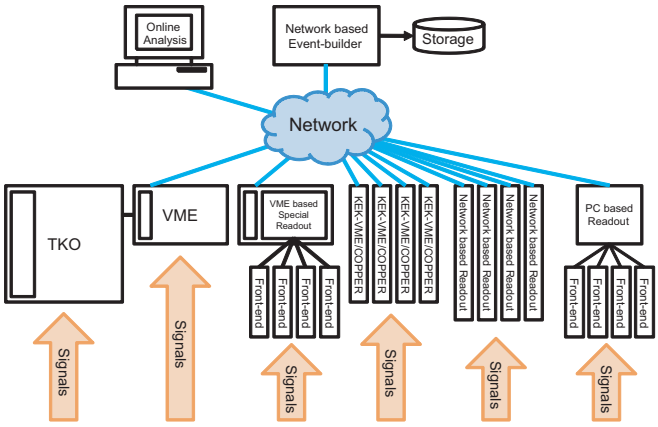

Figure 13: Network DAQ system

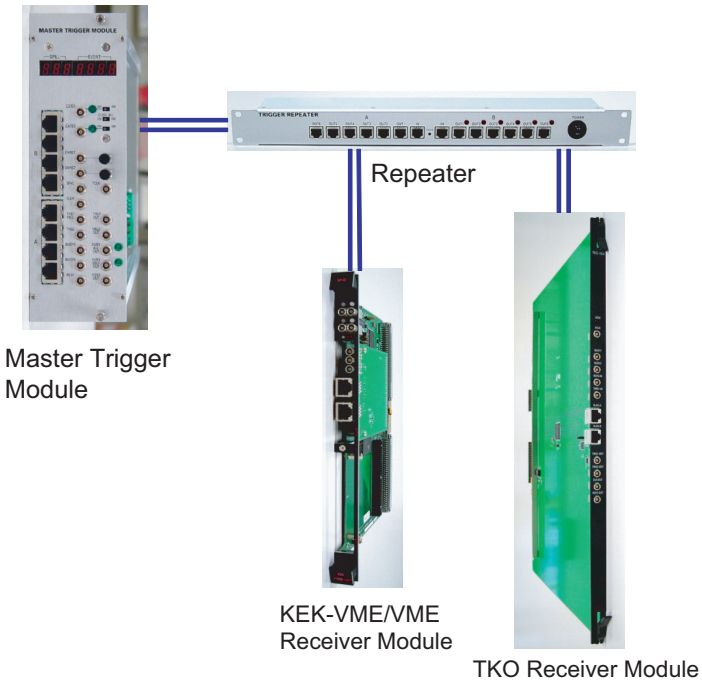

Figure 14: Pictures of the trigger distribution modules for the event synchronization.

relays and divides signals carrying the trigger and the event number. The system has been developed for the hadron experiments of J-PARC Hadron Hall, and works well. Fig. 14 shows pictures of the trigger distribution modules.

3.3.8 R_K measurement at J-PARC

The K^+ decay channels appearing in this proposal are shown in Table 7. According to the PDG, the current world average of the K_{e2} and $K_{\mu 2}$ branching ratio are $(1.55 \pm 0.07) \times 10^{-5}$ and $(63.51 \pm 0.18) \times 10^{-2}$, respectively. The relative intensity normalized

Table 7: K^+ decay channels appearing in this proposal. The branching ratio of $K_{\mu 2}$ and $K^{IB}_{e2\gamma}$ is about 40000 and 0.1 times as strong as that of K_{e2}, and they have to be taken at the same time. This feature indicates the special nature of this experiment.

Decay mode	Branching ratio	Relative intensity	Momentum(MeV/c)
$K^+ \to e^+\nu$	1.6×10^{-5}	1	247
$K^+ \to \mu^+\nu$	6.3×10^{-1}	40000	236
$K^+ \to e^+\nu\gamma(IB)$		~ 0.1	
$K^+ \to e^+\nu\gamma(SD)$	1.5×10^{-5}	~ 1	
$K^+ \to e^+\nu\pi^0$	4.8×10^{-2}	3000	$<$228
$K^+ \to \mu^+\nu\gamma$	5.5×10^{-3}	400	
$K^+ \to \mu^+\nu\pi^0$	3.2×10^{-2}	2000	$<$215

to $K^+ \to e^+\nu$ is also given. The branching ratio of $K_{\mu 2}$ and $K^{IB}_{e2\gamma}$ is about 40000 and 0.1 times as strong as that of K_{e2}, and all decay channels described in Table 7 have to be taken at the same time. This indicates the special nature of the proposed experiment. The spectrometer magnetic field is adjusted to maximize the detector acceptance, $B = 1.4$ T. The $K^{IB}_{e2\gamma}$ decay has not been observed yet and we expect to observe it for the first time. Since the helicity suppression mechanism does not work for $K^{SD}_{e2\gamma}$, the $K^{SD}_{e2\gamma}$ branching ratio is almost the same as K_{e2}, as shown in Table 7, which is also recorded in the data.

An event is accepted when the following mixed trigger requirements are satisfied:

$$TRG \otimes C_e \oplus TRG \otimes SC. \tag{19}$$

The former and the latter are the triggers for K_{e2} and $K_{\mu 2}$, respectively, and

$$TRG = C_K \otimes \Sigma_i^{12}[TOF2_i \otimes (TOF1_{i-1} \oplus TOF1_i \oplus TOF1_{i+1})] \otimes (0\gamma \text{ or } 1\gamma) \tag{20}$$

where

- C_K is the multiplicity condition of the Cherenkov K-ring > 7,
- $TOF2_i$ is the counter TOF2 hit condition in the ith magnet sector,
- $TOF1_{i-1} \oplus TOF1_i \oplus TOF1_{i+1}$ is the hit condition in the ith TOF1 counter or its adjacent counter,
- 0γ and 1γ are 0 and 1 photon clusters, respectively, in the CsI(Tl) calorimeter.
- C_e is the aerogel Cherenkov counter hit in the ith magnet sector [4],

[4]The aerogel Cherenkov detector is now under development. We have an option not to use signals from the e^+ Cherekov detector for trigger.

Table 8: Reduction factors of the trigger rate in each step. The K^+ beam intensity is assumed to be 2.2×10^5. Exact definition of $\Sigma_i^{12}TOF1_i$ is explained in the text. SC is adopted to be 0.001.

Step	Condition	Rate at $2.2 \times 10^5 K^+$/s
1	C_K	2×10^5
2	$C_K \otimes \Sigma_i^{12} TOF1$	4×10^4
3	$C_K \otimes \Sigma_i^{12}(TOF1 \otimes TOF2_i)$	2.5×10^3
4	$C_K \otimes \Sigma_i^{12}(TOF1 \otimes TOF2_i) \otimes (0\gamma$ or $1\gamma)$	2.5×10^3
5	$C_K \otimes \Sigma_i^{12}(TOF1 \otimes TOF2_i) \otimes (0\gamma$ or $1\gamma) \otimes SC$	2.5
6	$C_K \otimes \Sigma_i^{12}(TOF1 \otimes TOF2_i) \otimes (0\gamma$ or $1\gamma) \otimes C_e$	0.06

- SC is a prescaling rate.

Here C_K is necessary to discriminate K^+ from π^+ by the beam Cherenkov counter. The $TOF1$ and $TOF2$ requirements are to confirm that a charged particle has been transported through the toroidal spectrometer. (0γ or 1γ) is to pick up events with 0γ and 1γ hits by the calorimeter. C_e is the requirement for a e^+ hit in the aerogel Cherenkov counter. A typical TRG rate is 2.5 k trigger/s which is subject to the $K_{\mu2}$ rate. Adopting the SC parameter to be 0.001, we can expect the trigger rate to be 2.5 trigger/s, where the trigger from K_{e2} is still negligible. This trigger rate can be easily controlled by changing the SC value to match the DAQ capability. Since all decay modes are collected simultaneously, normalization of the stopped kaon number does not contribute to the systematic error at all.

The proposed experiment will be performed during the low-intensity period of the J-PARC Main Ring (MR). The 30 kW operation of the MR, a kaon beam intensity of 220 kHz at the K^+ target position is expected. The singles rate of each detector element is summarized in Table 9, which was estimated from the E246 experiment by scaling the K^+ and π^+ intensities. Since the π^+ beam intensity can be significantly reduced compared with the E246, the single rates in the proposed experiment are expected to be much lower than those in E246. A total of 250 k K_{e2} events will be collected in 50 days of data collection, and the corresponding estimated statistical error will be $\Delta R_K/R_K = 0.2\%$ (see Section 7.1).

4 Analysis

K_{l2} events will be identified by analyzing the charged particle momentum with the toroidal spectrometer. Radiative decay is required to be one photon hit in the CsI(Tl) calorimeter in addition to the normal charged particle analysis. The e^+ and μ^+ momenta will be imposed to be higher than the K_{e3} and $K_{\mu3}$ endpoints, respectively. K_{e2} and $K_{\mu2}$ decays will be discriminated by the aerogel Cherenkov counter and

Table 9: Expected single rates. The K^+ beam intensity is assumed to be 2.2×10^5. They were estimated from the E246 experiment by scaling the K^+ and π^+ intensities.

Detector	single rate
CsI(Tl) calorimeter	$< 5 \times 10^3$
one CsI(Tl) crystal	< 10
GEM (C1), MWPC (C2, C3, C4)	$< 2 \times 10^3$
K^+ stopping target	$< 2 \times 10^5$
one fiber in K^+ stopping target	$< 2 \times 10^2$
TOF2 counter	$< 2 \times 10^3$

time-of-flight between TOF1 and TOF2. The most dominant background will be the structure dependent $K^+ \to e^+\nu\gamma$ decay, which will be subtracted from the collected sample.

4.1 K^+ analysis

K^+ beam particles will be identified by the beam Cherenkov counter, and misidentification is not a problem because these events are easily rejected by other analyses. The K^+ decay vertex will be determined as intersection point of a K^+ track and an e^+ or μ^+ track in the scintillating fibers of the target. Although the DC separator in the K1.1BR line will be in operation, the beam will likely still contain about the same number of π^+. Therefore, it is essential to pick up the K^+ by using the K-ring PMT. The K^+/π^+ separation using the multiplicity cut of K-ring and π-ring PMTs will be quite satisfactory. Since K^+ produce a signal in the K-ring with high multiplicity and in the π^+-ring with low multiplicity, we can set the threshold to a certain value of the multiplicity for both the K-ring and π-ring PMTs in order to extract the K^+ particles.

In the case of in-flight K^+ decay, the momentum of e^+ and μ^+ is modified and a systematic bias would be introduced in the event reconstruction of K_{e2} and $K_{\mu2}$. The K^+ stopping condition in the target is checked by using the timing information of the beam Cherenkov counter. The timing of an incoming K^+ will be determined by the average time of the K-ring PMTs. The events due to K^+ decay in flight will occur promptly, while the events due to stopped K^+ are delayed following an exponential curve with the K^+ lifetime of 12.4 ns. Events earlier than a reasonable time will be rejected.

The K^+ decay vertex will be determined by checking the pattern of the K^+ track and secondary charged particle track in the scintillating fiber target. For the incoming K^+ beam, the energy deposit in one of the fibers is much larger than that for decay particles emitted radially from the target. Also, the timing of the incoming K^+ coincides with the beam Cherenkov counter, while that of the outgoing particle

is delayed. The K^+ track and the e^+/μ^+ track are recognized from the energy and timing information of each fiber, and the intersection point is treated as the K^+ decay vertex in the x-y plane.

4.2 e^+ and μ^+ momentum analysis

Charged particles from the target will be tracked using one GEM (C1) and three MWPCs (C2, C3, C4) as well as by the fiber target. It should be noted that the momentum analysis procedure is exactly identical for K_{e2} and $K_{\mu 2}$. The hit position of the trackers is calculated from the induced charges on the cathode strips. The passage of a charged particle induces a point-like charge avalanche at the same point on the anode wire, thus producing a charge distribution along several cathode strips. A difference of the detection efficiency between the e^+ and the μ^+ due to different energy deposits in the trackers would introduce a systematic error and we have to carefully treat this problem. This error can be controlled by measuring the chamber efficiencies directly, as described in Section 7.2.

The e^+ and μ^+ momentum is calculated by reconstructing a track under the calculated spectrometer field by the TOSCA code using a Runge-Kutta tracking method. The trajectory of the e^+ and the μ^+ can be determined uniquely by assigning the parameters of (1) hit position, (2) direction, (3) momentum at C1 for forward tracking or C4 for backward tracking. These parameters are determined by minimizing χ^2 which is defined as a sum of the squares of the distances between the fitted track and the data. Events with a large χ^2 value due to scattering or decay-in-flight are rejected. The e^+ and μ^+ momenta are required to be higher than the endpoints, 228 MeV/c and 215 MeV/c, of K_{e3} and $K_{\mu 3}$, respectively, to remove the K_{e3} and $K_{\mu 3}$ backgrounds.

4.3 γ analysis

For the measurement of the radiative $K^+ \to e^+\nu\gamma$ ($K_{e2\gamma}$) and $K^+ \to \mu^+\nu\gamma$ ($K_{\mu 2\gamma}$), the CsI(Tl) calorimeter will be used. The number of photon hits in the CsI(Tl) calorimeter is required to be one. The energy calibration of each module is carried out using charged particles from $K_{\pi 2}$, $K_{\mu 2}$, and π^0 from $K_{\pi 2}$. Relative gain coefficients are obtained from the μ^+ and π^+ signals of the single module hits. Since the response function of the CsI(Tl) calorimeter for photons should be different from that for charged particles, the absolute gain coefficients are determined to reproduce the π^0 energy spectrum of $K_{\pi 2}$. The photon energy is obtained by summing up the energy of a photon cluster and the hit position of the photon is calculated by an energy-weighted centroid of each module. The photon direction is determined from the K^+ decay vertex and the photon hit position in the calorimeter by connecting them with a straight line. Compared with the E246 experiment, the accidental rate due to the beam halo should be much lower because of the improvement of the K^+/π^+ ratio, as discussed in section 3.3.1, and therefore this effect is harmless.

According to the Monte Carlo simulation, $K^+ \to e^+\nu$ with a external bremsstrahlung photon is not detected by the calorimeter (see below). Also, most of the radiative IB photons pass though the muon hole, while a part of $K_{l2\gamma}$ events can be detected by the calorimeter. For the determination of R_K, the radiative corrected K_{e2}+$K^{IB}_{e2\gamma}$ and $K_{\mu 2} + K^{IB}_{\mu 2\gamma}$ events have to be analyzed. On the other hand, the SD events are backgrounds for the present experiment and have to be subtracted from the observed sample. For this purpose, the reproducibility of the observed IB and SD spectra by a Monte Carlo simulation is very important for the understanding of these physics processes.

4.4 Particle identification

Particle discrimination between the e^+ and μ^+ will be carried out by measuring the time-of-flight (TOF) between the TOF1 and TOF2 counters and by using the aerogel Cherenkov counter. The particle incoming time is determined by the average time of the two phototubes at both ends. A time-walk correction of the leading-edge discriminator will be applied to both TOF1 and TOF2. The TOF value will be calibrated using mono-energetic charged particles from $K_{\pi 2}$ and $K_{\mu 2}$, in which the real TOF value from the information of the flight path length and momentum can be calculated. Then, β and mass squared ($M^2_{\rm TOF}$) are obtained as,

$$\beta = \frac{L}{TOF \cdot c} \tag{21}$$

$$M^2_{\rm TOF} = p^2(1/\beta^2 - 1), \tag{22}$$

where L is the flight length, c is the speed of light, and p is the momentum of the charged particle. The timing resolution of $\sigma_T = 100$ ps provides a good separation between the K_{e2} and $K_{\mu 2}$ events (see Section 5.2).

The e/μ misidentification directly introduces a systematic error into the R_K determination. The detector efficiency for the both TOF and Cherenkov system can be directly measured by tagging events with the trackers. Details of the systematic effect due to this misidentification are discussed in Section 7.2.4.

4.5 K_{e2} and $K_{\mu 2}$ data sample

The selection requirements for K_{e2}, $K_{\mu 2}$, and their radiative decays can be simply summarized as,

- Charged particles are discriminated by the Cherenkov counter as well as the TOF measurement.
- Momenta of charged particles are higher than 228 MeV/c for positrons and 215 MeV/c for muons.
- The number of photon clusters detected by the CsI(Tl) calorimeter is 0 or 1.

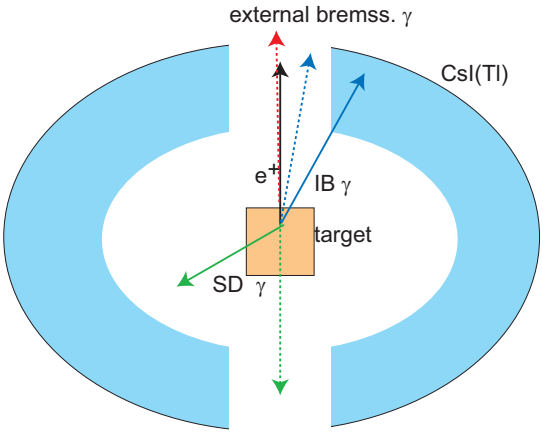

Figure 15: Schematic view of the photon detections. External bremsstrahlung photons are nearly parallel to the e^+ direction (black arrow). They pass through the holes without hitting the calorimeter (red dotted arrow) and contribute only to D0. Radiated photons generated through IB and SD contribute to both D0 (dotted blue and green arrow) and D1 (solid blue and green arrow).

Therefore, the collected data sample after applying the above analysis will be separated into four categories: no photon detection by the CsI(Tl) calorimeter (D0) for e^+ (D0e) and μ^+ (D0μ), and one photon detection (D1) for e^+ (D1e) and μ^+ (D1μ), as shown in Fig. 15 and Fig. 16. Hereafter, the R_K determination will be explained using these four event categories. Although events with two or more than two photon clusters are recorded in the data, they are rejected in the present analysis.

The D0e data consists of (a) K_{e2} without bremsstrahlung photon emission, (b) K_{e2} with bremsstrahlung photon emission and its escape (c) $K^{IB}_{e2\gamma}$ with a photon escape, and (d) $K^{SD}_{e2\gamma}$ with a photon escape. The D1e data are composed of (e) K_{e2} with bremsstrahlung photon emission and its detection, (f) $K^{IB}_{e2\gamma}$ with a photon detection, and (g) $K^{SD}_{e2\gamma}$ with a photon detection. Since we do not need to consider external bremsstrahlung photons for the muon sample, the muon data is simpler than the positron data. The D0μ data consist of (a) $K_{\mu 2}$, (b) $K^{IB}_{\mu 2\gamma}$ with a photon escape, and (c) $K^{SD}_{\mu 2\gamma}$ with a photon escape. The D1μ data are composed of (d) $K^{IB}_{\mu 2\gamma}$ with a photon detection and (e) $K^{SD}_{\mu 2\gamma}$ with a photon detection.

For the determination of R_K, we have to use the $\tilde{K}_{e2} = K_{e2} + K^{IB}_{e2\gamma}$ and $\tilde{K}_{\mu 2} = K_{\mu 2} + K^{IB}_{\mu 2\gamma}$ processes. Events due to the SD component have to be subtracted from the observed sample. Since we require the charged particle momentum to be higher than the K_{e3} and $K_{\mu 3}$ endpoints, background contaminations other than the $K^{SD}_{l2\gamma}$ component are negligible. Details of the R_K determination are explained using calculated events in a Monte Carlo simulation in Section 6.2.

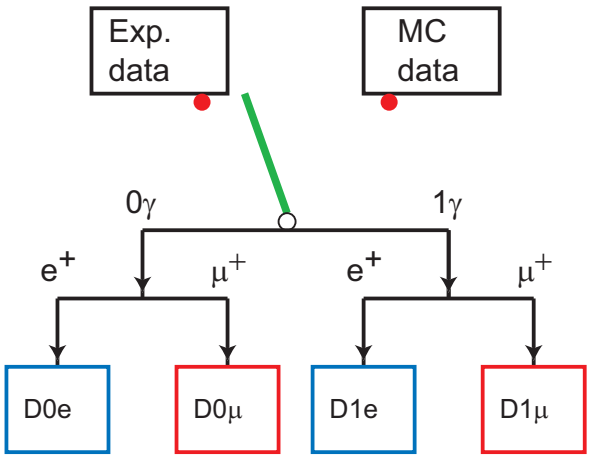

Figure 16: Flow chart for the data handling. The experimental and simulation data are analyzed by the same program codes. The accepted events after applying the analysis are separated into four categories: no photon detection (D0) for e^+ (D0e) and μ^+ (D0μ), and one photon detection (D1) for e^+ (D1e) and μ^+ (D1μ).

5 Monte Carlo simulation

The K_{e2}, $K^{IB}_{e2\gamma}$, $K^{SD}_{e2\gamma}$, $K_{\mu 2}$, $K^{IB}_{\mu 2\gamma}$, and $K^{SD}_{\mu 2\gamma}$ processes were carefully studied in a Monte Carlo simulation. Main purposes of this simulation study can be summarized as,

- The expected K_{l2} and $K_{l2\gamma}$ spectra in the D0 and D1 samples can be obtained (section 5.2). Expected spectra shapes and detector response functions are calculated by the simulation. Needless to say that knowledge of the detector response is essential to design the experiment. Since the $K_{l2\gamma}$ decays have an infrared divergence at $E_\gamma = 0$, an energy threshold for the γ measurement is important and the suitable threshold level is determined. The separation of IB and SD components for the $K_{l2\gamma}$ decays are also checked using the simulation data.

- The detector acceptances for K_{l2} and $K_{l2\gamma}$ are calculated (section 5.2). The ratio of the K_{e2} and $K_{\mu 2}$ acceptances is important for the R_K determination. These values are also used for the estimation of the statistical error of the proposed experiment.

- The performance of the particle identification between e^+ and μ^+ by the TOF measurement is checked (section 5.2). The e^+/μ^+ identification is one of the key issues in the proposed experiment. The TOF mass spectra are obtained as a function of the distance of TOF2 from C4 assuming a realistic time resolution of $\sigma_t = 100$ ps.

- The characteristics of the bremsstrahlung photon emitted from interactions between the e^+ and the target materials are carefully studied (section 5.2).

Bremsstrahlung creation probability, the energy of bremsstrahlung emitted in the target, and the opening angle between e^+ and bremsstrahlung are obtained. It is concluded that the direction of the external bremsstrahlung photons is nearly parallel to the e^+ direction and they pass through the holes without hitting the calorimeter.

- The SD component of the $K_{e2\gamma}$ decay contributes to the background and we have to subtract this background from the observed K_{e2} events. Although we will impose no γ hit in the CsI(Tl) calorimeter, the SD component of the $K_{e2\gamma}$ decay with photon escape through the holes of the calorimeter is contained in the 0γ sample. Details of the analysis procedure using the D0 and D1 samples are described in Section 6.1. The background fraction from the SD component in the $K_{e2\gamma}$ events is carefully estimated.

- A concrete method to determine the R_K value is described in Section 6.2. The treatment of the radiative correction for the IB process is one of the most important points. Details of the analysis procedure is explained using the simulation data.

- The statistical and systematic errors are estimated in Section 7. The statistical error is calculated by using the detector acceptance obtained in the simulation. Systematic errors from background contamination by the SD component of $K_{e2\gamma}$, the radiative correction, and K_{e2} acceptance loss due to high energy bremsstrahlung emission are estimated from the simulation.

The realistic geometry of the entire detector system and the magnetic field of the toroidal spectrometer were precisely implemented in the calculation. The simulation starts from K^+ decay in the target and follows the trajectories of all the daughter particles in the detector volume. In the simulation, various interactions for the charged particles and the photons were taken into account. In particular, multiple scattering, Bhabha scattering, and bremsstrahlung are very important for the proposed experiment. The simulation data are also separated into 4 categories: D0 (D0e, D0μ) and D1 (D1e, D1μ) which receive the same treatment as the experimental data.

The simulation program developed for the TREK experiment was based on the CERN library, GEANT3. By using this elaborated simulation code in E246 and E470, we have analyzed several decay modes such as, $K^+ \to \pi^0 e^+ \nu$, $K^+ \to \pi^0 \mu^+ \nu$, $K^+ \to \pi^0 e^+ \nu\gamma$, $K^+ \to \pi^0 \mu^+ \nu\gamma$, $K^+ \to \pi^+ \pi^0 \gamma$, and $K^+ \to \pi^0 \pi^0 e^+ \nu$ decays [43, 44, 45, 46, 47, 48]. Spectroscopic studies of these decay modes have been successfully performed. The simulation code has been constructed step-by-step by strict checks of these physics analyses. In this course, our simulation program has been carefully tested, and is thus very reliable. In this section, we would like also to discuss the feasibility of the R_K measurement itself using the TREK apparatus based on the simulation.

5.1 Theoretical form of the $K^+ \to l^+\nu\gamma$ decay

The following theoretical calculation was used as input in the simulation calculation [49, 50]. The differential decay rate in the K^+ rest frame can be written in terms of $x \equiv \frac{2E_\gamma}{M_K}$ and $y \equiv \frac{2(E_l+M_l)}{M_K}$, where E_γ is the photon energy, E_l is the lepton kinetic energy, M_l is the lepton mass, and M_K is the K^+ mass:

$$\begin{aligned}\frac{d\Gamma_{K_{\mu\nu\gamma}}}{dxdy} &= A_{IB}f_{IB}(x,y) \\ &+ A_{SD}[(F_V+F_A)^2 f_{SD^+}(x,y) + (F_V-F_A)^2 f_{SD^-}(x,y)] \\ &- A_{INT}[(F_V+F_A) f_{INT^+}(x,y) + (F_V-F_A) f_{INT^-}(x,y)], \end{aligned} \tag{23}$$

where

$$\begin{aligned} f_{IB}(x,y) &= \left[\frac{1-y+r}{x^2(x+y-1-r)}\right] \\ &\quad \times\left[x^2 + 2(1-x)(1-r) - \frac{2xr(1-r)}{x+y-1-r}\right], \end{aligned} \tag{24}$$

$$f_{SD^+} = [x+y-1-r][(x+y-1)(1-x)-r], \tag{25}$$

$$f_{SD^-} = [1-y+r][(1-x)(1-y)+r], \tag{26}$$

$$f_{INT^+} = \left[\frac{1-y+r}{x(x+y-1-r)}\right][(1-x)(1-x-y)+r], \tag{27}$$

$$f_{INT^-} = \left[\frac{1-y+r}{x(x+y-1-r)}\right][x^2-(1-x)(1-x-y)-r], \tag{28}$$

$$r = \left[\frac{M_l}{M_K}\right]^2, \tag{29}$$

$$A_{IB} = \Gamma(K_{l2})\frac{\alpha}{2\pi}\frac{1}{(1-r)^2}, \tag{30}$$

$$A_{SD} = \Gamma(K_{l2})\frac{\alpha}{8\pi}\frac{1}{r(1-r)^2}\left[\frac{M_K}{F_K}\right]^2, \tag{31}$$

$$A_{INT} = \Gamma(K_{l2})\frac{\alpha}{2\pi}\frac{1}{(1-r)^2}\frac{M_K}{F_K}. \tag{32}$$

In these formulas, F_V is the vector form factor, F_A is the axial form factor, α is the fine structure constant (1/137.036), F_K is the K^+ decay constant ($159.8 \pm 1.4 \pm 0.4$ MeV), and $\Gamma(K_{l2})$ is the width of the K_{l2} decay. As seen from Eq. (24), the differential spectrum of internal bremsstrahlung f_{IB} has the infra-red divergence nature, which has to be taken into account in the analysis

The SD^+ and SD^- refer to the different photon polarizations, and these components do not mutually interfere. Both SD^+ and SD^- can interfere with IB, however, resulting in the terms labeled INT^+ and INT^-. The SD^+ component peaks at high muon and photon energy, making it the easiest of the SD components to observe.

The SD^- and INT^- terms are negligible in the present study. Hereafter, the SD^+ term is described to be just SD. The form factors of the decay, F_V and F_A, can, in principle, depend on q^2, which is given by $q^2 = M_K^2 - 2M_K E_\gamma$ in the K^+ rest frame. In an $\mathcal{O}(p^4)$ ChPT calculation, however, they are found to be q^2 independent and are given by $F_V + F_A = 0.137$, and $F_V - F_A = 0.052$. In the data analysis, we initially assume that they are constant, then test for q^2 dependence.

5.2 K_{l2} and $K_{l2\gamma}$ spectra in the D0 sample

The Monte Carlo simulation to study the response function of the detector system to the K_{e2} decay was carried out for both the e^+ measurement by the spectrometer and the γ measurement by the CsI(Tl) calorimeter. Fig. 17 shows (a) the e^+ momentum, (b) bremsstrahlung creation probability as a function of flight path length in the target, (c) the energy of bremsstrahlung emitted in the target, (d) the opening angle between the e^+ and the bremsstrahlung photon. Here it should be emphasized that external bremsstrahlung gammas are nearly parallel to the e^+ direction and they pass through the holes without hitting the calorimeter, as shown in Fig. 17(d). Since the μ^+ does not generate a bremsstrahlung photon, only the $K_{\mu 2}$ momentum distribution is shown in Fig. 18. The K_{e2} and $K_{\mu 2}$ events accepted by the spectrometer can be categorized as the D0 data. Also, the $M^2_{\rm TOF}$ spectrum obtained as a function of the distance of TOF2 from C4 by assuming $\sigma_t = 100$ ps is shown in Fig. 19, indicating good separation for the K_{e2} and $K_{\mu 2}$ events. In the figure, the K_{e2} and $K_{\mu 2}$ branching ratios are taken into account. The dependence of the detector acceptance and the mass resolution on the TOF2 position is also shown in Fig. 19.

In order to understand the characteristics of these bremsstrahlung photons, the emission probability was measured using the E470 data. Details are described in Appendix A. The E470 experiment [5] was performed with a magnetic field of the spectrometer at B = 0.65 T. The behavior of the GP counters was studied when obvious K_{e3} events were tagged by the detector system. The K_{e3} events were selected using the two-photon cluster data with the conditions: $-5000 < M^2_{\rm TOF} < 5000$ MeV$^2/c^4$ and $\theta_{e^+\pi^0} < 166^\circ$, where $\theta_{e^+\pi^0}$ is the opening angle between the e^+ and the π^0. The distribution of the numbers of the hit GP counter determing the magnet sector through which the e^+ passed is shown in Fig. 20, together with the Monte Carlo simulation. The counting rates other than from the gap through which the e^+ passed, is at the 10^{-3} level. The direction of the external bremsstrahlung photons is thus nearly parallel to the e^+ direction and they pass through the holes without hitting the calorimeter.

In general, since the decay particles are essentially affected by the interaction with the target material in the stopped K^+ experiment, the K_{e2} event with a bremsstrahlung photon generated through the interaction between the e^+ and the stopper material would deform the K_{e2} spectra. Fortunately, events of K_{e2} with an external

[5] In the E470 experiment which was performed subsequent to E246, spectroscopic studies of various K^+ decay channels were carried out using the E246 detector system at KEK-PS.

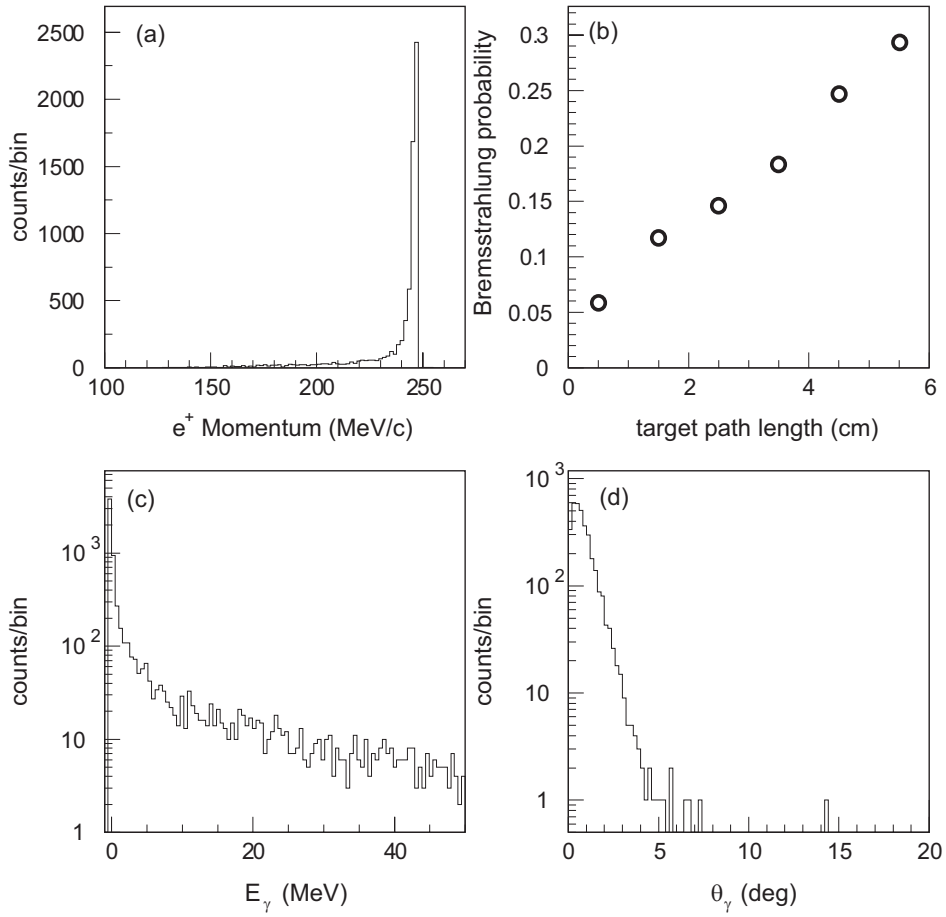

Figure 17: K_{e2} spectra stored in the simulated D0 sample: (a) e^+ momentum, (b) bremsstrahlung creation probability as a function flight path length in the target, (c) energy of bremsstrahlung emitted in the target, (d) opening angle between e^+ and bremsstrahlung photon.

bremsstrahlung photon contribute only to the D0 sample because they do not hit the calorimeter. Therefore, the number of radiative corrected $K_{l2} + K^{IB}_{l2\gamma}$ events is determined from the D0 data by correcting for the $K^{IB}_{l2\gamma}$ fraction and subtracting the $K^{SD}_{l2\gamma}$ contribution.

The Monte Carlo simulations for the $K^{IB}_{e2\gamma}$ and $K^{IB}_{\mu 2\gamma}$ events were also carried out. The theoretical form of Eq. (23) was used for inputs into the calculation. To remove the infrared divergence at $E_\gamma = 0$, an E_γ threshold of $E_\gamma >$7.5 MeV was assumed in the simulation. Fig. 21 shows the $K^{IB}_{e2\gamma}$ and $K^{IB}_{\mu 2\gamma}$ spectra with a radiated photon escape through the holes, which should be categorized to be the D0 sample. The detector response to events of the SD component stored in the D0 data is described in Section 6.1.

The detector acceptances of $\Omega(K_{l2})$ and $\Omega(K_{l2\gamma})$ for the D0 sample were obtained

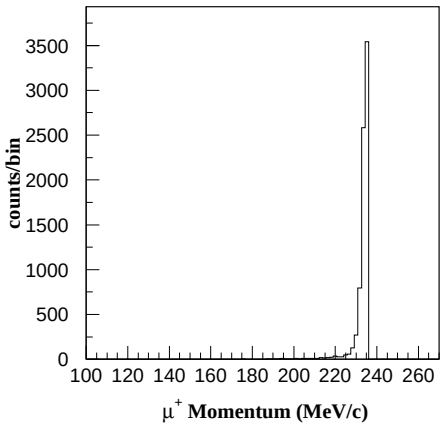

Figure 18: The $K_{\mu 2}$ momentum distribution stored in the simulated D0 sample. Since the μ^+ does not generate a bremsstrahlung photon, only the momentum distribution is shown.

from the simulation as,

$$\Omega = n_{accept}/n_{trigger}, \tag{33}$$

where n_{accept} is the accepted number of events after requiring the event selection conditions and $n_{trigger}$ is the generated K^+ number. They were determined to be $\Omega(K_{e2}) = 6.99 \times 10^{-2}$ and $\Omega(K_{e2}) = 7.74 \times 10^{-2}$.

5.3 K_{l2} and $K_{l2\gamma}$ spectra in D1 sample

The key to success in the R_K determination using the TREK apparatus is the understanding of the following 3 processes: (1) K_{e2} with external bremsstrahlung generated in the stopper, (2) $K_{e2\gamma}$ internal bremsstrahlung (IB), and (3) the $K_{e2\gamma}$ structure dependent term (SD), because the width of the radiative corrected $K_{l2} + K_{l2\gamma}^{IB}$ has to be compared with the theoretical calculation.

The Monte Carlo simulation for the D1 sample was carried out in order to check the separation of the IB and SD processes. Fig. 22 and 23 show the $K_{e2\gamma}$ and $K_{\mu 2\gamma}$ spectra, respectively, obtained by requiring that the radiated photon is detected by the calorimeter for the IB (red) and SD (black) processes. In the figure, (a) the e^+ momentum, (b) the $\theta_{e^+\gamma}$ distribution, (c) the E_γ spectrum and (d) the correlation plot for E_γ and $\theta_{e^+\gamma}$ are shown for SD (black) and IB (red), where E_γ is the photon energy and $\theta_{e^+\gamma}$ is the opening angle between the e^+ and the photon. Needless to say, these events are categorized as the D1 data. Since IB has a peak structure at $E_\gamma = 0$ due to the infrared divergence, the energy threshold for the photon measurement has

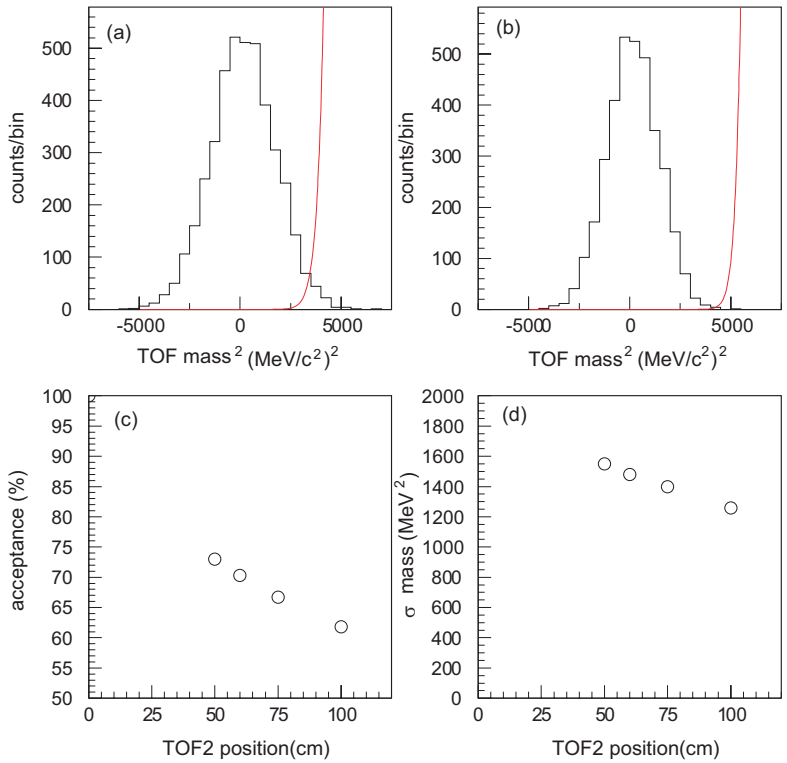

Figure 19: $M^2_{\rm TOF}$ spectra for K_{e2} and $K_{\mu 2}$ events obtained in the TOF analysis by assuming $\sigma_t = 100$ ps. The TOF2 position is (a) just behind C4 and (b) 1 m from C4. The detector acceptance (c) and mass resolution (d) are calculated under the assumption of $\sigma_t = 100$ ps as a function of the TOF2 position, where 0 corresponds to the TOF2 counter position being just behind C4.

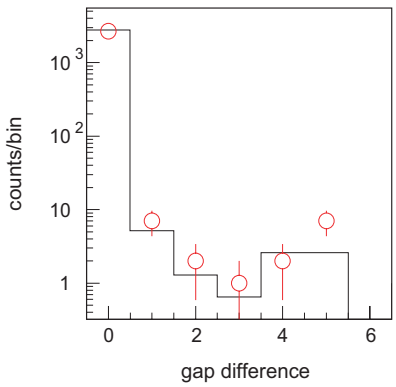

Figure 20: The distribution of the hit GP counter position as determined from the magnet sector through which the e^+ passed. The dots are the experimental data from the E470 experiment and the histogram is the simulation. The counting rates other than from the gap through which the e^+ passed is at the 10^{-3} level.

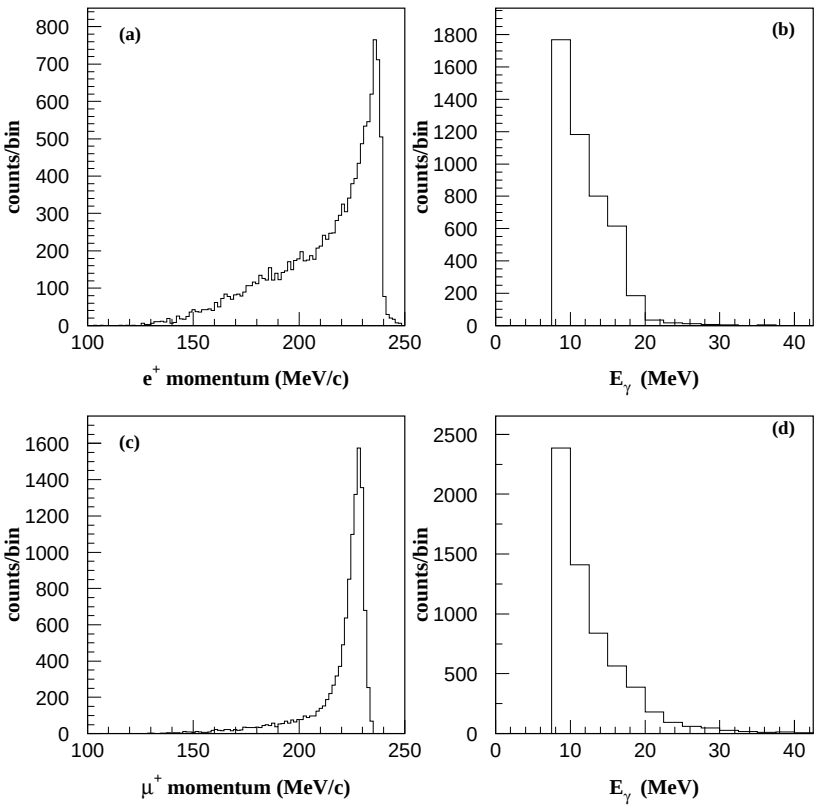

Figure 21: The simulated $K^{IB}_{e2\gamma}$ and $K^{IB}_{\mu 2\gamma}$ events categorized as D0e and D0μ are shown in (a)(b) and (c)(d), respectively. (a)(c) are the charged particle momentum distributions and (b)(d) are the photon energy distribution. Photons are escaping through the holes without hitting a CsI(Tl).

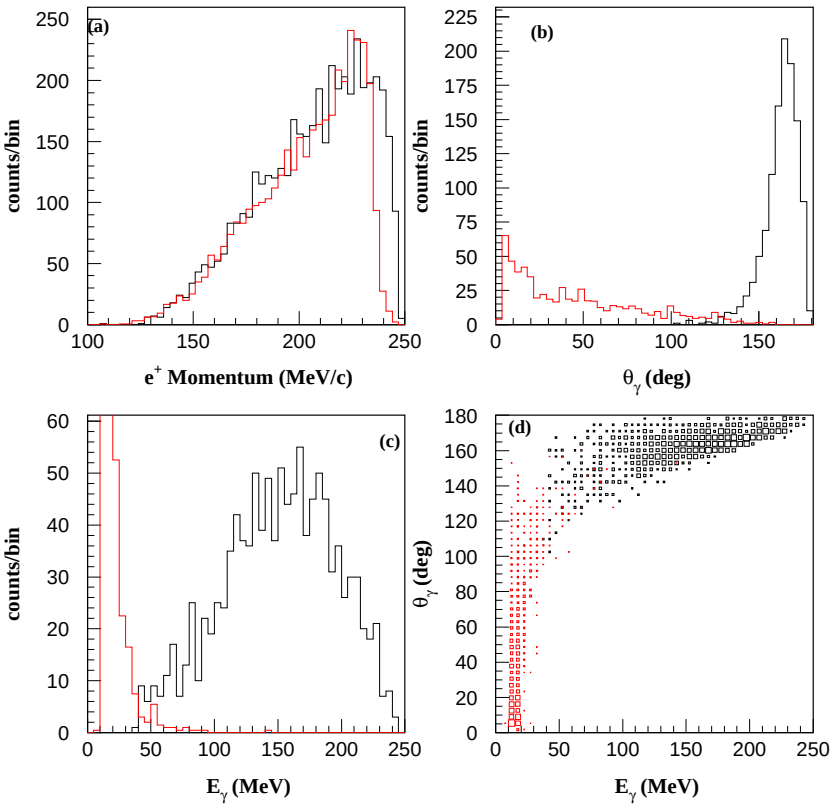

Figure 22: $K^{IB}_{e2\gamma}$ (red) and $K^{SD}_{e2\gamma}$ (black) spectra stored in the simulated D1 sample: (a) the e^+ momentum, (b) the $\theta_{e^+\gamma}$ distribution, (c) the E_γ spectrum and (d) the correlation plot for E_γ and $\theta_{e^+\gamma}$, for SD (black) and IB (red). The events due to the IB and SD processes have a distinct structure and it is possible to separate them.

to be reduced as low as possible to increase the acceptance for the IB processes. In this calculation, $E_\gamma > 20$ MeV as used in the E246 experiment, was assumed. As can be easily understood from the figure, the spectral shapes are quite distinct and it can be concluded that a separation of the IB and SD processes is quite feasible. The acceptances of the radiative $K^{IB}_{e2\gamma}$ and $K^{IB}_{\mu 2\gamma}$ decays with a photon detected were determined to be 5.3×10^{-4} and 6.5×10^{-3}, respectively. The K_{e2} decay with a bremsstrahlung photon does not contribute to the D1 sample.

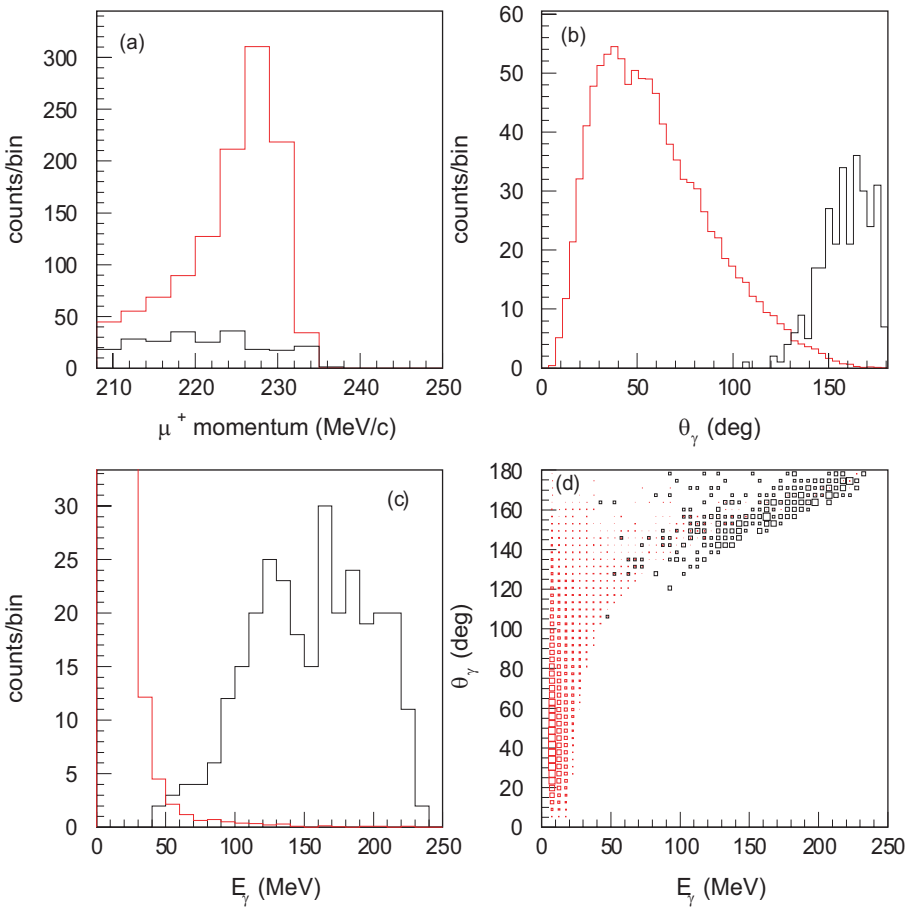

Figure 23: $K^{IB}_{\mu 2\gamma}$ (red) and $K^{SD}_{\mu 2\gamma}$ (black) spectra stored in the simulated D1 sample: (a) the μ^+ momentum, (b) the $\theta_{\mu^+\gamma}$ distribution, (c) the E_γ spectrum and (d) the correlation plot for E_γ and $\theta_{\mu^+\gamma}$, for SD (black) and IB (red). The events due to the IB and SD processes have a distinct structure and it is possible to separate them.

Table 10: Detector acceptances for K_{l2} and $K_{l2\gamma}$. They are given by separating events into the D0 and D1 samples. Details of the error evaluation will be done by comparing the experimental data with the simulation.

Decay mode	Ω for D0	Ω for D1
K_{e2}	6.99×10^{-2}	0
K^{IB}_{e2}	2.43×10^{-2}	5.30×10^{-4}
K^{SD}_{e2}	5.13×10^{-3}	1.13×10^{-2}
$K_{\mu 2}$	7.74×10^{-2}	0
$K^{IB}_{\mu 2}$	1.60×10^{-3}	6.53×10^{-3}
$K^{SD}_{\mu 2}$	9.43×10^{-4}	3.08×10^{-3}

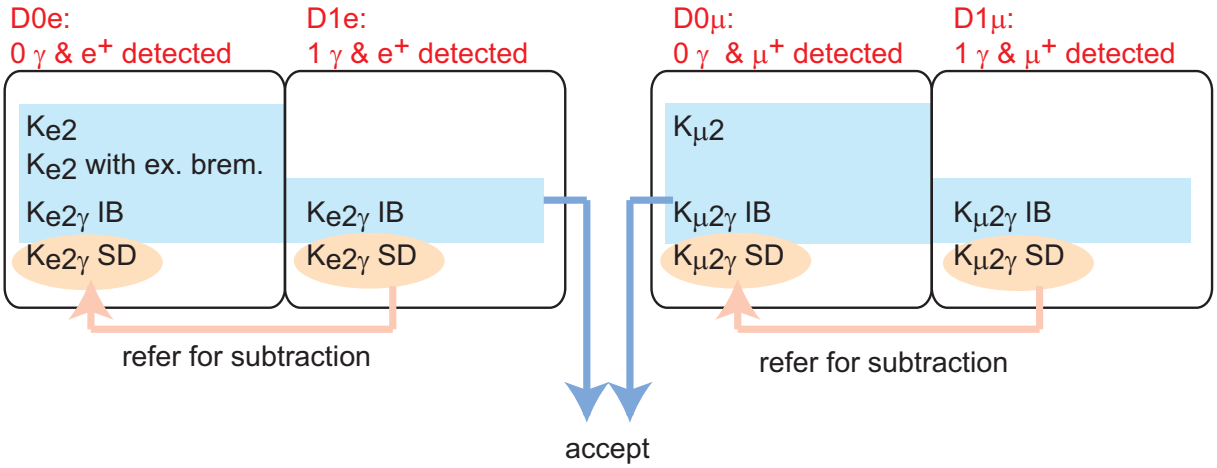

Figure 24: The schematic explanation of data handling for each decay. Since we can understand the $K^{SD}_{l2\gamma}$ kinematics carefully using the D1 data, we can correctly estimate this background fraction in D0 sample. The $K^{IB}_{l2\gamma}$ events have to be included into the K_{l2} events for the radiative correction.

6 Determination of the $\Gamma(K^+ \to e^+\nu)/\Gamma(K^+ \to \mu^+\nu)$ ratio

The R_K value is determined from the numbers of the detected $K_{e2}(\gamma)$ and $K_{\mu 2}(\gamma)$ events by correcting for the detector acceptances obtained from a MC simulation. Here, we will explain some details of the R_K determination. The schematic explanation of the data handling for each decay is shown in Fig. 24.

6.1 Backgrounds from SD component of $K_{e2\gamma}$ decay

The study of backgrounds from the SD component of the $K_{e2\gamma}$ decay starts from a correct understanding of the SD spectra using the D1e data. As mentioned in Section 3.3.8, events due to the SD component are recorded in the data with nearly the same statistics of the K_{e2} events and a spectroscopic study is possible by employing a similar procedure from the E246/470 analyses. These $K^{SD}_{e2\gamma}$ spectra obtained by the simulation are shown in Fig. 25 as indicated by black histograms. The shapes of the spectra and the branching ratio can be compared with the results reported by the KLOE group [29].

Next, we will switch from the analysis of $D1e$ events to alternative $D0e$ events. Although we will impose no γ hit in the CsI(Tl) calorimeter, the SD component of the $K_{e2\gamma}$ decay with the photon escaping through the holes of the calorimeter is contained in the 0γ sample. The radiated photon produced through the SD process tends to be emitted in the opposite direction of the e^+ and a part of the photons escape without hitting the calorimeter, as shown in Fig. 25, indicated by the red histograms. Since

we can study and understand the $K^{SD}_{e2\gamma}$ kinematics carefully using the D1e data, we can correctly estimate this background fraction. The relative number of these events is estimated to be

$$\frac{N(K^{SD}_{e2},0\gamma)}{N(K_{e2})} = \frac{BR(K^{SD}_{e2})}{BR(K_{e2})}\cdot\frac{\Omega(K^{SD}_{e2},0\gamma)}{\Omega(K_{e2})} \tag{34}$$

$$= \frac{1.52\times10^{-5}}{1.55\times10^{-5}}\cdot\frac{0.513\times10^{-2}}{6.99\times10^{-2}} = 0.072, \tag{35}$$

which should be subtracted for the further analysis of the R_K determination, as shown in Fig. 24. Note that the information of the GP counter will improve the understanding of the SD backgrounds. On the other hand, the SD component in $K_{\mu2\gamma}$ does not contribute to the $K_{\mu2}$ analysis because its fraction in the D0μ data is negligibly small.

6.2 Determination of the R_K value using the D0 sample

We would like to describe a concrete method to deduce the R_K value from the observed D0 data. The treatment of the radiative correction for the IB process is one of the most important points in the present analysis, as shown in Fig. 24. Here, the theoretical model is assumed to exactly determine the IB component of $K_{l2\gamma}$ from K_{l2}. Under this assumption, the IB branching ratio can be written as

$$BR(K^{IB}_{e2\gamma}) = \alpha BR(K_{e2}) \tag{36a}$$

$$BR(K^{IB}_{\mu2\gamma}) = \beta BR(K_{\mu2}), \tag{36b}$$

where α and β are the radiative correction factors which are calculable numbers in the framework of the above theoretical calculation. Also, the corresponding detector acceptance is expressed using a correction factor (f) as,

$$\Omega(K^{IB}_{e2\gamma}) = f(\alpha)\Omega(K_{e2}), \tag{37a}$$

$$\Omega(K^{IB}_{\mu2}) = f(\beta)\Omega(K_{\mu2}). \tag{37b}$$

Then, the numbers of accepted events after subtracting the K^{SD}_{e2} component are described to be

$$N(K_{e2}) = N_K BR(K_{e2})\Omega(K_{e2}), \tag{38a}$$

$$N(K^{IB}_{e2\gamma}) = N_K BR(K^{IB}_{e2\gamma})\Omega(K^{IB}_{e2\gamma}) \tag{38b}$$

$$= N_K \alpha BR(K_{e2}) f(\alpha)\Omega(K_{e2}), \tag{38c}$$

and

$$N(K_{\mu2}) = N_K BR(K_{\mu2})\Omega(K_{\mu2}), \tag{39a}$$

$$N(K^{IB}_{\mu2\gamma}) = N_K BR(K^{IB}_{\mu2\gamma})\Omega(K^{IB}_{\mu2\gamma}) \tag{39b}$$

$$= N_K \beta BR(K_{\mu2}) f(\beta)\Omega(K_{\mu2}), \tag{39c}$$

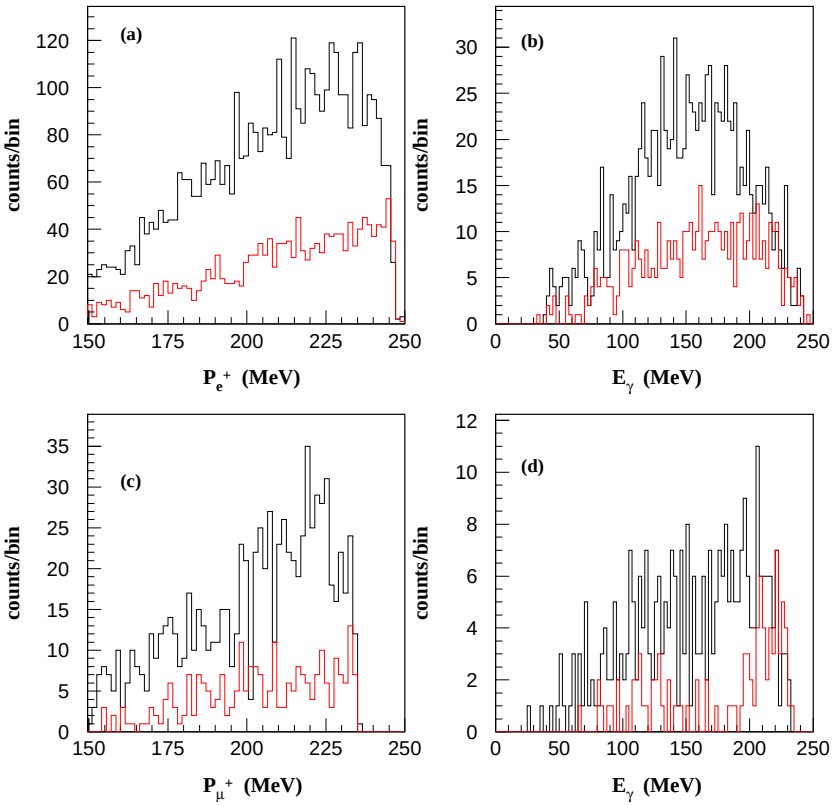

Figure 25: Spectra of the calculated SD component of the radiative $K_{e2\gamma}$ and $K_{\mu2\gamma}$ decays based on the D1 events (black histograms) and the D0 events (red histograms) by the CsI(Tl) calorimeter. (a)(c) and (b)(d) are the momentum distribution of the charged particle and the photon energy, respectively. (a)(b) are the $K_{e2\gamma}$ events and (c)(d) are the $K_{\mu2\gamma}$ events.

where N_K is the number of stopped K^+ in the stopper. $N(e^+) = N(K_{e2}) + N(K^{IB}_{e2\gamma})$ and $N(\mu^+) = N(K_{\mu 2}) + N(K^{IB}_{\mu 2\gamma})$ are the experimentally observed quantities in the D0 sample, and by forming the ratio of $N(e^+)$ to $N(\mu^+)$, the relationship of

$$\begin{aligned}
\frac{N(e^+)}{N(\mu^+)} &= \frac{BR(K_{e2})\Omega(K_{e2}) + BR(K^{IB}_{e2\gamma})\Omega(K^{IB}_{e2\gamma})}{BR(K_{\mu 2})\Omega(K_{\mu 2}) + BR(K^{IB}_{\mu 2\gamma})\Omega(K^{IB}_{\mu 2\gamma})} && \text{(40a)} \\
&= \frac{BR(K_{e2})\Omega(K_{e2}) + \alpha BR(K_{e2})f(\alpha)\Omega(K_{e2})}{BR(K_{\mu 2})\Omega(K_{\mu 2}) + \beta BR(K_{\mu 2})f(\beta)\Omega(K_{\mu 2})} && \text{(40b)} \\
&= \frac{BR(K_{e2})}{BR(K_{\mu 2})} \cdot \frac{\Omega(K_{e2})}{\Omega(K_{\mu 2})} \cdot \frac{1+\alpha f(\alpha)}{1+\beta f(\beta)} && \text{(40c)}
\end{aligned}$$

can be obtained. Since the $\Omega(K_{e2})/\Omega(K_{\mu 2}) \cdot [1+\alpha f(\alpha)]/[1+\beta f(\beta)]$ factor is calculable using the above theoretical model and the simulation calculation, the $BR(K_{e2})/BR(K_{\mu 2})$ value can be deduced using the above formula. Finally, the radiative corrected quantity

$$R_K = \frac{\Gamma(K_{e2}) + \Gamma(K^{IB}_{e2\gamma})}{\Gamma(K_{\mu 2}) + \Gamma(K^{IB}_{\mu 2\gamma})} = \frac{\Gamma(K_{e2}) + \alpha\Gamma(K_{e2})}{\Gamma(K_{\mu 2}) + \beta\Gamma(K_{\mu 2})} = \frac{\Gamma(K_{e2})}{\Gamma(K_{\mu 2})} \cdot \frac{1+\alpha}{1+\beta}. \qquad (41)$$

will be compared with the SM prediction in order to check the lepton universality.

6.3 Internal consistency check for radiative correction

According to the PDG, the IB component of the $K_{e2\gamma}$ decay has not yet been observed. On the other hand, the SD component has been precisely studied by the KLOE group [29]. In the proposed experiment, we would like to attempt the first observation of the IB process and check the theoretical calculation by comparing with the experimental results.

After the extraction of the IB events from the D1 sample, an internal consistency check for the radiative correction will be performed by comparing with the D0 and D1 data. The number of observed events are described to be

$$\begin{aligned}
N(K_{e2}, 0\gamma) &= N_K BR(K_{e2})\Omega(K_{e2}) && \text{(42a)} \\
N(K^{IB}_{e2\gamma}, 0\gamma) &= N_K BR(K^{IB}_{e2})\Omega(K^{IB}_{e2\gamma}, 0\gamma) && \text{(42b)} \\
&= N_K \alpha BR(K_{e2})\Omega(K^{IB}_{e2\gamma}, 0\gamma) && \text{(42c)}
\end{aligned}$$

for D0 events, and

$$\begin{aligned}
N(K_{e2}, 1\gamma) &\sim 0 && \text{(43a)} \\
N(K^{IB}_{e2\gamma}, 1\gamma) &= N_K BR(K^{IB}_{e2})\Omega(K^{IB}_{e2\gamma}, 1\gamma) && \text{(43b)} \\
&= N_K \alpha BR(K_{e2})\Omega(K^{IB}_{e2\gamma}, 1\gamma) && \text{(43c)}
\end{aligned}$$

for the D1 sample. Experimentally, the observable quantities are $N(0\gamma) = N(K_{e2}, 0\gamma) + N(K^{IB}_{e2\gamma}, 0\gamma)$ and $N(1\gamma) = N(K_{e2}, 1\gamma) + N(K^{IB}_{e2\gamma}, 1\gamma)$ for D0 and D1, respectively. By

taking the ratio of $N(0\gamma)$ to $N(1\gamma)$, the relation

$$\frac{N(0\gamma)}{N(1\gamma)} = \frac{BR(K_{e2})\Omega(K_{e2}) + \alpha BR(K_{e2})\Omega(K_{e2}^{IB}, 0\gamma)}{\alpha BR(K_{e2})\Omega(K_{e2}^{IB}, 1\gamma)} \quad (44a)$$

$$= \frac{1 + \alpha f(\alpha)}{\alpha g(\alpha)} \quad (44b)$$

is obtained, where g is the acceptance correction fraction defined as $\Omega(K_{e2}^{IB}, 1\gamma) = g(\alpha)\Omega(K_{e2})$. The right side of Eq. (44b) is calculable from the theoretical model and the Monte Carlo simulation. Therefore, using the above formula, we can perform an internal consistency check for radiative corrections and evaluate the correctness of the theoretical model adopted in this analysis. Needless to say, we can apply the same procedure for the $K_{\mu 2}$ and $K_{\mu 2\gamma}$ decays.

6.4 Measurement of external bremsstrahlung photons

The treatment of external bremsstrahlung photon in the Monte Carlo simulation is very important because some of the e^+ will lose their momentum by emitting a high-energy bremsstrahlung photon and will not be accepted in the analysis. Therefore, the main systematic error comes from the uncertainty of the K_{e2} fraction below the K_{e3} endpoint. In order to understand the characteristics of these processes, in particular the bremsstrahlung generation probability (ϵ_r) as a function of flight path length in the target, the behavior of the GP counters is studied when the e^+ are tagged by the spectrometer and compared with the simulation. The number of events with a bremsstrahlung hit in the GP counter can be described as,

$$N(GP) = N(e^+)\epsilon_r\Omega(GP) \quad (45)$$

where $N(e^+)$ and $N(GP)$ are the numbers of accepted e^+ events by the spectrometer and bremsstrahlung hits in the GP counter among them. $\Omega(GP)$ is the GP detector acceptance. The reproducibility of the experimental results by the Monte Carlo simulation will be carefully checked.

6.5 Byproduct physics

For the R_K determination, we need to analyze the $K^+ \to e^+\nu\gamma$ and $K^+ \to \mu^+\nu\gamma$ decays, as described above. Spectroscopic studies of semi-leptonic radiative decays offer a good testing ground of hadron structure models making use of low-energy effective Lagrangians as follows.

6.5.1 The $K^+ \to e^+\nu\gamma$ decay

Details of the theoretical form of the $K_{e2\gamma}$ decay is described in Section 5.1. The IB component of the $K_{e2\gamma}$ decay has not been observed yet and we intend to derive find it for the first time, although IB physics is theoretically well understood. The SD

form factors of the $K^+ \to e^+\nu\gamma$ transition have been studied in the light-front quark model and the chiral perturbation theory of $O(p^6)$. Due to the helicity suppression of the K_{e2} decay, the SD component gives the dominant contribution to their spectra shapes. Therefore, the precise measurement of $K_{e2\gamma}$ will offer a good testing ground for these theories [51].

6.5.2 The $K^+ \to \mu^+\nu\gamma$ decay

The decay $K^+ \to \mu^+\nu\gamma$ ($K_{\mu 2\gamma}$) can proceed via two distinct mechanisms. The first is the internal bremsstrahlung (IB) process which is a radiative version of the familiar $K_{\mu 2}$ decay. Its Feynman diagram has a photon emitted from the external kaon or muon line. The second is the structure-dependent radiative decay (SD), which involves the emission of a photon from intermediate states. The structure-dependent component in the decay $K_{\mu 2\gamma}$ was observed by the BNL E787 group [52]. Using the kinematic region where the muon kinetic energy is greater than 137 MeV and the photon energy is greater than 90 MeV, the sum of the vector and axial-vector form factors was extracted. In the current proposal, the accuracy of these form factors will be improved significantly.

7 Estimation of experimental sensitivity for the R_K determination

7.1 Statistical error

The statistical error of the R_K value will be subject to that of the accepted K_{e2} events because of the $BR(K_{\mu 2})/BR(K_{e2}) \sim 10^5$. We will assume 30 kW operation of the MR (low-intensity period) which corresponds to 220 kHz of kaon beam intensity (I_K) at the K^+ target position. Then, using the following parameters,

- 50 days of data collection, corresponding to 1500 kW·day or 1×10^{12} K^+
- The kaon stopping efficiency in the target (f) is 0.25
- The detector acceptance is $\Omega(K_{e2})$=0.07,

the number of K_{e2} events is estimated to be

$$\begin{aligned} N(K_{e2}) &= I_K \times (50 \cdot 3600 \cdot 24) \times f \cdot \Omega \cdot BR(K_{e2}) && \text{(46a)} \\ &= 220 \times 10^3 \times (50 \cdot 3600 \cdot 24) \times 0.25 \times 0.07 \times (1.55 \times 10^{-5}) && \text{(46b)} \\ &\sim 250 \times 10^3 && \text{(46c)} \end{aligned}$$

corresponding to a statistical error of $\Delta R_K = 0.0054$ ($\Delta R_K/R_K$=0.2%). The statistical errors reported by the NA62 and KLOE groups are 0.5% and 1.0%, respectively.

Table 11: Event reduction factors by each experimental requirement. We assume 30 kW operation of the MR and 50 days of data collection, corresponding to 1500 kW·day or 1×10^{12} K^+.

Item	Parameter	Statistics
Beam	1500 kW day (30 kW·50 days)	1×10^{12}
Kaon stopping effi.	0.25	3×10^{11}
Branching ratio of K_{e2}	1.55×10^{-5}	4×10^{6}
Detector acceptance	0.07	3×10^{5}

7.2 Systematic error

7.2.1 Reduction mechanism of systematic error

The R_K value can be determined using the form of

$$R_K = N(\tilde{K}_{e2})/N(\tilde{K}_{\mu 2}) \cdot \Omega(\tilde{K}_{\mu 2})/\Omega(\tilde{K}_{e2}), \quad (47a)$$

$$= N(\tilde{K}_{e2})/N(\tilde{K}_{\mu 2}) \cdot N(\tilde{K}_{\mu 2})^{\mathrm{MC}}/N(\tilde{K}_{e2})^{\mathrm{MC}}, \quad (47b)$$

where $N(\tilde{K}_{\mu 2})^{\mathrm{MC}}$ and $N(\tilde{K}_{e2})^{\mathrm{MC}}$ are the numbers of accepted events in the simulation with the same number of K^+ triggers for $\tilde{K}_{e2}$ and $\tilde{K}_{\mu 2}$, respectively. As indicated by this form, the general methodology for the reduction of error in the proposed experiment can be summarized as follows.

- **The simultaneous K_{e2} and $K_{\mu 2}$ measurements using a stopped K^+ beam.**
  The ambiguity of the number of stopped kaons will not contribute to the systematic error at all, since the K_{e2} and $K_{\mu 2}$ events are collected simultaneously. The detector inefficiencies are also canceled.

- **Detector apparatus.**
  The acceptance distortion associated with a misalignment of the detectors can be eliminated due to the rotational symmetry of the toroidal spectrometer. The distortion can be minimized by integrating over all e^+ and μ^+ directions.

- **Cancellation mechanism between K_{e2} and $K_{\mu 2}$.**
  Since we form the ratio of the calculated acceptance of K_{e2} and $K_{\mu 2}$ decay, the similarity of the K_{e2} and $K_{\mu 2}$ kinematics can reduce a systematic error due to the imperfect reproducibility of the experimental condition in the simulation, for example, field strength of the spectrometer, beam backgrounds, etc.

- **Analysis procedure.**
  The error arising from analysis can be reduced by treating the experimental data and the simulation data with the same procedure. For example, charged particle tracking, particle identification by TOF, etc. are common.

7.2.2 Background contamination

The D0 sample contains $K^{SD}_{e2\gamma}$ events with a photon escaping from the holes, and therefore the uncertainty of this background estimation introduces a systematic error. On the other hand, the SD component of the $K_{e2\gamma}$ decay is also recorded in the D1 sample with significant statistics. The correct understanding of the SD spectra by the simulation calculation makes the $K^{SD}_{e2\gamma}$ background uncertainty negligibly small compared to the statistical error. The background fraction is estimated from the simulation to be 7.2% of the accepted K_{e2} events. The information of the GP counter should improve the understanding of the SD background. The spectral shapes and the branching ratio will be compared with the results reported by the KLOE group. Therefore, the $K^{SD}_{e2\gamma}$ fraction will be estimated with an accuracy of $\sim 1\%$, resulting that the systematic error due to the $K^{SD}_{e2\gamma}$ backgrounds is estimated to be $< 0.1\%$. The SD component in $K_{\mu 2\gamma}$ does not significantly contribute to the error because its fraction is negligibly small.

7.2.3 Inefficiency of tracking elements

An efficiency difference of the GEM and MWPCs between e^+ and μ^+ would clearly introduce a systematic uncertainty in the R_K measurement. In order to remove this systematic effect, their efficiencies will be directly determined using the experimental data. In the proposed experiment, four tracking elements are used, however the trigger condition does not include their signals. In principle, removing the aerogel Cherenkov signals from the trigger [6], it is possible to reconstruct the particle trajectory also for $K_{\mu 2}$ using three tracking elements. The particle identification can be carried out from the TOF measurement. Therefore, the efficiency can be determined by comparing signals from a particular element with the tracks reconstructed by the others. By changing the combination of the elements, we can determine the efficiency of all the tracking elements for each particle species e^+ and μ^+.

In general, the efficiency of the trackers (ϵ) should be high, and thus the statistical fluctuation for the number of events of the relevant tracking elements can be written as,

$$\sigma = \sqrt{N \cdot \epsilon(1-\epsilon)} \sim \sqrt{N \cdot (1-\epsilon)} \tag{48}$$

$$\frac{\sigma}{N} \sim \frac{\sqrt{1-\epsilon}}{\sqrt{N}} \tag{49}$$

[6] Although it is written that signals from the Cherenkov counter will be used for the trigger, this scheme is not finalized and we have an option not to use the aerogel Cherenkov for the trigger.

Table 12: Summary of the performance check for the tracking and particle ID elements.

Element for check	Tracking elements	Trigger
C1	C2, C3, C4	TOF1⊗TOF2
C2	C1, C3, C4	TOF1⊗TOF2
C3	C1, C2, C4	TOF1⊗TOF2
C4	C1, C2, C3	TOF1⊗TOF2
PID by Cherenkov	C1, C2, C3, C4	TOF1⊗TOF2
PID by TOF	C1, C2, C3, C4	TOF1⊗C4

following a binomial distribution. Therefore, if ϵ is 99.9%, 99.0%, and 98.0%, $N = 10^3$, 10^4, and 2×10^4, respectively, are necessary to achieve $\sigma/N = 0.1\%$. We can easily accumulate 10^4 events due to K_{e3}, $K_{\mu 3}$ by changing the magnetic field of the spectrometer to $B = 0.9$ T. In the low momentum region, the particle identification by the TOF measurement is expected to be more reliable. In conclusion, the systematic uncertainty due to the tracker inefficiency and will be controlled to a level that is much smaller than the statistical sensitivity. If the efficiency difference is greater than the statistical error, this effect should be corrected. The procedure of the above efficiency check is summarized in Table 12. In conclusion, the systematic error due to the inefficiencies of the trackers will be less than 0.1%.

7.2.4 Performance check of particle identification

As well as the detector inefficiency, it is clear that particle misidentification introduces an additional error. The e^+ inefficiency and misidentification of μ^+ as e^+ by the aerogel Cherenkov counter can easily change the R_K value. Also, the particle misidentification by the TOF measurement introduces a systematic error. In order to confirm the performance of the particle identification by the TOF and aerogel Cherenkov counters, the probability of misidentification will be directly measured using the experimental data.

Probabilities of the e^+ inefficiency and the μ^+ misidentification by the aerogel Cherenkov counter can be determined using the same data set mentioned in Section 7.2.3, as shown in Table 12. The performance of the Cherenkov counter can be checked by comparing signals from the Cherenkov counter with the TOF measurement. It is to be noted that four-point tracking can be used for this study. Then, removing both the TOF2 and aerogel Cherenkov signals from the trigger and adding the C4 signals into the trigger, the data will be collected by setting the magnetic field to 0.9 T. Requiring and vetoing aerogel Cherenkov signals, the TOF mass spectrum will be obtained and the TOF performance can be precisely checked. In conclusion, the systematic uncertainty due to non-ideal performance of the particle identification will be controlled to a level less than 0.1%, which is analogous to the discussion in Section

7.2.3. This value is smaller than the statistical sensitivity.

7.2.5 Radiative correction

In the proposed experiment, the first observation of the $K^{IB}_{e2\gamma}$ process is expected and we can check the theoretical calculation by comparing with the experimental results. Since the $K^{IB}_{e2\gamma}$ events contribute to the D0e and D1e data, the internal consistency between the two samples can be carefully checked and we will be able to evaluate the correctness of the theoretical model adopted in this analysis. In this sense, the systematic error due to radiative correction is less than 0.1%.

7.2.6 K_{e2} acceptance loss due to high energy bremsstrahlung emission

External bremsstrahlung photons are emitted nearly parallel to the e^+ direction. They will pass through the holes without hitting the calorimeter and we will miss these events. However, some e^+s will lose their momentum by emitting high energy bremsstrahlung photons and they will not be accepted in the analysis. Therefore, the treatment of external bremsstrahlung photons in the Monte Carlo simulation is very important because this uncertainty directly introduces a systematic error. In order to check the correctness of the bremsstrahlung in the simulation, the following analyses will be performed.

- The e^+ momentum distribution above K_{e3} endpoint should be correctly reproduced by the Monte Carlo simulation.
- The energy distribution of the external bremsstrahlung photons measured by the GP detector should be reproduced by the simulation.
- The e^+ momentum distribution obtained by requiring a GP hit should be correctly reproduced by the simulation.
- The GP counting rate as a function of the e^+ flight length in the K^+ stopper should be reproduced by the simulation.
- R_K should be obtained as a function of the e^+ flight length in the K^+ stopper and the consistency should be carefully checked.

After a check of these necessary conditions, we will reduce this systematic error to $\Delta R_K/R_K = 0.1\%$ due to the uncertainty of the K^+ decay vertex.

7.2.7 Summary of systematic errors

Here we considered the systematic errors due to (1) background contamination, (2) inefficiency of tracking detectors, (3) particle identification by the TOF measurement and aerogel Cherenkov counter (4) radiative correction, (5) K_{e2} acceptance loss due to high energy bremsstrahlung emission, as summarized in Table 13. The total systematic error is obtained to be $\Delta R_K/R_K = 0.1\%$ by adding all items in quadrature.

Table 13: Summary of the systematic errors. The total systematic error is obtained to be $\Delta R_K/R_K = 0.1\%$ by adding all items in quadrature.

Items	Error size of $\Delta R_K/R_K$
(1)Background	<0.1%
(2)Efficiency of tracking elements	<0.1%
(3)Particle identification	<0.1%
(4)Radiative correction	<0.1%
(5)External bremsstrahlung	0.1%
Total systematic error	0.1%
Statistical error	0.2%

The systematic error is estimated to be about half of the statistical one. The error sizes of the NA62, KLOE, and TREK experiments are visualized in Fig. 26. The central value of the TREK experiment is just assumed to be the same as the NA62 result.

7.3 Constraint to SUSY model

The expected sensitivity of the proposed experiment is $|\Delta R_K/R_K| = 0.2\%(\text{stat.}) \oplus 0.1\%(\text{syst.})$. Using this value we can constrain the parameters in LFV SUSY model. From Eq. (7), the deviation of the R_K value from the SM can be described using the Higgs mass, $\tan\beta$, and Δ_{13} parameters, and the relation of these parameters should be limited by the bounds of the proposed experiment. Fig. 27 shows the expected constraint in M_H and $\tan\beta$ at 90% confidence level obtained using three typical Δ_{13} values ($\Delta_{13} = 1 \times 10^{-4}$, 5×10^{-4}, and 1×10^{-3}).

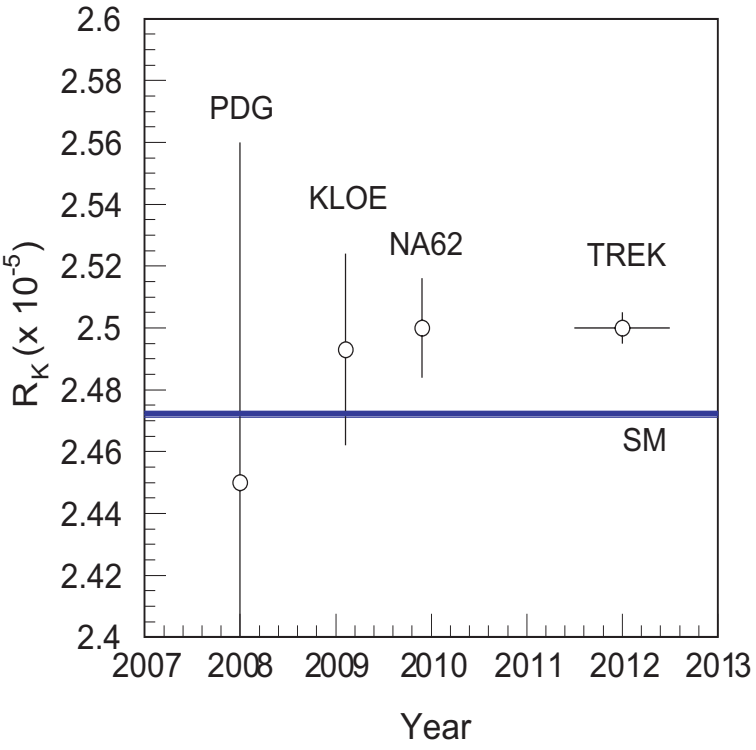

Figure 26: Summary of the error sizes of the NA62, KLOE, and TREK experiments. The central value of the TREK experiment is just assumed to be the same as the NA62 result.

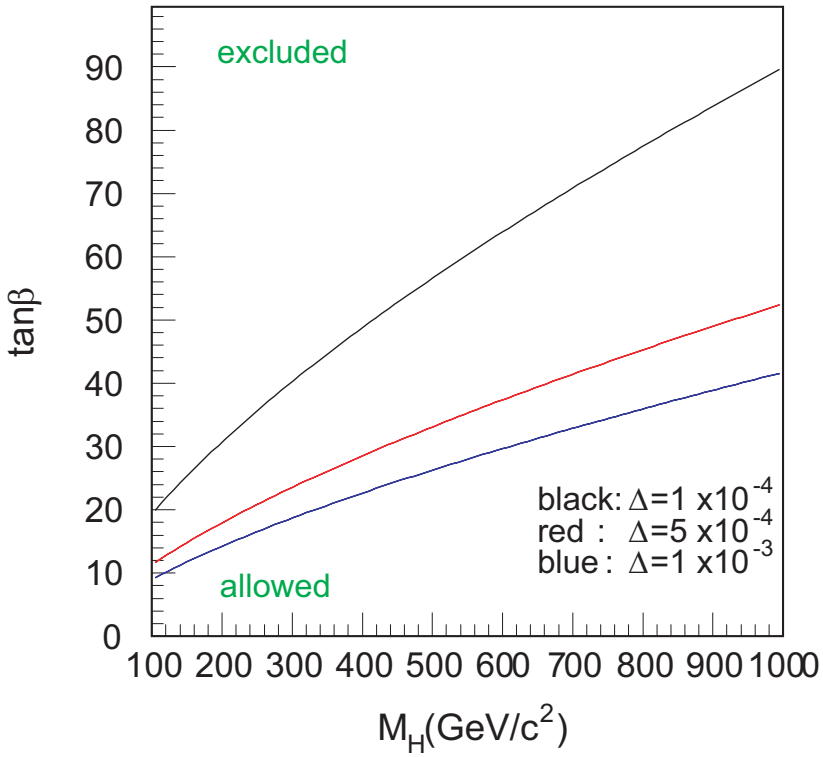

Figure 27: Constraint to M_H and tanβ. The constraint curves at the 90% confidence level are obtained by assuming typical Δ_{13} values.

Search for heavy neutrino in $K^+ \to \mu^+ N$ decay

8 Physics motivation of heavy neutrino search

8.1 Description of νMSM

In the search for physics beyond the Standard Model (SM), one can use different types of guidelines. A possible strategy is the attempt to explain phenomena that are not described by the SM by minimal extensions, that is by introducing the smallest possible number of new particles without adding any new physical principles or a new energy scale. An example of such a theory is the renormalizable extension of the SM, the νMSM (neutrino Minimal Standard Model) [15, 16, 53], where three light singlet right-handed neutrinos (sterile neutrinos) are introduced. The νMSM can simply explain

- Neutrino oscillation,
- Dark matter as sterile neutrinos, and
- Baryon asymmetry induced from leptogenesis via sterile neutrino oscillation.

The SM is originally formulated with massless neutrinos as components of the electroweak SU(2) doublets. To accommodate the neutrino masses, one can add several electroweak singlets to build the seesaw Lagrangian as,

$$L_{\nu\mathrm{MSM}} = L_{\mathrm{SM}} + N_I i d_\mu \gamma^\mu N_I - F\alpha I L_\alpha N_I \Phi - M N_2 N_3 - \Delta M_{IJ}/2 N_I N_J + h.c., \quad (50)$$

where N_I are the right-handed singlet leptons, Φ and L_α ($\alpha = e, \mu, \tau$) are the Higgs and lepton doublet, F is the matrix of Yukawa couplings, and M is the common mass of two heavy neutral fermions. ΔM_{IJ} are related to the mass of the lightest sterile neutrino N_1 responsible for Dark Matter (DM). Also, Δ_{IJ} produces the small splitting of the masses of N_2 and N_3.

The leptonic section of this theory has the same structure as the quark section, i.e. every left-handed fermion has its right-handed counterpart. All of the sterile neutrinos have masses below the electroweak scale: one has a mass of the order of a few keV, while the two remaining sterile neutrinos are assumed to be closely degenerated at a scale of about 0.1−10 GeV. The lightest singlet fermion N_1 may have a lifetime greatly exceeding the age of the Universe and may thus play the role of a DM particle. The DM sterile neutrino is likely to have a mass in ∼keV region. Within the framework of the νMSM, the baryon asymmetry can be naively explained though CP-violating sterile neutrino oscillation in the Early Universe. The kinetics of these oscillations and transfer of lepton number between active and sterile neutrino

sectors has been considered. For masses of sterile neutrinos exceeding ∼20 GeV, the mechanism does not work as the sterile neutrinos equilibrate.

If the sterile neutrinos are lighter than the kaons, they can give rise to leptonic and semileptonic decay with relatively large branching ratios. This gives a possibility to confirm or rule out the νMSM with light sterile neutrino by kaon decay experiments.

8.2 Constraint on the model parameters

The Yukawa coupling constants of the DM neutrino $|F_{\alpha 1}| < 10^{-12}$ are strongly bounded by cosmological consideration and X-ray observations. For the present discussion field N_1 can be omitted from the Lagrangian. So, with the definition $f_\alpha = |F_{\alpha 2}|$, we arrive at

$$Ł_N = -\frac{1}{\sqrt{2}} f_\alpha L_\alpha (N_2 + N_3)\Phi - \frac{M_2}{2} N_2^c N_2 - \frac{M_3}{2} N_3^c N_3 + h.c., \tag{51}$$

where masses M_2 and M_3 must be almost the same (baryogenesis constraint). For a successful baryogenesis the active-sterile mixing must be small enough, otherwise N_2 and N_3 come to thermal equilibrium above the electroweak scale and the baryon asymmetry is diminished. This leads to the upper bound

$$\frac{f_\alpha^2 \nu^2}{2M^2} = U^2 < 2k \cdot 10^{-8} (\mathrm{GeV}/M)^2 \tag{52}$$

with $k = 1(2)$ for the case of normal (inverted) hierarchy in the active neutrino sector. The lower bound on U can be derived as well from the required mass-mixing pattern in active neutrino sector.

$$U^2 > 1.3k \cdot 10^{-11} (\mathrm{GeV}/M)^2. \tag{53}$$

To present quantitative predictions, three sets of Yukawa couplings corresponding to three "extreme hierarchies", which thus mostly determines the overall strength of mixing U^2. Here we consider three sets of coupling constants given by

$$I \quad : \quad f_e^2 : f_\mu^2 : f_\tau^2 \sim 52 : 1 : 1 \tag{54a}$$

$$II \quad : \quad f_e^2 : f_\mu^2 : f_\tau^2 \sim 1 : 16 : 3.8 \tag{54b}$$

$$III \quad : \quad f_e^2 : f_\mu^2 : f_\tau^2 \sim 0.061 : 1 : 4.3. \tag{54c}$$

8.3 Contribution to kaon decays

From the νMSM calculation, heavy sterile neutrinos can contribute to kaon decays, if sterile neutrinos are lighter than kaons. According to the literature, the predictions of the branching ratio in two-body and three-body decays $K^+ \to l^+ N$ and $K^+ \to \pi^0 l^+ N$ were obtained to be $BR \leq 10^{-6}$ using the above parameter sets, as shown in Fig. 28 [15, 16].

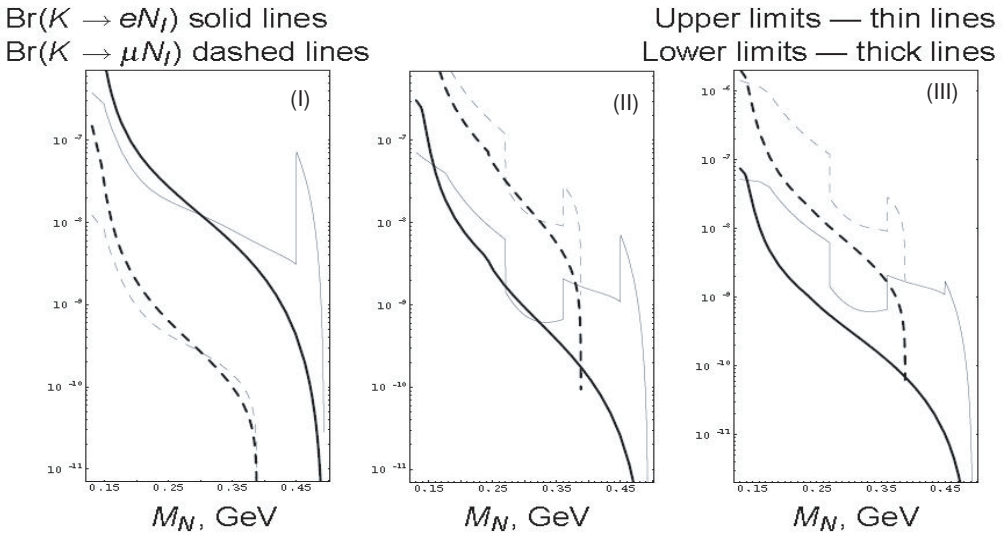

Figure 28: $K^+ \to e^+N$ (solid lines), $K^+ \to \mu^+N$ (dashed lines) branching ratio calculated as a function of sterile neutrino mass in the framework of νMSM. In a phenomenologically viable model, the branching ratios are confined between corresponding thin and thick lines which show upper and lower limits on U^2. Figures I, II, and III, correspond to the difference of coupling constants for Eq. (54a), Eq. (54b), and Eq. (54c), respectively.

A peak structure is expected in the momentum spectra in case of two body decay. In addition to the momentum measurement, the muon polarization can be measured for the muon channel. Therefore, we can improve the sensitivity for the sterile neutrinos by measuring both the μ^+ momentum and the μ^+ polarization simultaneously. It should be emphasized that the muon polarization measurement is very powerful as it takes advantage of detecting the contribution of righthanded current to the generation of heavy neutrino. Also, the peak structure will be measured in the momentum and polarization distributions at the same position and width. We can thus drastically reduce the systematic error and the experimental result will be quite reliable.

9 Experimental situation of heavy neutrino search

9.1 KEK-PS E99 experiment

The muon momentum spectrum in $K_{\mu 2}$ decay was measured by using a high-resolution magnetic spectrograph to look for a discrete muon peak associated with heavy-neutrino emission [54]. The spectrum revealed no distinct peak, and the upper bound of the mixing ratio between the muon neutrino and a massive neutrino was determined to be $10^{-4} - 10^{-6}$ in the mass range of $70 - 300$ MeV/c^2.

The experiment (KEK-PS E99) was performed at the K3 beam channel of the

Table 14: Comparison of the previous experiment and the proposed one. The attainable branching ratio is about 100 times sensitive for the proposed experiment.

Items	KEK-PS E99	This proposal
$\Omega(\mu^+)$	0.8%	7%
$\Omega(\pi^0)$	92%	>99.9%
spectrometer	dipole, 4 trackers	toroidal, 4-5 trackers
calorimeter	$11.5X_0$ NaI(Tl)	$13.5X_0$ CsI(Tl)
μ^+ polarimeter	not used	used
sensitivity	10^{-6}	10^{-8}

12-GeV KEK-PS. The experimental configuration is shown in Fig. 29. They reported on the result using a high-resolution magnetic spectrograph with a wider momentum range (100−250 MeV/c) and much better momentum resolution. Furthermore, a very effective photon veto system using NaI(Tl) counters to suppress the continuum background was employed. An argument has been made that the expected ν_τ mass may fall in the mass range just covered by this experiment (70-300 MeV/c^2).

The veto efficiency of the $\mu^+\pi^0\nu$ mode was quite high (as high as better than 99%) because of 2γ emission, better than 99%, while the $\mu^+\nu\gamma$ mode was difficult to eliminate. Even with 92% solid-angle coverage by the NaI counters, about 30% of the $\mu^+\nu\gamma$ photons escaped undetected for $P_\mu \leq 220$ MeV/c, becoming much worse toward the 236-MeV/c peak, since low-energy photons are preferentially emitted along the muon momentum direction.

The momentum resolution at 236 MeV/c was 2.1 MeV/c FWHM (0.9%) with a perfectly Gaussian line shape, and decreases gradually toward lower momenta. There was no distinct peak in the muon momentum spectrum except for the normal one at 236 MeV/c. They set the upper limit on the mass and mixing of heavy neutrinos. In terms of the mixing ratio $|U_{\mu i}|^2$, where i is presumably 3 in the ordinary $\nu_e \simeq \nu_1$ and $\nu_\mu \simeq \mu_2$ assignment, the 90% confidence-level limit was about 10^{-5} for the $m_{\nu_i} = 100$ MeV/c^2 and 10^{-6} for the $m_{\nu_i} = 200 - 300$ MeV/c^2. The limit became exceedingly loose for higher masses as shown, e.g. 10^{-4} for $m_{\nu_i} = 70$ MeV/c^2, because of the $\mu^+\nu\gamma$ background and the finite momentum resolution of the spectrograph.

9.2 CERN PS191 experiment

They have performed an experiment specifically designed to look for neutrino decays into $e^+e^-\nu$ with negative results and gave the limits for the couplings to ν_e and ν_μ.

The CERN PS191 experiment was performed in July-August 1984 in parallel with an exposure of the BEBC bubble chamber using 19.2 GeV protons from the CERN Proton Synchrotron. A focusing magnetic horn was operated every other PS burst (namely every 2.4 s); the alternate burst was unfocused because of limitations in

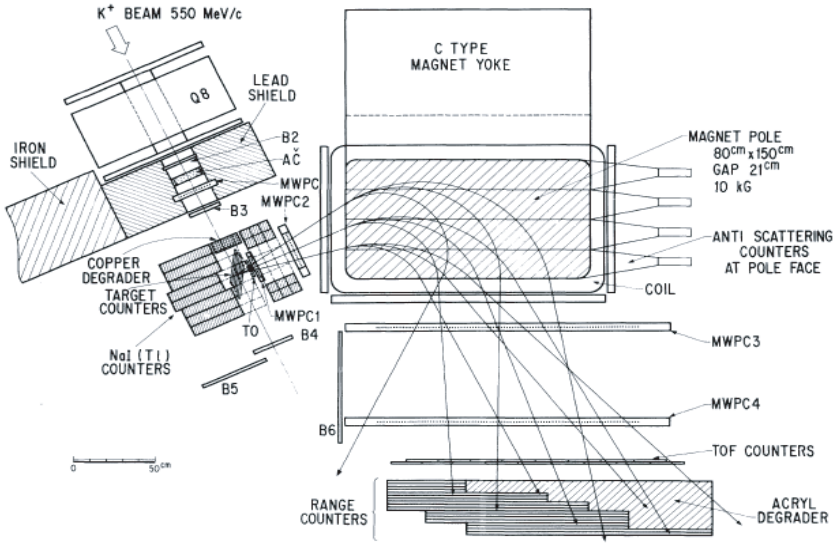

FIG. 1. Plan view of the neutrino mass spectrograph.

Figure 29: Schematic view of the previous experimental setup of KEK-PS E99. The μ^+ momentum spectrum has been measured by using a high-resolution magnetic spectrograph to look for a discrete muon peak. The $K_{\mu 3}$ backgrounds were suppressed by detecting γs from π^0.

the horn repetition rate. The total number of protons on target was 0.86 $\times 10^{19}$ of which 0.56 $\times 10^{19}$ were in the focused and the rest in the unfocused mode. The detector was located in a pit whose center was 128 m from the target and 40 mrad off the beam axis because the beam was directed towards the BEBC chamber. Fig. 30 shows a general view of the beam, the pit and the detector. The neutrino flux was calculated using two independent and well-established Monte Carlo programs. The secondary particle spectra used by these programs were based on and extrapolated from measurements giving the shape and absolute normalization of particles produced by 19.2 GeV protons on a beryllium target.

The apparatus consisted of two parts: (a) a 12 m long volume of 18 m^2 cross-sectional area where decaying neutrinos were detected by chambers with low material content; (b) an electromagnetic calorimeter of 7 radiation lengths in which showers from electrons and photons were detected and measured. The results depend upon the hypothetical neutrino mass. They are essentially independent of the type of neutrino (Dirac or Majorana) assumed for the ν_h. The limits at the 90% confidence level for the products of the relevant mixing matrix elements were obtained. The limits from this experiment were 2 to 3 orders of magnitude better than the previous ones.

This experimental result sets a constraint for νMSM in the region of neutral lepton mass $M < 450$ MeV. Fig. 31 shows the constraint for the neutrino lifetime and the mixing matrix from the PS191 experiment and other conditions. The $K^+ \to \mu^+ N$

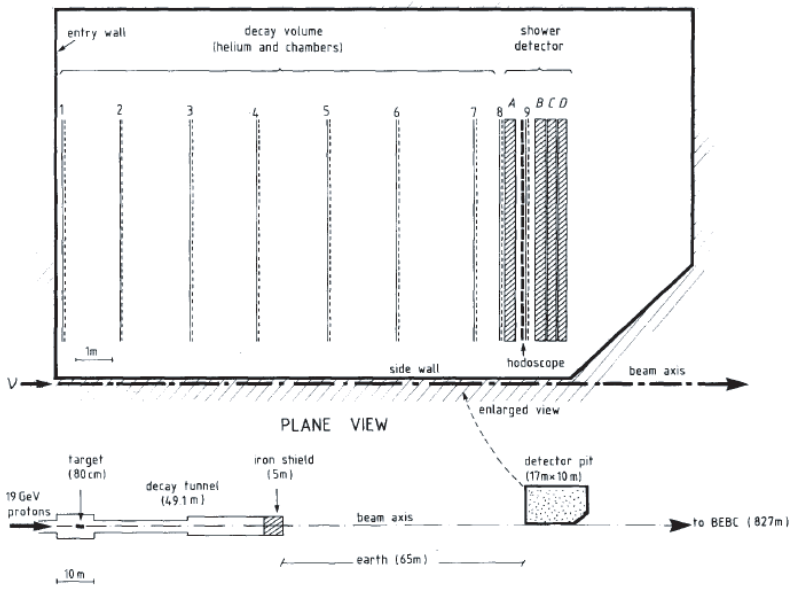

Figure 30: A general view of the beam, the pit and the detector in the CERN PS191 experiment.

branching ratio shown in Fig. 28 is calculated based on this constraint.

10 Proposed experiment for heavy neutrino search at J-PARC

10.1 Overview of the experiment

In the TREK experiment, we will search for the transverse muon polarization in $K^+ \to \pi^0\mu^+\nu$ by measuring the μ^+ momentum, π^0 momentum, and μ^+ polarization. Therefore, the TREK apparatus is very suited for the heavy neutrino search because

- The μ^+ momentum generated from the $K^+ \to \mu^+ N$ decay is monochromatic. A peak structure is formed in the momentum spectrum.
- Since the μ^+ is generated through a right-handed current, the μ^+ polarization in the direction of μ^+ motion is 100% and opposite of that from the normal $K^+ \to \mu^+\nu$ decay.

In addition to the detector system for the $\Gamma(K_{e2})/\Gamma(K_{\mu 2})$ measurement, which consist of the toroidal spectrometer and the CsI(Tl) calorimeter, the muon polarimeter will be used for the measurement of the longitudinal muon polarization. Two settings of the magnetic fields $B = 1.4$ T and 0.65 T will be chosen to cover a wide μ^+ momentum region. It should be noted that the experimental data with the

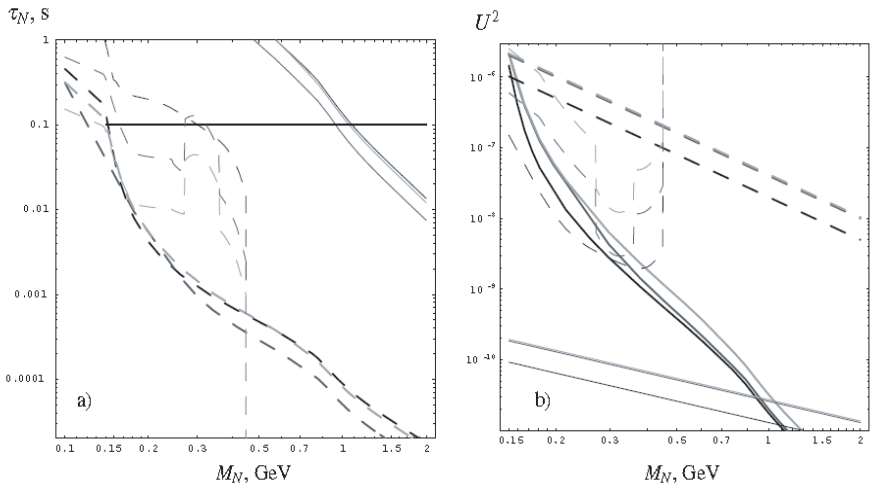

Figure 31: Upper (solid lines) and lower (dashed lines) limits on (a) neutrino lifetime and (b) overall mixing U^2 in model 1 (black), 2 (dark gray), and 3 (lightgray). Thin dashed lines corresponds to limits from the CERN PS191 experiment. A thick solid black line indicates the upper limit from Big Bang Nucleosynthesis, the thin solid lines are limits from Eq. (53), and the thick dashed lines are from Eq. (52).

former setting will be taken together with the $\Gamma(K_{e2})/\Gamma(K_{\mu 2})$ experiment. The μ^+ momentum is analyzed by the spectrometer and the μ^+ is identified by the TOF measurement. After passing through the spectrometer, the muons are slowed down by a copper degrader and stop in the polarimeter. The magnetic field from the spectrometer magnet is shielded by adding new iron plates and an external decouping field of $\sim$10 Gauss is applied to preserve the muon polarization in longitudinal direction. The muon polarization in the longitudinal direction is measured as position asymmetry from $\mu^+ \to e^+\nu\bar{\nu}$ in forward and backward directions.

The main background is the $K^+ \to \pi^0\mu^+\nu$ decay with escape of both photons from the muon and beam holes of the calorimeter. In order to suppress these events, we have two options: (1) a dedicated photon veto system is installed outside the calorimeter for the detection of the escaping photons; (2) half of the muon holes are filled up with additional veto detectors. Also, the GP counters can be used as veto counters. The momentum resolution is very important to get good sensitivity for a peak search and it can be improved up to ~ 1 MeV/c by the energy loss measurement of charged particles in the target.

The experimental sensitivity mainly depends on 3 parameters: (1) K^+ statistics (running time $\times$ beam intensity), (2) muon momentum resolution, and (3) $K_{\mu 3}$ background fraction. Since the effects from the heavy neutrino should be observed in the μ^+ momentum distribution and μ^+ polarization as a peak structure at the same position and width, we can reduce the systematic error to be much smaller than the statistical error.

10.2 Muon polarimeter

The muon polarimeter used in the previous E246 experiment will be reused. We will not yet use the proposed new TREK active polarimeter. In E246, the magnetic field to preserve the transverse component of the muon polarization was applied by guiding the fringing field of the superconducting toroidal magnet with shim plates. The longitudinal component was rotated by this field. In the proposed experiment, a small longitudinal field will be applied in order to preserve the longitudinal polarization component P_L, as shown in Fig. 32. The longitudinal component is then detected as a forward-backward asymmetry of the decay positron with respect to the muon stopper. The structure of the polarimeter is shown in Fig. 33. Since the typical strength of stray field in the experiment area including the earth field is smaller than 1 Gauss, an external decoupling field of about 10 Gauss will be strong enough. The field from the spectrometer magnet is screened by an iron-shim plate and a newly installed return plate. An air-cooled low-power coil wound around the muon stopper produces field of a 10 Gauss. In this way, a large analyzing power is ensured, which is essential to detect the effect from the sterile neutrino.

The muon stopper is required to be thick enough to stop muons, but it must also allow the positron to escape. An array of eight 6-mm thick pure aluminum slabs, 160 mm wide and 500 mm long, with 8 mm spacing is used. The stopping efficiency for $K_{\mu 3}$ muons was estimated to be $\sim 80\%$. It is well known that muons embedded in pure Al show neither initial loss of polarization nor spin relaxation.

In order to measure the longitudinal polarization, two plastic scintillating counters are put in front of the stoppers (B counter) and behind them (F counter), as shown in Fig. 33. The μ^+ polarization is obtained from the difference of e^+ counting rates in the F and B counter. The measurement of muon polarization is based on the asymmetry of positrons emitted in muon decay with a lifetime of 2.2 μs. The forward/backward asymmetry of muon decay positions is determined as the ratio

$$A = \frac{N_F - N_B}{N_F + N_B} \tag{55}$$

where N_F and N_B are the time-integrated positron counts observed by the F and B counters, respectively. The F and B counters are also used as a trigger and a veto in the prompt timing to require muon stop in the stopper plate. Since the P_L component of the $K_{\mu 3}$ events is also preserved by the magnetic field, this is used for monitoring the muon polarization of the $K_{\mu 3}$ backgrounds.

10.3 π^0 veto system

The main background in the proposed experiment is the $K_{\mu 3}$ decay with a 2 photon escape through the holes without hitting the calorimeter for the $B = 0.65$ T setting. Since the $K_{\mu 3}$ decay is one of the main channels of the K^+ decay with a branching ratio of $\sim$3.2%, we have to reduce these events as much as possible to obtain high sensitivity to the heavy neutrino search. The $K_{\mu 3}$ contamination is basically due to

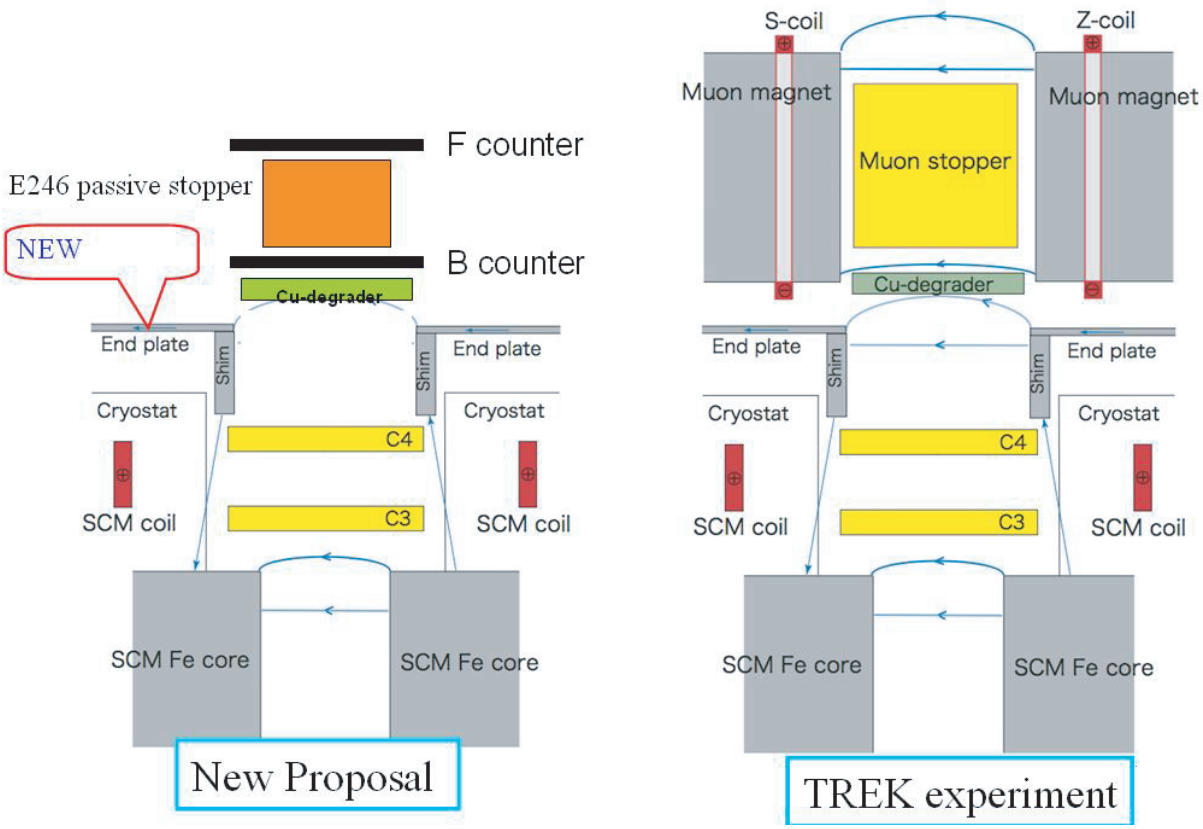

Figure 32: Schematic view of the magnetic field arrangement at the polarimeter position for (a) the proposed experiment and (b) the TREK experiment. In the proposed experiment, we measure the longitudinal component of the muon polarization.

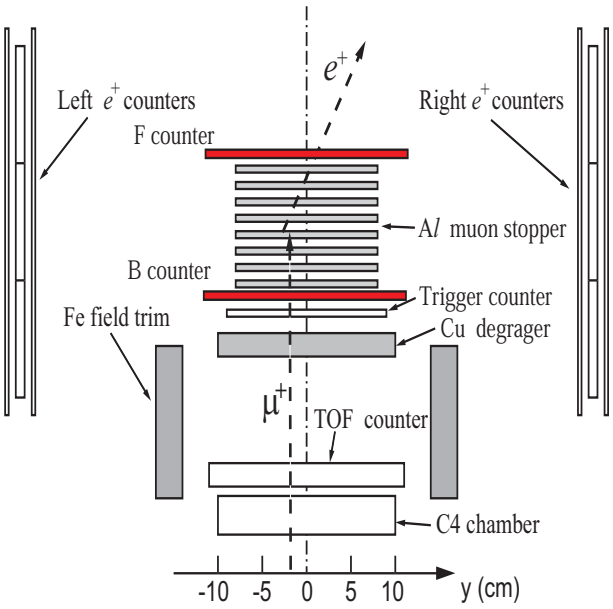

Figure 33: Layout of the polarimeter configuration. The muon stopper is an array of eight aluminum plates. The longitudinal component of the muon polarization is measured as the positron asymmetry in forward and backward direction with respect to the muon stopper. Two plastic scintillating counters are put in front of and behind the stoppers. These counters are also used as a trigger for the muon stopping in the plates.

the fact that the π^0 tends to be emitted in the opposite direction from the μ^+ and the associated photons at directed toward the holes, as shown in Fig. 34. We are going to reduce these background effects by installing additional photon counters.

The current design of the veto counter system is shown in Fig. 35. Now, we have two options: (1) the dedicated photon veto system is installed outside the calorimeter for the detection of the escaping photons; (2) half of the muon holes are filled with additional veto detectors. For the latter case, the whole veto system becomes simple at the cost of half of genuine events. The veto efficiency for (2) can easily be estimated by a simulation and has been obtained to be 0.85×10^{-3} of the single photon veto inefficiency, corresponding to 3×10^{-5} of the π^0 veto inefficiency. The GP counters help to remove the $K_{\mu3}$ backgrounds. Also, we can consider the possibility to fill the beam hole with counters, as shown in Fig. 35. Here it should be noted that the lifetime of the sterile neutrinos was limited to be > 0.01 s, as shown in Fig. 31 [15]. The photon detection and the $K_{\mu3}$ rejection do not affect the proposed experiment at all.

We do not need to suppress $K_{\mu3}$ backgrounds for the $B = 1.4$ T setting because only events around the endpoint region contribute to the data. Therefore, the heavy neutrino search can be performed together with the R_K measurement without using the veto system for this setting.

The $K_{\mu3}$ decay is the most serious and dangerous background, however it is worth listing other background components as,

- $K^+ \to \pi^+\pi^0$ and π^+ decays in-flight,
- IB component of $K^+ \to \mu^+\nu\gamma$,
- SD component of $K^+ \to \mu^+\nu\gamma$,
- $K^+ \to \pi^0\mu^+\nu\gamma$.

They were carefully studied by simulations and were concluded to be negligible.

10.4 μ^+ momentum resolution

Since we are going to search for a peak structure in the momentum and polarization distribution, one of the key parameters to improve the experimental sensitivity is the μ^+ momentum resolution. In the previous E246 experiment ($\sigma_P = 2.6$ MeV/c at 205 MeV/c), the charged particle momentum resolution was subject to uncertainty of charged particle track in the target because particle hit positions on C2, C3, and C4 MWPCs were used for the track reconstruction. In the proposed experiment, we will install the C1 GEM chamber, and a four point tracking can be performed. Since an average energy loss in the target is $\sim 5 - 6$ MeV, the momentum resolution is expected to be 1 MeV/c by the energy loss correction. This result is about a factor of 2 improvement from the E246 result.

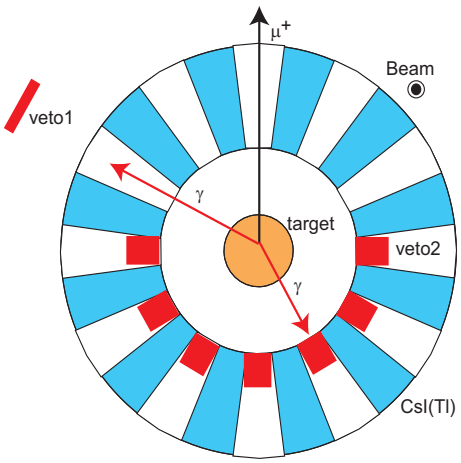

Figure 34: Schematic end view of the photon veto system. We can put veto detectors outside the calorimeter (veto1) and/or at the muon holes (veto2). The GP counter which already exists will further improve the rejection.

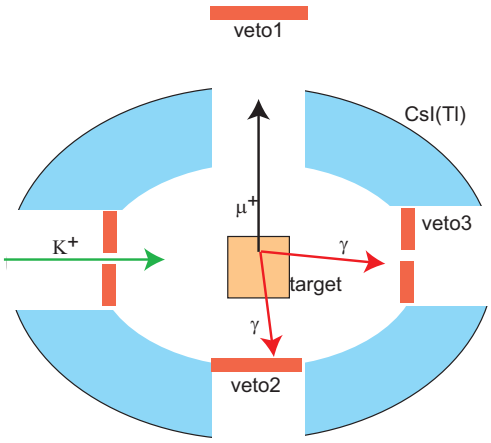

Figure 35: Schematic side view of the photon veto system. We can put veto detectors outside the calorimeter (veto1) and/or at the muon holes (veto2). The GP counter which already exists in the setup can further improve the rejection. In addition, we might add veto counters in the beam holes (veto3).

10.5 Experiment at J-PARC

The central magnetic fields of B=1.4 T and 0.65 T are employed for this experiment. The experimental data with the former setting will be taken together with the $\Gamma(K_{e2})/\Gamma(K_{\mu 2})$ experiment without the veto system. Hereafter the data collection with the B=0.65 T setting is described. Signals from the polarimeter trigger and veto counters are added to the trigger condition and an event is accepted when the following trigger requirement is satisfied:

$$\begin{aligned} TRG &= C_K \otimes \Sigma_i^{12}[TOF2_i \otimes (TOF1_{i-1} \oplus TOF1_i \oplus TOF1_{i+1})] \otimes \\ &\quad (0\gamma \text{ or } 1\gamma \text{ or } 2\gamma) \otimes (P_f \otimes \bar{P}_b), \end{aligned} \tag{56}$$

where

- C_K is the multiplicity condition of the Cherenkov K-ring>7,
- $TOF2_i$ is the counter TOF2 hit condition in the ith magnet sector,
- $TOF1_{i-1} \oplus TOF1_i \oplus TOF1_{i+1}$ is the hit condition in the ith TOF1 counter or its adjacent counter,
- 0γ, 1γ, 2γ are 0, 1, and 2 photon clusters, respectively, in the CsI(Tl) calorimeter.
- P_f is the F counter hit and $\bar{P}_b$ is the anticoincidence of the B counter in a prompt timing.

Here C_K is necessary to discriminate K^+ from π^+ by the Cherenkov counter. The $TOF1$ and $TOF2$ requirements are to confirm that a charged particle is transported through the toroidal spectrometer. $(0\gamma$ or 1γ or $2\gamma)$ is to pick up events with 0γ, 1γ, 2γ hits by the calorimeter. $P_f \otimes \bar{P}_b$ requires a muon stop in the polarimeter.

The proposed experiment will be performed during the low-intensity period of J-PARC MR. A 30 kW operation of the MR, corresponding to 220 kHz of the kaon beam intensity at the K^+ target position, is assumed. The experimental sensitivity of the $K^+ \to \mu^+ N$ branching ratio is improved to be better than 10^{-8} after 30 days of data collection (900 kW·day).

10.6 Byproduct physics

In the experiment to search for a heavy neutrino, it is also possible to look for $K^+ \to e^+ N$. Also the μ^+ polarization in $K^+ \to \mu^+ \pi^0 \nu$ and $K^+ \to \mu^+ \nu\gamma$ can be simultaneously measured. These polarizations provide the decay form factors as follows.

10.6.1 Search for heavy neutrino in $K^+ \to e^+ N$

Although the e^+ polarization cannot be measured, a peak search in the e^+ momentum distribution to look for a heavy neutrino signal is possible. Due to the small e^+ mass, we can access a higher mass region compared with the muon channel.

10.6.2 The $K^+ \to \mu^+\nu\gamma$ decay

In the proposed experiment, as well as in these spectroscopic studies, the μ^+ polarization from the SD effect can be measured. The SD term is sensitive to the electroweak structure of the kaon and has been the subject of chiral perturbation theory (ChPT) [55]. The μ^+ polarization has been calculated using the theoretically predicted SD amplitude [56]. Therefore, a precise measurement of μ^+ polarization in $K_{\mu 2\gamma}$ will offer a strict testing ground for the ChPT prediction by comparing with the results obtained from spectroscopic studies. Measurements of the in-plane μ^+ polarization distribution in $K_{\mu 2\gamma}$ have not been reported so far, only a measurement of P_T in $K_{\mu 2\gamma}$ was reported [57]. The theoretical form of the muon polarization in the $K^+ \to \mu^+\nu\gamma$ decay is described in Appendix B.

10.6.3 The $K^+ \to \pi^0\mu^+\nu$ decay

In $K_{\mu 3}$ decays, the matrix element is written as [1]

$$\begin{aligned} M &\propto f_+(t)[(P_K + P_\pi)_\mu \bar{l}\gamma_\mu(1+\gamma_5)\nu] + f_-(t)[m_l\bar{l}(1+\gamma_5)\nu] && \text{(57a)} \\ &\propto f_+(t)[\{(P_K + P_\pi)_\mu \bar{l}\gamma_\mu(1+\gamma_5)\nu + \xi(t)[m_l\bar{l}(1+\gamma_5)\nu\}], && \text{(57b)} \end{aligned}$$

where P_K and P_π are the four-momenta of the K and π mesons, m_l is the lepton mass, and f_+ and f_- are dimensionless form factors, which can depend only on $t = (P_K - P_\pi)^2$, the square of the four-momentum transfer to the leptons. $\xi(t)$ is the ratio of $f_-(t)$ and $f_+(t)$, and $Re(\xi)$ is related to the muon polarization. The μ^+ is expected to be polarized in the direction $\vec{A}$ with $\vec{P} = \vec{A}/|\vec{A}|$, where $\vec{A}$ is given by [58],

$$\begin{aligned} \vec{A} &= a_1(\xi)p_\mu - a_2(\xi)\left[\frac{p_\mu}{m_\mu}\{(m_K - E_\pi + \frac{p_\pi p_\mu}{|p_\mu|^2}(E_\mu - m_\mu)\} + p_\pi\right] && \text{(58a)} \\ &\quad + Im(\xi)(p_\pi \times p_\mu). && \text{(58b)} \end{aligned}$$

The form factors can be deduced by fitting the in-plane μ^+ polarization distribution. There are three published results but they have fairly large errors [59, 60, 61]. Needless to say the last term in Eq. (58b) corresponds to the T-violating muon polarization being pursued in the TREK experiment.

11 Experimental sensitivity of heavy neutrino search

A Monte Carlo simulation was performed to study the experimental sensitivity for the heavy neutrino search with the TREK apparatus. The muon polarization with $K_{\mu 3}$ background events was first studied, as shown in Fig. 36. The longitudinal polarization was obtained by integrating over all ν and π^0 directions. For simplicity, the type-2 veto system, mentioned in Section 10.3, was assumed in the simulation and the $K_{\mu 3}$ veto efficiency was obtained to be $(1 - 3 \times 10^{-5})$. The polarization of

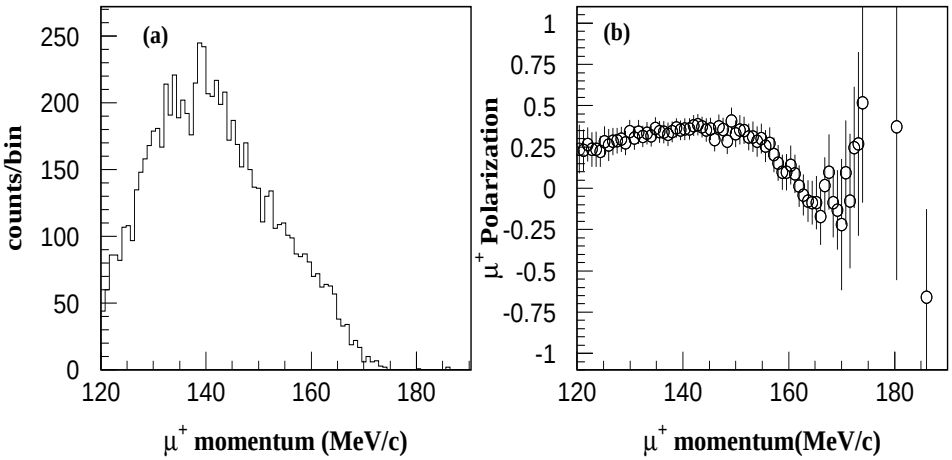

Figure 36: $K_{\mu 3}$ spectra: (a) μ^+ momentum and (b) μ^+ polarization obtained in the simulation.

the surviving $K_{\mu 3}$ events is about 25% below 155 MeV/c. The muon momentum distribution has a peak-like structure at $P_\mu = 140$ MeV/c, which depends on the $K_{\mu 3}$ kinematics and the configuration of the veto system.

The statistical sensitivity strongly depends on the running time of the experiment, μ^+ momentum resolution (σ_P), and $K_{\mu 3}$ veto efficiency (ϵ), which were assumed to be 30 days, 1 MeV/c, and $(1-3\times10^{-5})$, respectively, in this estimation. In addition, the following parameters were:

- The kaon beam intensity is I_K =220 kHz
- The kaon stopping efficiency in the target (f) is 0.25
- The photon veto system is type-2 (see Section 10.3)
- Detector acceptance is $\Omega(K_{\mu N}) = 0.07\%/2 = 0.035\%$

The number of the accepted $K_{\mu N}$ events can be expressed as,

$$\begin{aligned} N(K_{\mu N}) &= I_K \cdot (30 \cdot 3600 \cdot 24) \times f \cdot \Omega(K_{\mu N}) \cdot BR(K_{\mu N}) && \text{(59a)} \\ &= 220 \times 10^3 \cdot (30 \cdot 3600 \cdot 24) \times 0.25 \times 0.035 \times BR(K_{\mu N}) && \text{(59b)} \\ &= 5.0 \times 10^9 \times BR(K_{\mu N}). && \text{(59c)} \end{aligned}$$

Also, the number of the $K_{\mu 3}$ background events is

$$\begin{aligned} N(K_{\mu 3}) &= I_K \cdot (30 \cdot 3600 \cdot 24) \times f \cdot \Omega(K_{\mu 3}) \cdot BR(K_{\mu 3}) \cdot (1-\epsilon) && \text{(60a)} \\ &= 220 \times 10^3 \cdot (30 \cdot 3600 \cdot 24) \times 0.25 \times 0.03 \times 3.3 \times 10^{-5} && \text{(60b)} \\ &= 8.4 \times 10^3 && \text{(60c)} \end{aligned}$$

Fig. 37 show the simulation results obtained by assuming $BR(K^+ \to \mu^+ N) = 2 \times 10^{-8}$ and monoenergy μ^+ peak at (a)(b) $P_\mu = 180$ MeV/c and (c)(d)$P_\mu = 150$ MeV/c. The heavy neutrino signal can be determined by fitting the μ^+ momentum and the μ^+ polarization simultaneously. This result indicates that the attainable sensitivity is better than $\sim 10^{-8}$ with reasonable beam power and time. The $K_{\mu 3}$ momentum spectrum has a peak-like structure and the experimental sensitivity depends on the $K_{\mu N}$ peak position. The systematic error is estimated to be much smaller than the statistical one because the requirement for the same position and the same width of the peaks in the momentum and polarization distributions is highly rigorous.

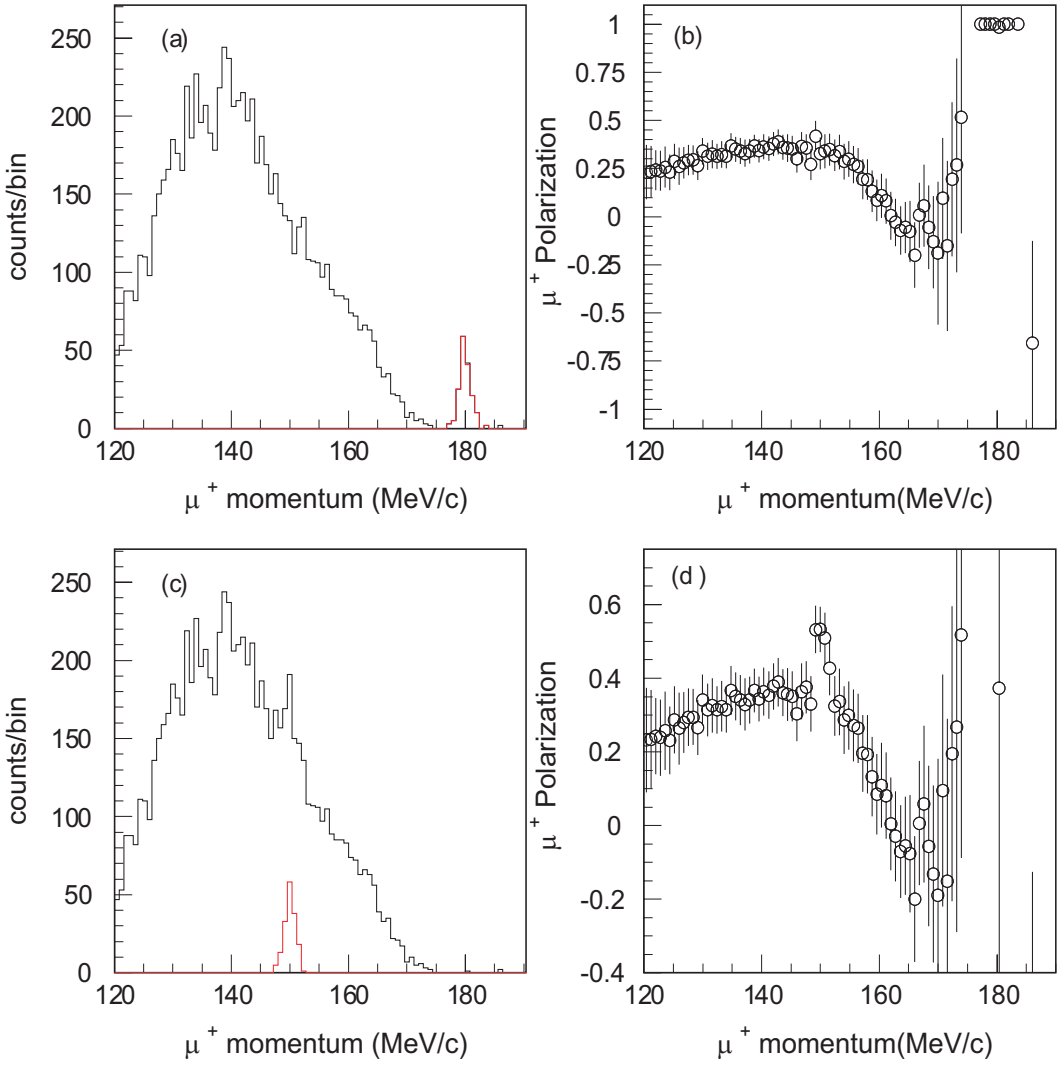

Figure 37: Distributions of (a)(c) μ^+ momentum and (b)(d) μ^+ polarization obtained by assuming $BR(K^+ \to \mu^+ N) = 2\times10^{-8}$ and monoenergy μ^+ peak at (a)(b) $P_\mu = 180$ MeV/c and (c)(d)$P_\mu = 150$ MeV/c. The heavy neutrino signal can be determined by fitting the μ^+ momentum and the μ^+ polarization simultaneously.

12 Beam time request

The beam time request for the R_K measurement and the heavy neutrino search is summarized in Table 15. Setting the magnetic field of the toroidal spectrometer to 1.4 T, the R_K measurement and the heavy neutrino search at high P_μ will be performed. Then, changing the magnetic field to 0.65 T, we will continue the heavy neutrino search at low P_μ. The requested physics time is 1500 kW·day for 1.4 T and 900 kW·day for 0.65 T. Also, additional run time (300 kW·day) for beam tuning, detector calibration, and so on, is requested. Most of the detector elements are common, and necessary detectors are summarized in Table 16.

Table 15: Summary of beam time and physics motivation.

Spectrometer field	1.4 T	0.65 T
Physics run time	1500 kW·day	900 kW·day
Total run time	1800 kW·day	900 kW·day
Physics	the lepton universality test & heavy neutrino search at high P_μ	heavy neutrino search at low P_μ
Constraint to	LFV SUSY model νMSM model	νMSM model

Table 16: Summary of necessary detectors. LFV and HN correspond to the lepton universality test and heavy neutrino search, respectively. $\circ$, $\times$, and $\circ^*$ correspond to necessary, not necessary, and preferable to use, respectively.

Detector	LFV	HN at high P_μ	HN at low P_μ	current status
Beam Cherenkov	$\circ$	$\circ$	$\circ$	to be modified
K^+ target	$\circ$	$\circ$	$\circ$	newly made
CsI(Tl)	$\circ$	$\circ$	$\circ$	to be modified
GP counter	$\circ$	$\circ$	$\circ$	exists
Additional γ counters	$\times$	$\circ^*$	$\circ$	newly made
Tracker :C1	$\circ$	$\circ$	$\circ$	newly made
Tracker :C2-C4	$\circ$	$\circ$	$\circ$	exists
Aerogel Cherenkov	$\circ$	$\times$	$\times$	newly made
TOF System	$\circ$	$\circ$	$\circ^*$	newly made
Polarimeter	$\times$	$\circ$	$\circ$	exists

13 Schedule

Here, we would like to express our strong commitment to engage in the commissioning of the K1.1BR line at J-PARC, develop the detector components of the TREK experiment, and perform the proposed experiments: (1) $\Gamma(K_{e2})/\Gamma(K_{\mu 2})$ and (2) heavy neutrino search, during the low-intensity period. Below, we present the rationale and strategy leading up to the TREK experiment.

13.1 Transfer of the SC toroidal spectrometer

For the proposed experiment we will employ the superconducting toroidal spectrometer which has been used for the KEK-PS E246 experiment. The total system of the magnet and He refrigerator will be transferred to J-PARC without modification. The spectrometer is movable by installing the whole system on rails, and it is possible to avoid the interference with other experimental groups. Note we will not occupy the experimental area.

13.2 Beam commissioning of K1.1BR

We will conduct beam commissioning and tuning of the K1.1BR beamline, whose beam optics was designed by the TREK group. The construction of K1.1BR will be finished by August in 2010 and the beam commissioning will be started in October. The K^+ intensity and π/K ratio will be carefully optimized for our series of planned experiments. The beam Cherenkov counters, MWPCs, TOF counters, and their electronics are being prepared for this beam tuning. We expect that a low-intensity beam ($\sim$5 kW) will be ready for use at the K^+ target position by the end of 2010. A good understanding of the kaon beam characteristics (beam profile, K/π ratio etc.) will be gained.

13.3 Detector preparation

We would like to have the toroidal spectrometer in place and furnished with the E246 MWPCs for the charged particle detection. The CsI(Tl) calorimeter with the new readout system will be reassembled and installed in the hadron hall. The new TOF system for both the start and the stop counters is designed to provide TOF resolution with better than 100 ps. A prototype counter will be constructed and the performance will be checked with cosmic rays. The planar GEMs which will be used as C1 in the TREK experiment will be designed and a prototype system will be tested using e^+ beams at Tohoku University or JLAB. The e^+ trigger system based on aerogel Cherenkov detection will also be tested at Tohoku University.

We are expecting that the operation power for the MR will be improved up to 30 kW in the near future. Then, we will implement the GEM detectors to improve the vertex reconstruction, the TOF system for the particle identification, the K^+ active target, and the aerogel Cherenkov counter. After installing all the detector elements,

we would like to run the experiment to measure the $\Gamma(K^+ \to e^+\nu)/\Gamma(K^+ \to \mu^+\nu)$ ratio with ∼30 kW beam operation. The experimental data for the heavy neutrino search in the high μ^+ momentum region will be simultaneously taken by installing the E246 polarimeter. We will continue the experiment for the heavy neutrino search in the low μ^+ momentum region by changing the spectrometer field and adding the photon veto counter system.

13.4 Further effort toward TREK

Finally we will realize the upgrade item-by-item towards the TREK experiment as the funding profile permits. After finishing the $\Gamma(K_{e2})/\Gamma(K_{\mu 2})$ and the heavy neutrino experiments, we will set up and commission the active polarimeter which will enable us to measure the normal, longitudinal and the transverse polarization of the decay muons from kaon decays. This task is essential for us to calibrate the polarimeter for the TREK experiment. If the J-PARC intensities reach their design values sooner, we will reconsider this strategy and begin the TREK experiment at the earliest possible date. A ten-fold increase in the beam intensity will also make these initial experiments much faster and this physics can still be addressed.

14 Cost estimation and funding

In addition to the existing resources used in the E246 experiment, we will prepare new detector elements for the proposed experiment such as,

- C1 GEM detector.
- Aero-gel Cerenkov counter for e^+ detection.
- TOF counter.
- Readout of CsI(Tl) calorimeter.
- Photon veto counters put at the muon and beam holes.

The estimated costs are summarized in Table 17. The new K^+ stopping target is already funded in Canada. We will apply for Grant-in-Aid research support for the detector construction cost. Regarding the spectrometer transfer, we would like to ask IPNS and KEK for support.

Table 17: Summary of Cost estimation

Items	number	Cost (kYen)		Total (kYen)
		to be funded	funded	
Spectrometer transfer				187,000
Superconducting magnet	1	37,000		
He refrigerator system	1	150,000		
Total for transfer				187,000
K^+ Stopping target			42,000	42,000
TOF System				10,700
TOF1	12	3,500		
PMT	24	2,800		
Sci.+LG+Ass.	12	6,000		
TOF2	12	4,800		
PMT (reused+new)	24	3,600		
Sci.(reused)+LG etc.	12	1,200		
Support etc.	13	2,400		
Tracking				44,900
C1-GEM	12	16,900		
QTC		12,000		
C2,C3,C4 (reused)	12	14,000		
C4 support	12	2,000		
CsI(Tl)				59,100
APD	800	23,000		
Amp.+Bias	800	10,400		
FADC		20,700		
Ass. etc.		5,000		
Cerenkov				24,000
Aerogel	120	9,600		
PMT	24	3,600		
Support		2,400		
Ass.		5,400		
Readout electronics		3,000		
Photon veto counter				2,760
Counter	6	1,800		
PMT	12	960		
DAQ/electronics		13,340		13,340
Total for detector				154,800

Acknowledgement

We acknowledge the help by the members of the KEK K-decay group. We are indebted to Prof. S. Mihara for valuable discussion and for a careful reading of this proposal. We would like to thank Prof. C.S. Lim for comments from the theoretical viewpoint.

References

[1] C. Amsler et al. (Particle Data Group), Phys. Lett. **B667** (2008) 1; http://pdg.lbl.gov/.

[2] Review for SM in reference [1].

[3] J.H. Christenson et al., Phys. Rev. Lett. **13** (1964) 138.

[4] Belle homepage, http://belle.kek.jp/.

[5] BaBar homepage, http://www.public.slac.stanford.edu/babar/.

[6] Review for MSSM in reference [1].

[7] Review for Neutrino mixing in reference [1].

[8] LHC homepage, http://lhc.web.cern.ch/lhc/.

[9] T2K homepage, http://www-nu.kek.jp/jhfnu/.

[10] T.K. Komatsubara, in proceedings of FPCP2004, arXiv:[hep-ex/0501016] (2005).

[11] TREK homepage, http://trek.kek.jp/.

[12] A. Masiero, P. Paradisi, and R. Petronzio, Phys. Rev. **D74** (2005) 011701(R).

[13] F. Ambrosino et al., Eur. Phys. J. **C64** (2009) 627-636; arXiv:[hep-ex/0907.3594] (2009).

[14] E. Goudzovski et al., in proceedings of KAON09, PoS (KAON09) 025.

[15] D. Gorbunov et al., in proceedings of KAON07, PoS (KAON) 047.

[16] S.N. Gninenko and D. Gorbunov, arXiv:[hep-ph/0907.4666v1] (2009).

[17] K.S. Babu and C. Kolda, Phys. Rev. Lett. **89**, (2002) 241802 .

[18] M. Sher, Phys. Rev. **D66**, (2002) 057301; A. Brignole and A. Rossi, Nucl. Phys. **B701**, (2004) 3.

[19] R. Kitano, M. Koike, S. Komine, and Y. Okada, Phys. Lett. **B575**, (2003) 300.

[20] A. Dedes, J.R. Ellis, and M. Raidal, Phys. Lett. **B549**, (2002) 159.

[21] A. Brignole and A. Rossi, Phys. Lett. **B566**, (2003) 217; E. Arganda, A.M. Curiel, M.J. Herrero, and D. Temes, Phys. Rev. **D71**, (2005) 035011.

[22] P. Paradisi, J. High Energy Phys. **02** (2006) 050; arXiv:[hep-ph/0601100] (2006).

[23] B.A. Campbell and D.W. Maybury, Nucl. Phys. **B709**, (2005) 419.

[24] M.J. Ramsey-Musolf, Phys. Rev. **D62**, (2000) 056009.

[25] J. Maalampi, V. Sipilainen, and I. Vilja, Phys. Rev. **D67**, (2003) 113005.

[26] A. Smirnov and R. Funchal, Phys .Rev. **D74**, (2006) 013001.

[27] H. Davoudiasl and L. Everett, Phys. Lett. **B634**, (2006) 55.

[28] A. Masiero, P. Paradisi, and R. Petronzio, arXiv:[hep-ph/0511289] (2005); A. Masiero and P. Paradisi, arXiv:[hep-ph/0609262] (2006).

[29] M. Moulson et al., in proceedings of KAON09, PoS (KAON09) 035 (2009).

[30] D. Pocanic et al., arXiv:[hep-ex/0907.4358] (2009).

[31] D.A. Bryman, in proceedings of KAON07, PoS(KAON) 052 (2007).

[32] E. Frle, D. Pocanic, and K. Assamagan, et al., Nucl. Inst. and Meth. **A526** (2004) 300.

[33] D. Pocanic, E. Frle, and V.A. Baranov, et al., Phys. Rev. Lett. **93** (2004) 181803.

[34] E. Frle, D. Pocanic, and V.A. Baranov, et al., Phys. Rev. Lett. **93** (2004) 181804.

[35] M. Bychkov, D. Pocanic, and B.A. VanDevender, et al., arXiv:[hep-ex/0804.1815] (2008).

[36] K. Horie Ph. D thesis, Phys. Lett. **B513** (2001) 311-318; S. Shimizu, Ph. D. thesis, Phys. Lett. **B495** (2000) 33.

[37] J.A. Macdonald et al., Nucl. Inst. and Meth. Phys. Res. Sect. **A506** (2003) 60.

[38] V. Cirigliano and I. Rosell, Phys. Lett. **99** (2007) 231801.

[39] G. Czapek et al., Phys. Rev. Lett. **70** (1993) 17.

[40] D.I. Britton et al., Phys. Rev. Lett. **68** (1992) 3000.

[41] A. Kawachi et al., Nucl. Inst. and Meth. **A416** (1998) 253.

[42] J. Simkin and C.W. Trowbridge et al., Rutherford report RL-79-097, Dec 1979.

[43] M. Abe et al., Phys. Rev. **D73** (2006) 072005.

[44] S. Shimizu et al., Phys. Lett. **B495** (2000) 33.

[45] K. Horie et al., Phys. Lett. **B513** (2001) 311-318.

[46] S. Shimizu et al., Phys. Lett. **B495** (2000) 33.

[47] M.A. Aliev et al., Phys. Lett.**B554** (2003) 7.

[48] S. Shimizu et al., Phys. Rev. **D70** (2004) 037101.

[49] S.G. Brown and S.A. Bludman, Phys. Rev. **136**, (1964) 1160; J.N. Huang and C.Y. Lee, Phys. Rev. **D27**, (1983) 2227. See Also P. De Baenst and J Pestieau, Nuovo Cim. **53A**, (1968) 407; and D. Bryman, P. Depommier and C. Leroy, Phys. Rep. **88**, (1982) 151.

[50] V. Cirigliano and I. Rosell, Phys. Rev. Lett. **99** (2007) 231801.

[51] C.H. Chen et al., arXiv:[hep-ph/0801.1074v1] (2008).

[52] S. Adler et al., Phys. Rev. Lett. **85** (2000) 2256.

[53] M. Shaposhnikov, Progress of Theoretical Physics, **122** (2009) 185.

[54] R.S. Hayano et al., Phys. Rev. Lett. **49** (1982) 1305.

[55] J. Bijnens et al., Nucl. Phys. **B396** (1993) 81; J. Bijnens et al., in The Second DAPHNE Physics Handbook, http://www.Inf.infn.it/theory/dafne.html.

[56] C.H. Chen et al., Phys. Rev. **D56** (1997) 6856.

[57] V.V. Anisimovsky et al., Phys. Lett. **B562** (2003) 166.

[58] N. Cabibbo and A. Maksymowicz, Phys. Lett. **9** (1964) 352.

[59] D. Cutts et al., Phys. Rev. **184** (1969) 1380.

[60] H. Braun et al., Nucl. Phys. **B89** (1975) 210.

[61] J. Bettels et al., Nuovo Cimento **A56** (1968) 1106.

A Appendix: Measurement of bremsstrahlung photons in the E470 experiment

A.1 KEK E470 experiment

The E470 experiment was designed to measure the radiative $K^+ \to \pi^+\pi^0\gamma$ ($K_{\pi 2\gamma}$), $K^+ \to \pi^0\mu^+\nu\gamma$ ($K_{\mu 3\gamma}$), and $K^+ \to \pi^0 e^+\nu\gamma$ ($K_{e3\gamma}$) decays using stopped positive kaons. The experiment was performed at the KEK 12 GeV proton synchrotron. The experimental apparatus was based on the E246 experiment. A Pb-plastic sandwich detector with 2.6 radiation lengths was installed at the outer radius of the magnet pole to monitor photons passing through the photon detector holes. For the analysis of the $K_{e3\gamma}$ decay, the $K^+ \to \pi^0 e^+\nu$ (K_{e3}) decay with a bremsstrahlung photon (BP) generated in the target was the most important background and this had to be carefully estimated. This is very similar situation to that in the proposed $\Gamma(K^+ \to e^+\nu)/\Gamma(K^+ \to \mu^+\nu)$ experiment.

In contrast to an in-flight K^+ experiment, the decay particles can be affected by interaction with the target in a stopped K^+ experiment. In principle, these K_{e3} backgrounds can be studied by a Monte Carlo simulation. In this appendix, the performance of the E470 detector system for rejection of the K_{e3} backgrounds and the experimental feasibility of the $K_{e3\gamma}$ decay are described. The behavior of the GP counters was studied when the obvious K_{e3} events were tagged by the detector system, and these events were compared with the simulation.

A.2 K_{e3} selection

The K_{e3} events were selected by the following K_{e3} selection conditions. The main cut conditions to extract the K_{e3} events were $-6000 < M^2_{\rm TOF} < 4000$ MeV$^2/c^4$, $80 < M_{\pi^0} < 140$ MeV$/c^2$, and $\theta_{e^+\pi^0} < 166°$, where $\theta_{e^+\pi^0}$ is opening angle between π^0 and e^+. The experimental K_{e3} spectra obtained with these conditions are in good agreement with the simulation obtained with the same cut conditions as the experimental data, as shown in Fig. 38.

A.3 Conclusion

Using these K_{e3} events, we determined the opening angle distribution between the e^+ and the BP detected by the GP counters ($\theta_{e^+{\rm BP}}$), where the BP hit position was assumed to be as the center position of the GP counter. Fig. 39 shows the correlation spectrum for $\theta_{e^+{\rm BP}}$ and $\theta_{\gamma{\rm GP}}$, where $\theta_{\gamma{\rm GP}}$ is smaller opening angle between the central position of the hit GP and two photons. The distinct locus at $\theta_{e^+{\rm BP}} = 0$ is mainly due to BP. In both the experimental and the simulation spectra, the GP counters located near the gap through which e^+ passed have significant events. Here it should be noted that the GP counter detected not only BP but also shower leakage from the CsI(Tl) calorimeter. The GP counter which detected the shower leakage was centered

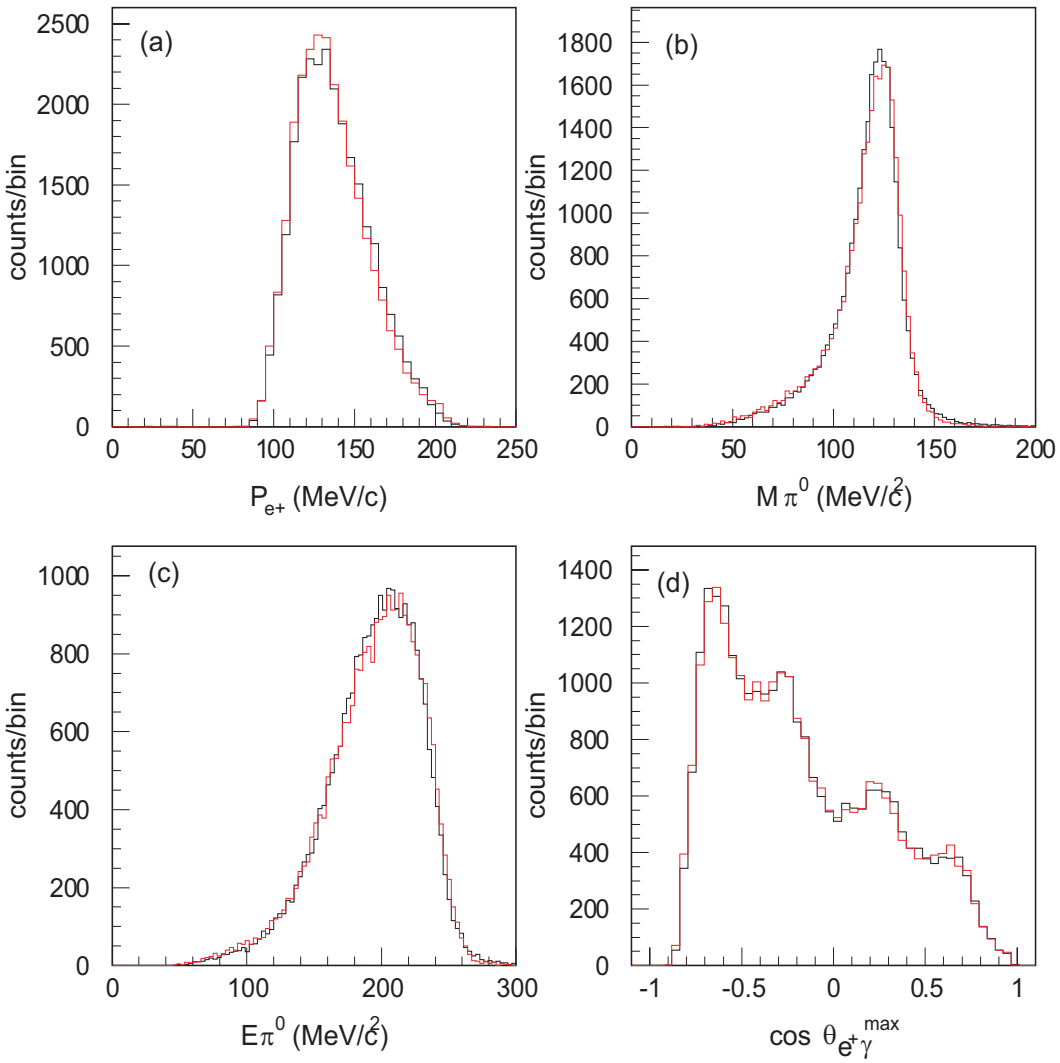

Figure 38: K_{e3} spectra: (a)e^+ momentum, (b)invariant mass of π^0, (c) π^0 energy, (d) smaller opening angle between e^+ and two photons. Red and black lines are the experimental data and the Monte Carlo simulation, respectively. The simulation spectra are in good agreement with the experimental ones.

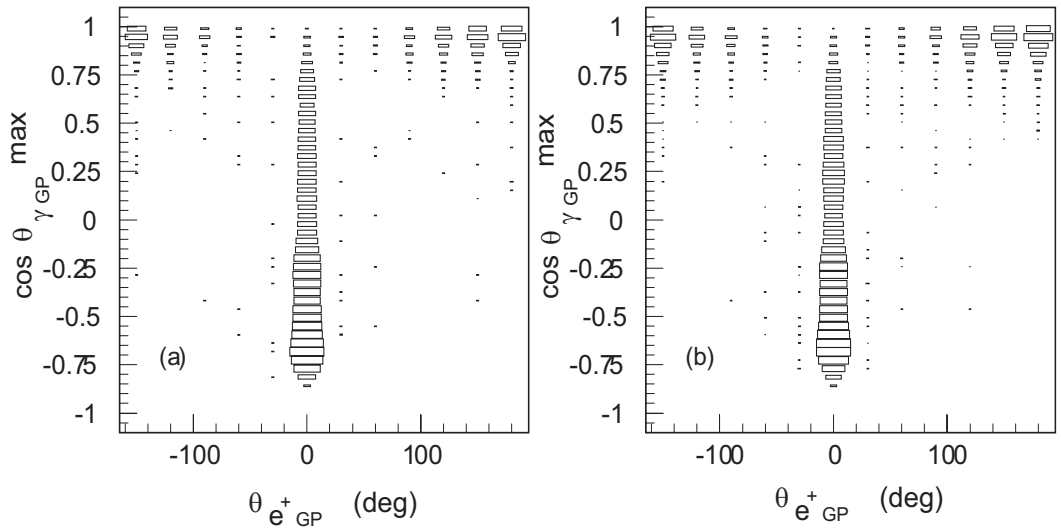

Figure 39: Correlation plot of $\theta_{e^+\mathrm{GP}}$ and $\cos\theta^{\max}_{\gamma\mathrm{GP}}$ for (a) the experimental data and (b) the simulation. The GP counter which detects the shower leakage is centered near the γ hit position in the calorimeter.

around the γ hit position in the calorimeter.

In order to reduce the effect from the shower leakage and to clarify the bremsstrahlung nature, an additional cut condition $\cos\theta_{\gamma\mathrm{GP}} < 0.2$ was imposed. This cut efficiently rejected events due to the shower leakage and enhanced the BP events. The $\theta_{e^+\mathrm{BP}}$ distribution after this cut is shown in Fig. 40. The experimental results are in good agreement with the simulation. Since the experimental data include genuine $K_{e3\gamma}$ and K_{e4} decays, events with large θ_{e^+BP} value could still remain in Fig. 40. The number of BPs detected by the GP counter in the e^+ observed gap and the adjacent gaps were about 10% and 0.2% of the K_{e3} events, respectively. This feature indicates that most of BPs did not hit the CsI(Tl) calorimeter and escaped through the holes.

The dependence of the BP detection probability on the flight-path length in the target system (FPL) was then studied. The FPL distribution obtained by the normal K_{e3} selection condition with the GP hit requirement was normalized by those without the GP hit requirement, as shown in Fig. 41. This probability is naively expected to be proportional to FPL. The experimental spectrum is in good agreement with the calculated one, indicating the correct treatment of BP in the simulation.

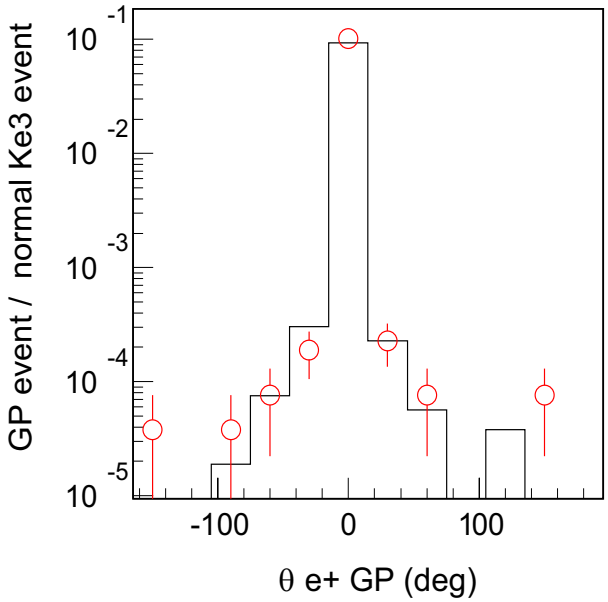

Figure 40: $\theta_{e^+\mathrm{GP}}$ distribution with the $\cos\theta_{\gamma\mathrm{GP}}$ <0.2 cut. Events with shower leakage are totally removed by this cut and the BP events are strongly enhanced. Open circles are the experimental data and histogram is the simulation.

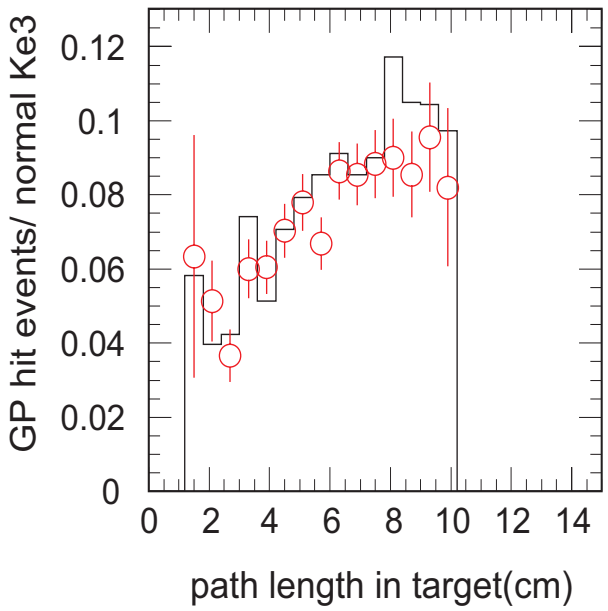

Figure 41: Probability distribution of the BP detection by the GP counter as a function of FPL, which is naively expected to be proportional to FPL.

B Appendix: Theoretical form of muon polarization from the $K^+ \to \mu^+\nu\gamma$ decay

The theoretical form of the muon polarization from the $K^+ \to \mu^+\nu\gamma$ decay can be described by defining the longitudinal (P_L), normal (P_N) and transverse (P_T), polarization asymmetries as,

$$\begin{aligned}
\rho_L(x,y) &= -e^2G_F^2\sin^2\theta_c\frac{(1-\lambda)}{2\lambda\sqrt{y^2-4r_\mu}}\left\{\frac{4m_\mu^2|f_K|}{\lambda x^2}\left[x(\lambda y-2r_\mu)(x+y-2\lambda)\right.\right.\\
&\left.-(y^2-4r_\mu)(\lambda x+2r_\mu-2\lambda)\right]-M_K^4\lambda x^2\left[|V+A|^2\frac{\lambda}{1-\lambda}(\lambda y-2r_\mu)\right.\\
&\left(1-x-\frac{r_\mu}{\lambda}\right)+|V-A|^2\left(y^2-\lambda y-2r_\mu\right)\Big]\\
&-4M_Km_\mu^2\left[Re\{f_K(V+A)^*\}\lambda\left(1-x-\frac{r_\mu}{\lambda}\right)(2-2x-y)\right.\\
&\left.+Re\{f_K(V-A)^*\}\left((1-y)(y-\lambda)+2r_\mu-\lambda\right)\right]\Big\}\ , \qquad (61)\\
\rho_N(x,y) &= e^2G_F^2\sin^2\theta_c\frac{(1-\lambda)\sqrt{\lambda y-\lambda^2-r_\mu}}{M_K\lambda\sqrt{y^2-4r_\mu}}\left\{\frac{4m_\mu^3|f_K|^2}{\lambda x}(x+y-2\lambda)\right.\\
&-M_K^4m_\mu\lambda x^2\left[|V+A|^2\frac{\lambda}{1-\lambda}\left(1-x-\frac{r_\mu}{\lambda}\right)+|V-A|^2\right]\\
&-2M_K^3m_\mu\left[Re\{f_K(V+A)^*\}\left(\frac{(r_\mu-\lambda)(1-x-r_\mu)}{1-\lambda}+\lambda x(1-x)\right)\right.\\
&\left.-Re\{f_K(V-A)^*\}(y-2r_\mu)]\right\}\ , \qquad (62)\\
\rho_T(x,y) &= -2e^2G_F^2sin^2\theta_cm_K^2m_\mu\frac{1-\lambda}{\lambda}\sqrt{\lambda y-\lambda^2-r_\mu}\left\{Im[f_K(F_V+F_A)^*]\frac{\lambda}{1-\lambda}\right.\\
&\left.\times\left(1-x-\frac{r_\mu}{\lambda}\right)+Im[f_K(F_V-F_A)^*]\right\}\ . \qquad (63)
\end{aligned}$$

where $\lambda=(x+y-1-r_\mu)/x$, $r_\mu=m_\mu^2/M_K^2$ and $x=2p\cdot q/p^2=2E_\gamma/m_K$ and $y=2p\cdot p_\mu/p^2=2E_\mu/m_K$ being normalized energies of the photon and muon, respectively. It is easily seen that the asymmetries of P_L and P_N are even quantities under time-reversal transformation, while P_T is an odd one.